Nano-Calorimetry for Point of Care Diagnostics

By

Brad Lubbers

Dissertation
Submitted to the Faculty of the
Graduate School of Vanderbilt University
in partial fulfillment of the requirements
for the degree of
DOCTOR OF PHILOSOPHY
in
Biomedical Engineering
May 2015
Nashville, Tennessee

Approved:

Franz Baudenbacher, Ph.D., Chair

Kevin Currie, Ph.D.

Robert Galloway, Ph.D.

Raymond Mernaugh, Ph.D.

Joel Tellinghuisen, Ph.D.

Hak-Joon Sung, Ph.D.

ACKNOWLEDGEMENTS

I wish to thank my wife, Paige, for putting up with me these last many years and giving me the driving force to continue, even when I wanted to throw in the towel. I thank God for strength and guidance and also for my parents and in-laws constant support and prayers. I thank Franz for giving me the autonomy to take this project where I saw fit, but at the same time guiding me in the proper direction. I also thank my committee for overseeing this project and giving it their approval. Thanks also to everyone in BME and VIIBRE who assisted in aspects of this project.

TABLE OF CONTENTS

Page

LIST OF TABLES

Table Page

LIST OF FIGURES

Figure Page

CHAPTER I

Introduction To Nano-Calorimetry For Point Of Care Diagnostics

Objective

The goal of this work is to develop microfabricated highly sensitive calorimeters for the research community and for point of care diagnostics.

Specific Aims

Essential to all chemical reactions, molecular interactions, and biological processes, is the transfer of energy according to the laws of thermodynamics. This energy flow must result in a change in energy and can be measured according to the first law of thermodynamics:

$$\Delta U = Q - W \tag{1}$$

where ΔU is the change in internal energy, Q is the heat added or taken out of the system, and W is the work performed by the system. In an isolated system, U must remain constant, so all processes that produce work either consume or produce heat, and this heat can be measured. The field of isothermal calorimetry deals with measuring this heat and characterizing reactions and processes based on it. The more accurately and quickly that temperature changes can be measured, the more details about the process can be elucidated.

In the interest of maximizing calorimeter performance and reducing sample consumption, there is a drive towards smaller sample volumes. This maximizes sensitivity and minimizes the time constant by reducing the thermal mass of the sample and measurement system. Calorimeter sensitivity can also be improved through heat flow modeling and low thermal conductivity

membrane materials like photo-definable Su-8. Using microfabrication techniques, nanowatt sensitivity thermopile based sensors can be built, but traditionally suffer tradeoffs between ease of sample handing and sensitivity. Standing drop calorimeters provide the highest sensitivity, but suffer from a lack of integrated liquid handling. Flow through calorimeters based on microfluidic channels offer simple sample handling, to the point of fully automated measurement systems, but traditionally have low sensitivity.

Calorimetry can be applied to many different disciplines, but for the most part it is limited to the research lab for use in physical materials study, chemical reaction measurements, and binding studies of drugs and proteins. Translation to the clinical setting has been slow due to the problems mentioned above. Here we propose using standard microfabrication techniques to build calorimeters capable of sub-nanowatt sensitivity for use in point of care diagnostic testing. For the first time, automated liquid handing that does not degrade device performance will be presented. The combination of nanoscale calorimetry with thin film capillary devices will allow for a scalable measurement system applicable to a number of disciplines including isothermal titration calorimetry for drug interaction screening, Thermometric Enzyme-Linked Immunosorbent Assay (TELISA) for blood antibody monitoring, and point of care (POC) diagnostic testing of many different blood analytes.

Aim 1: Construct high sensitivity calorimeters

The first aim of this dissertation was to construct and optimize thermoelectric calorimeters capable of sub-nanowatt sensitivity. This was accomplished through experimental determination of optimal nano-calorimeter materials and construction methods, heat flow modeling, and iterative optimization. The successful completion of this aim provided the basic measurement devices essential to the next aim.

Aim 2: Apply high sensitivity calorimeters to nanoliter volume Thermometric ELISA

The second aim combined standard ELISA reagents with nanoliter calorimetry to realize the small volume Thermometric ELISA. We successfully demonstrated TELISA by miniaturizing reactions and providing a quantitative thermal readout of analyte concentration. Serum matrix effects were mitigated while sample throughput was increased and sample consumption decreased. This novel technology paves the way for point of care diagnostic essential for the management of metabolic disease undergoing enzyme replacement therapy as outlined in specific aim 3.

Aim 3: Develop an automated calorimeter suitable for point of care diagnostics

The final aim used thermal and diffusion modeling to design a capillary based nano-calorimeter suited to POC diagnostics. We demonstrated the one-step measurement of common blood analytes through the thermal detection of enzymatic reactions in nanoliter sized capillary channels. By doing away with cumbersome micro-pipetting steps and eliminating most sources of error, we propel nano-calorimetry from the research lab to the clinical setting and beyond.

Background

Calorimetry

The field of calorimetry deals with the measurement of heat and energy changes associated with chemical reactions, binding events, phase changes, and metabolism to name a few[1-4]. These measurements can be made with a variety of different calorimeters with some of the most common being differential scanning calorimeters, isothermal titration calorimeters, and bomb calorimeters[5]. For the purposes of measuring the minute amounts of energy produced by living cells, protein binding, and small volume chemical reactions, isothermal calorimetry is most applicable[5]. In this form, the sample is kept in a near adiabatic condition while any heat flow changes resulting from reactions or internal processes are monitored. The temperature can be detected by any number of technologies including Resistive Temperature Detectors (RTD's), thermistors, resonance changes, and thermal expansion; though the most common is based on the thermoelectric effect[6,7]. Isothermal calorimeters can be further subdivided based on their sample volume and minimum detectable energy. The most sensitive calorimeters use microchip fabrication technology, operate with nanoliter sample volumes, and have sensitivities approaching one nanowatt[8].

Theory

Since the main sensing function of any calorimeter is to measure temperature changes, the more precisely those changes can be measured, the better the device performance becomes. As noted, the thermoelectric effect, and more specifically the Seebeck effect, is the most common method for precise temperature measurement in isothermal calorimetry. Discovered in 1821 by Thomas Johann Seebeck, the Seebeck effect relies on the generation of current when

two dissimilar metals are connected and their junctions held at different temperatures. The voltage potential is directly proportional to the temperature difference between the hot (measuring) and cold (reference) junctions and is quite linear over modest temperature ranges ($\Delta T<100$ C)[9]. The voltage produced is due to the differential thermal charge carrier drag along the length of wire with the ends at different temperatures and its sign and magnitude are dependent on material properties[10]. This self-generation of voltage is one of the main advantages of a thermocouple over a thermistor or RTD. Potential self-heating produced by the latter devices completely overwhelms any small temperature changes. The Seebeck coefficient (S) can be determined for metals and semiconductors and is measured in units of microvolt/Kelvin. When a thermocouple is formed from materials of known S and the resulting voltage (V) measured, the temperature difference between the two junctions can be found by:

$$\Delta T = (S_1 - S_2) \cdot V \tag{2}$$

For a single junction this voltage would be quite small, but by placing many thermocouples in series and forming a thermopile, the effect is additive. Materials with a high S make for high sensitivity thermopiles; however S and conductivity are roughly inversely proportional with the highest S materials being semiconductors with very high resistances[9,10].

Electrical resistance is an important factor of thermopiles as it determines the principle noise component. Since thermopiles self-generate voltage, Johnson-Nyquist noise can be described by the spectral noise density:

$$V_n = \sqrt{4\, k_B T R} \tag{3}$$

where k_B is the Boltzmann's constant, T the resistor's absolute temperature, and R the resistance of the thermopile. Therefore a balance must be struck between high S and low R. Many research

grade calorimeters utilize low resistance metals like gold and nickel that are easily processed using microfabrication techniques, but lack high S[11,12]. Utilization of bismuth and antimony based thermopiles produces very high sensitivity devices with moderate resistance, but are more difficult to work with at the sub 100 μm linewidths needed for nanoliter scale calorimeters[13]. Others utilize microfabrication friendly, high S semiconductors for thermopile materials, but suffer from high overall resistance (>200 kΩ)[14].

Another important consideration is heat flow out of the calorimeter. The higher the resistance to heat flow, the longer heat remains in the calorimeter at the hot junction where it can be measured. The total Seebeck coefficient for the thermopile (S_{tot}) and the total heat flux away from the sample (G_{tot}) are combined in the follow equation to give the overall power sensitivity (P_{sens}) in V/W for a thermoelectric calorimeter:

$$P_{sens} = S_{tot}/G_{tot} \quad (4)$$

G_{tot} is expressed in terms of amount of power in W needed to raise the sample temperature 1 K. The G_{tot} term is comprised of several different fluxes including flux through the thermopile traces, supporting substrate, air, and radiation. At such small ΔT, radiation is negligible and the main flux pathway is through the substrate. For this reason, most high sensitivity calorimeters are fabricated on suspended membranes surrounded by air (**Figure 1**). The open form of calorimeter, shown in **Figure 1** benefits from minimal contact between the sample droplet and membrane. In the closed or microfluidic form, the sample drop is contacted on all sides by the microfluidic channel. This provides thermal conduction away from the sample and greatly increases $G_{tot.}$ By reducing the thickness and thermal conductivity of the membrane and thermopile, G_{tot} can be minimized. Traditionally silicon nitride and silicon dioxide have been used as membrane materials due to their strength and compatibility with microfabrication techniques. Compared to

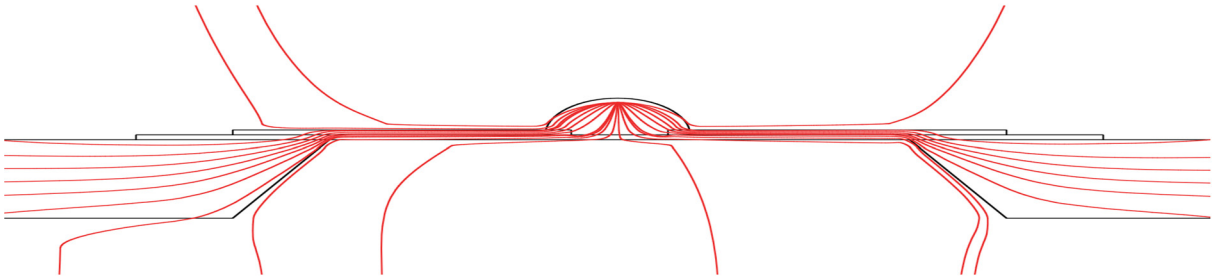

Figure 1. Calorimeter heat flow. For an ideal calorimeter with a sample droplet sitting atop the sensing thermopile and membrane, the main heat flux (red lines) is through the thermopile and membrane, with little transferred through the air.

SiN or SiO_2, utilizing a polymeric membrane can reduce membrane heat flux by as a factor of 40[15]. Polymeric membranes of parylene-C or Su-8 have been used on a few high sensitivity calorimeters, but are not yet the norm[12,16]. Su-8 is a well suited membrane material as it possess a very low thermal conductivity (~0.25 W/m·K), is photopatternable, withstand temperatures up to 300 °C, and is resistant to all but the harshest chemicals[17].

With G_{tot} and V_n known, another important parameter can be calculated, minimum detectable power change (P_{min}) with the following equation:

$$P_{min} = \Phi / P_{sens} \tag{5}$$

Φ is total noise, both thermal and electronic, but for a well isolated system with a low noise amplifier, Φ is mainly comprised of V_n. Similarly, the parameters Φ and S_{tot} can be used to find the minimum detectable temperature change with the following equation:

$$T_{min} = \Phi / S_{tot} \tag{6}$$

Equations 5 and 6 specify the minimum detectable signal with a signal to noise ratio of 1, however a more realistic ratio of 2 or 3 may be needed to provide a measurable signal. Though a

small P_{min} may be advantageous for some measurements, the response time (τ) of the system may be more important for fast processes with rapid changes in enthalpies. The following equation shows how τ is inversely proportional to G_{tot}:

$$\tau = C_{tot}/G_{tot} \quad (7)$$

C_{tot} is the total thermal mass of the calorimeter sensing area, including the sample itself. For an open, suspended membrane calorimeter, this is principally the sample thermal mass. A reduction in sample volume enhances τ and increases the effective bandwidth. Since P_{min} is in units of $W/Hz^{1/2}$, an increase in bandwidth leads to a lower minimum detectable energy.

While equations 4-7 provide useful insight into calorimeter parameters, they assume ideal conditions of uniform heat distribution, flux, and thermal conductivity in the sample. Experimental results may differ significantly from the equation predictions and in its place finite element analysis modeling provides a more accurate model of calorimetric systems. Being that any model is no more accurate than the parameters input into it, it is worthy to note the thin film properties of many materials differ significantly from the bulk values in the sub-micron range[9,18]. In order to create a robust model, these thin film parameters must either be measured or the model fit to empirically determined values for equations 3-6.

Calibration

The measurement of the parameters in equations 3-6 can take several forms depending on the calorimeter design. τ can be measured directly based on sample heating via a built in heater strip or laser heating. Likewise, P_{sens} can be measured in a similar fashion if a known amount of energy is input into the system. Using a built in heater near the sample volume provides the easiest method of sensitivity determination[19,20], but suffers from error due to localized heating

around the resistive element that does not originate within the sample volume. Laser heating of the sample is also problematic if the sample or membrane is semi-transparent in the laser wavelength. A more experimentally accurate determination of sensitivity can be made using binary chemical reactions[21,22]. In this form, the reaction of measured amounts of acid and base within the sample droplet mimics closely the thermodynamics of reactions of interest.

Performance

When comparing different calorimeters it is useful to look at not only their minimum power sensitivity, but also their thermal conductance as shown in **Table 1**. Closed calorimeters utilize microfluidics for sample handing and hence are easier to operate and do not suffer from sample evaporation problems. Aside from the Caltech device, most are lacking in sensitivity due to the large G_{tot} contributed by the microfluidic channels and conductance through the sample fluid itself. The low thermal conductance of the Caltech device was due to vacuum insulation of the sample sensing area[12]. The closed, microfluidic devices also suffer from a degradation of practical P_{min} due to flow noise through the chamber. An equally deleterious reduction in

Table 1. Comparison of different micro-calorimeters. Adapted[12]

	Chamber					Resolution*		
Group (source)	Type	Volume, nL	Sample handling	Thermal conductance, μW/K	Response time, ms	Power, nW	Theoretical energy, nJ†	Practical energy, nJ‡
Caltech	Closed	3.5	Multilevel microfluidics	16	325	4.2	6	10
Penn State	Closed	15§	Syringe pump	5,000	1.6	300	30	10^5
Eurotronics	Closed	6,000§	Syringe pump	10,000	1,770	30	100	1,000
Columbia	Closed	800§	Syringe pump	1,500	60	50	30	5,000
Scripps-Palo Alto Research Center	Open	500	Electrostatic merging	1,000	630	50	100	750
Katholieke Universiteit Leuven	Open	10^5 to 10^7	Micropipette	5,000	63	5,000	10^5	10^6
University of Glasgow	Open	0.75	Micropipette	100	12	13	3.6	100
Technische Universität Bergakademie Freiberg	Open	6,000	Micropipette	30,000	16,000	50	500	5,000
Vanderbilt	Open	5–50	Micropipette	65	100	15	1.2	2
Vanderbilt	Open	0.05	Inkjet head	90	0.006	150	1	500
Commercial	Open	10^6	Micropipette	N/A	N/A	10	N/A	100

N/A, not available.
*Power and energy resolution are based on a 3:1 signal-to-noise ratio.
†Theoretical energy resolution is the product of (noise-limited) power resolution and thermal relaxation time.
‡Practical energy resolution also includes measurement irreproducibility from fluidic volume uncertainties in injection, mixing, and evaporation. Evaporation is particularly deleterious for small, open-chamber calorimeters.
§Flow calorimeters are typically operated at flow rates of 0.5 mL/h.

practical P_{min} is seen for the open calorimeters due to sample evaporation and micropipette injection errors. This error was reduced considerably for the first Vanderbilt calorimeter listed through baseline shift correction and better sample chamber sealing[23]. No calorimeters to date have shown a practical energy resolution of less than 1 nJ. In order to reach this goal, better sample handling, evaporation control, and higher power sensitivity is needed. Towards this goal heat diffusion modeling can be applied to optimize calorimeter design.

Modeling

Finite element analysis (FEA) is a powerful mathematical tool for simulating chemical or thermal diffusion processes. The basis of FEA is the subdivision of a complex mathematical model into smaller, finite subunits (the mesh) in which partial differential equations can be more readily approximated[24]. Though originally applied to structural engineering problems, FEA can be used to analyze many different processes; of which heat flow, microfluidics, and molecular diffusion are of the most interest to the work at hand[25]. With the advent of software like COMSOL Multiphysics and MATLAB, multiple properties can be simulated at once with the ability to perform iterative feedback optimizations of calorimeter designs. This not only aids calorimeter design, but also guides experimental design by predicting the thermal output and reaction kinetics of chemical and enzymatic processes. However, as with any other model system, FEA is highly sensitive to imperfections in the model. This is especially true in the case of nano-calorimeters, which are composed of thin film materiuals and normally operated in the microfluidic flow regime. The thin film properties of materials, especially metals, can vary greatly from their bulk properties due to grain boundaries restricting the mean free path[9]. This necessitates empirical testing of thin film materials, as citable sources are sparse and can vary greatly depending on how the films were prepared[26]. Another approach to improve model

accuracy is the least-square fitting of model parameters to actual experimental results from the device in question.

Enzymes

Many different biological assays rely on enzymatic reactions to produce quantifiable signals (e.g. fluorescent, chemiluminescent, colorimetric, potentiometric, amperometric, acoustic, or calorimetric to name a few)[6,27-32]. These signals may be the direct result of an enzyme consuming the analyte and causing an optical absorbance change, as in the case of a peroxide assay utilizing catalase. The signaling could be more complex like that of a phenylalanine assay based on PAL that measures the pH change due to ammonia production[33]. By far the most widely utilized biosensor is that based on the amperometric measurement of H_2O_2 resulting from the oxidation of glucose by GOx in the commercial glucose sensors used by diabetics[6]. Much like equation 1 from the first law of thermodynamics, any enzymatic reaction can be studied using the Gibbs equation to find the change in energy:

$$\Delta G = \Delta H - T\Delta S \tag{8}$$

where ΔG (at a constant temperature) is the change in free energy, ΔH is the total heat change (enthalpy), T is temperature, and ΔS is the change in entropy. Since we are dealing with calorimetry, we are primarily interested in changes in enthalpy, since that leads to changes in temperature. The quantifications of this heat provides the basis for all calorimetric biosensors[34]. We are also concerned mainly with reactions that are exergonic (-ΔG) at or near room temperature so reactions will proceed towards the products. Utilizing nano-calorimeters to study enzymatic reactions with large -ΔH allows for the detections of very low concentrations of reactants (analytes). Even though any reaction with -ΔG will occur spontaneously, the time scale

Table 2. Comparison of reaction enthalpies and enzyme kinetics. Adapted[35-40]

Reaction	ΔH (kJ/mol)	Enzyme	K_m (mM)	k_{cat} (s^{-1})
$H_2O_2 \leftrightarrow H_2O + 1/2O_2$	-98	catalase	1.1	4.0×10^6
$3H_2O_2$ + 2OPD $\leftrightarrow 6H_2O$ + DAP	-297	horseradish peroxidase (HRP)	0.6	1.5×10^3
$C_6H_{12}O_6 + 1/2O_2 \leftrightarrow C_6H_{10}O_6 + H_2O_2$	-80	glucose oxidase (GOx)	6.0	1.8×10^3
$CO_2 + H_2O \leftrightarrow H_2CO_3$	-20	carbonic anhydrase	0.012	1.0×10^6
cholesterol + O_2 = cholest-5-en-3-one + H_2O_2	-53	cholesterol oxidase	0.03	6.5×10^1
L-phenylalanine $\leftrightarrow$ trans-cinnamic acid + NH_3	+25	phenylalanine ammonia-lyase (PAL)	0.2	1.2×10^2
$2NH_3 + CO_2 \leftrightarrow$ urea + H_2O	+58	urease	12	3.0×10^2

over which it happens is determined by its energy of activation (E_a). As shown in **Table 2**, the decomposition of hydrogen peroxide into water and oxygen has a relatively large ΔG and ΔH, making it a good candidate for calorimetric measurements. However, its E_a is very high (+75 kJ/mol) meaning that the likelihood of spontaneous decomposition is rare at room temperature. The actual rate is exponentially dependent on E_a as the Arrhenius equation (9) shows[35].

$$k = A \cdot e^{\frac{-Ea}{RT}} \tag{9}$$

A change of 2.48 in E_a leads to 10 fold increase in reaction rate. The E_a of H_2O_2 in the presence of catalase is only +8.4 kJ/mol meaning H_2O_2 reacts millions of times faster than on its own. E_a is not the only factor governing reaction kinetics, the Michaelis-Menten equation links enzyme kinetics and substrate concentration to the overall rate:

$$v = \frac{k_{cat}[E_0][S]}{K_m + [S]} \tag{10}$$

where k_{cat} is the maximum turnover rate, K_m is substrate concentration at half k_{cat} rate, $[E_0]$ is enzyme concentration, and [S] is substrate concentration. Enzymes with high k_{cat} and large ΔH (like catalase and glucose oxidase) are good candidates for calorimetric biosensors, as they consume substrate quickly and produce a large output, even at the low concentrations that may be present in diagnostic samples (**Table 2**). A common enzyme class, oxidases, have many

corresponding blood analytes of interest (i.e. cholesterol, carbohydrates, many amino acids)[34]. These are energetic on their own and the H_2O_2 produced can be coupled to catalase to more than double the output heat[39]. Similarly, an enzyme such as phenylalanine ammonia-lyase that releases NH_3 can be coupled to a dehydrogenase or urease to increase output. However, the enzyme kinetic values cited in many textbooks differs greatly from reported experimental kinetic data due to differences in enzymes and reaction environments[41]. This necessitates experimental validation and modeling to determine the true kinetic values under actual reaction conditions as any calorimetry based assay will be sensitive to changes in reaction rates. Similarly, the enthalpy values are sensitive to buffer conditions, concentration, and temperature, and as such need to be experimentally determined and factored into the modeling.

Enzyme Immobilization

While some research grade calorimetric biosensors utilize unbound enzymes, a commercial biosensor requires some form of enzyme immobilization. This is usually accomplished through crosslinking, covalent bonding, or physical entrapment of the enzymes[42]. Enzyme preservation is equally important and aims to prevent loss of enzyme structure and activity through enzyme modification, structural confinement, or stabilization reagents that maintain pH and humidity[43]. The most common class of calorimetric biosensors are based on flow through columns containing support matrixes to which the principle enzyme or analyte is bound[39]. One of the first flow through sensors utilized hexokinase bound to glass beads in a 1 ml column to measure glucose concentration[44]. Modern sensors often rely on chemical crosslinking with glutaraldehyde or affinity linking to bind enzymes to high surface area resin. A large excess of enzyme is required for these column based calorimeters since both C_{tot} and G_{tot} are large as compared to nanocalorimeters, however this excess allows columns to be used hundreds of times

with minimal enzyme degradation[39]. Dip type sensors in which the enzyme is immobilized directly to the transducer are common also[45]. A support matrix of porous carbon or silica gel (sol-gel) contains the enzymes and prevents complete desiccation[46]. Silica sol-gels are formed when colloidal silica solutions are allowed to gel through organometallic or acid/base catalysts[47]. When the sol-gel solvent is allowed to evaporate after gelling, a highly cross-linked, and high surface area (>300 m^2/g) xerogel is formed. If an enzyme is present during gelling, it becomes entrapped in the gel and many have succeeded in creating enzyme containing xerogels that retain high activity. In many cases, enzyme activity is maintained better than lyophilized enzymes due to the stabilizing effects of the sol-gel[48]. For applications in which a monolayer of enzyme or antibody bound to a surface is desired, bioaffinity and passive absorption are commonly used. Bioafinity based on the biotin/avidin linking system can produce nearly irreversible binding due to high binding affinity (>1 x 10^{-15} M) of the pair[49]. Many proteins can be biotinylated in neutral conditions, thereby avoiding harsh chemical crosslinking environments. Similarly, many proteins will self-assemble on gold surfaces due to thiol interaction or passively absorb due to hydrophilic/phobic interactions with surfaces at their isoelectric point pH[50,51]. Monolayer formation is advantageous for nanocalorimetry systems where there is no available volume for a 3-D support matrix. Regardless of the immobilization technique, K_m , k_{cat}, and optimal pH can vary due to the constraining effect of the carrier[52]. Steric hindrance and hydrophilic/phobic interactions with the support medium can significantly reduce enzyme activity and must be taken into account.

ELISA

Enzyme-linked immunosorbent assays (ELISAs) have become the gold standard for measuring antibodies and antigens, both native and introduced, in biological samples since the

1970s[32]. ELISA has replaced radioimmunoassay in most cases due to greater flexibility and the avoidance of radioactive antigens[53]. Of the many commercially available ELISA kits, most utilize an enzyme linked to a detecting antibody to produce a colorimetric, chemiluminescent, or fluorescent signal that can be quantified using a microplate reader[54]. There are several different types of ELISA, with each suited to particular applications.

The simplest ELISA (direct) relies on an antigen coated sample well in which the sample (usually diluted serum) containing the primary antibody (Ab_1) of interest is added. Then a secondary antibody (Ab_2) containing a reporter enzyme is added and its output read. This is best for measuring antibody titers in serum, but can suffer from serum matrix effects that lead to non-specific binding of serum component to the sample well surface. The second type (sandwich) uses sample wells that are precoated with Ab_1. Then the sample containing the antigen or antibody of interest is allowed to interact. Then a reporter enzyme linked Ab_2 specific to the antigen or antibody, but binding in a different spot than Ab_1 is introduced and read. A sandwich ELISA is less susceptible to serum matrix-effects and when combined with an antigen standard can produce quantitative results. The final main type (competitive) relies on competitive binding of a known and unknown antigen. A known amount of enzyme linked antigen or antibody is mixed with the sample and then exposed to a coated well and read. If the antigen or antibody of interest is present in the sample, it will compete with the enzyme linked one and produce less signal[55]. This is well suited to situations were a complementary Ab_2 is not available but quantitative results are still needed.

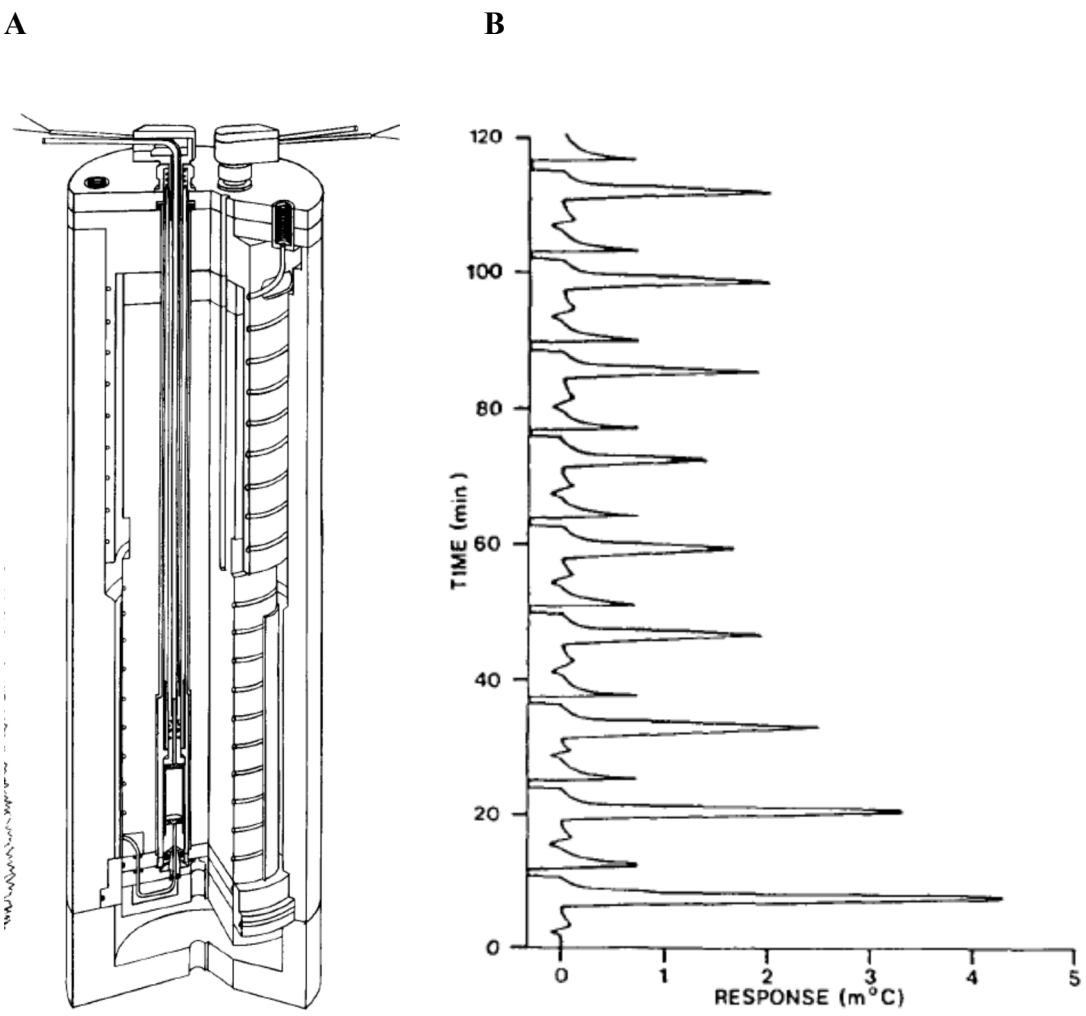

Figure 2. Column based Thermometric ELISA (A) The measurement cell contained a sample and reference column, both in an insulated, temperature controlled casing. (B) Response from TELISA experiment with porcine proinsulin. In ascending order, 0, 5, 10, 20, 30 40 µg/ml, followed by triplicate samples from an *E. coli* cultivation. Adapted[34]. © 1990 Elservier Science Publishers B.V.

Optical transduction is the most common ELISA detection method, with chemiluminescence often regarded as the most sensitive, allowing antigen detection below 1 pg/ml with appropriate enzyme amplification systems[56]. Though less sensitive, calorimetry is a viable detection method for ELISA. Flow through calorimetric biosensors have been utilized in thermometric ELISA (TELISA) to measure ug/ml levels of insulin, IgG, and albumin to name a few[57,58]. Prior TELISA systems have operated in a competitive assay mode whereby an enzyme

linked antibody or antigen is included with the sample and after washing, is exposed to the substrate to produce a measurable heat output. Being column based (**Figure 2A**), sample consumption is rather large (i.e. > 0.5 ml) and response time is 3 orders of magnitude slower than in nano-calorimeters[59]. In order to provide a quantitative measurement of an analyte in a sample, standard analyte concentration curves must be generated during sample analysis for accurate quantification of analyte concentrations in samples (**Figure 2B**). Additionally, personnel time and the antibodies needed to carry out ELISAs can be costly. This, in combination with sample consumption and the long time needed to perform ELISA precipitates the need for a rapid, low-volume, calibration-free ELISA system.

Point of Care Diagnostics

The goal of point-of-care (POC) diagnostics is to provide near instantaneous results for many common blood tests that previously required expensive laboratory equipment and personnel time. POC blood glucose meters made up almost half of the $15.5 billion POC market in 2013[60]. Though not a replacement for a clinical lab test, the information provided by the testing can help diabetic patients regulate their glucose levels through medication and diet. Phenylketonuria represents another disease where at-home monitoring is needed to help effectively manage the disease. Affecting 1 in 15,000 people worldwide, the genetic disease phenylketonuria prevents the metabolism of the essential amino acid phenylalanine (Phe), leading to high blood concentrations that can cause mental retardation if not treated though diet and/or enzyme replacement therapy[61]. Though much faster and more accurate than the bacterial inhibition assays of the 1960's, tandem mass spectrometry (MS/MS) testing of blood Phe levels is still limited to the clinical laboratory[62]. With new enzyme replacement therapies for phenylketonuria undergoing human clinical trials, the need for at home Phe monitoring to dictate

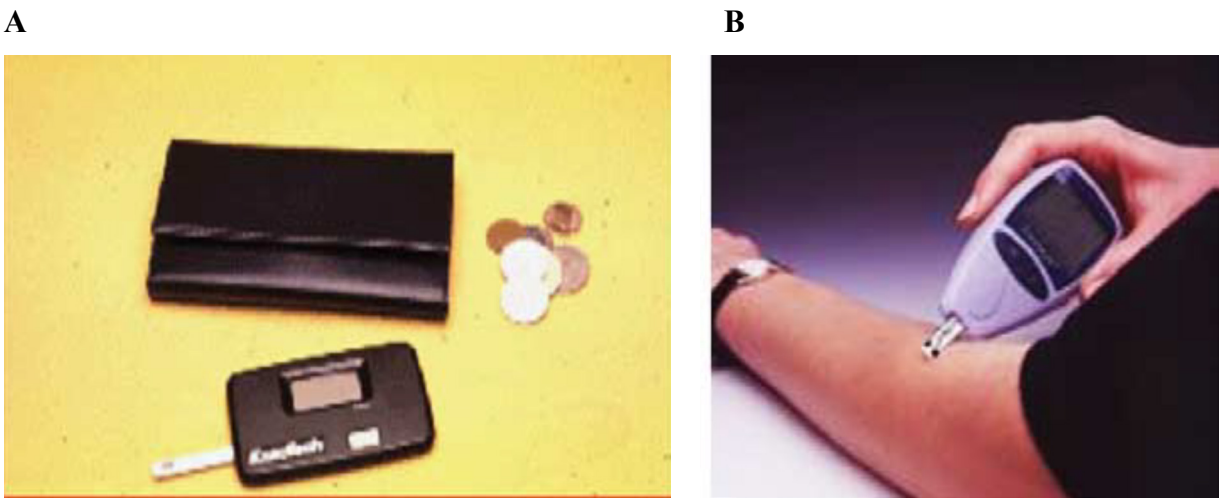

Figure 3. POC glucose devices. (**A**) Early devices required manual coding and a large sample size. (**B**) Current devices feature alternative site testing and automatic coding. Adapted[65]. © 2004 Elservier B.V.

dosing and diet is even greater[63]. Prior devices for POC Phe measurement have lacked long term stability[33], and as with most glucose sensors are dependent on constant enzyme activity for accurate measurements.

A successful POC device by definition should be useable by someone with no technical training and insensitive to most user errors. For example, early generation blood glucose monitors required the end user to enter codes related to the sensitivity of the GOx based sensor and were a common cause of errors[64](**Figure 3A**). By improving manufacturing tolerances, changing detection methods, and increasing enzyme stability, current generation devices have eliminated coding. Equally important is patient compliance with the testing. Early devices required > 10 µl of blood, necessitating painful finger sticks prompting many patients to skip routine testing[64]. Current devices requiring <1 µl of blood allow for less painful arm sticks (**Figure 3B**). Others have developed non-invasive glucose monitors based on saliva glucose levels[65,66], but these have not yet reached market as the correlation between saliva and blood glucose levels vary[67]. A user friendly POC device should not require the user to add reagents to

or treat the sample, nor require them to precisely measure the sample volume. Controls must be in place to alert the user if there is a problem with the sample or the test itself. Lateral flow assays (LFAs) have accomplished this well through the use of parallel control reactions. Most LFAs rely on ELISA technology to selectively bind to and indicate the presence of a specific blood or urine antigen or antibody[67]. In the case of home pregnancy tests, if insufficient sample is provided or there are other problems with the device, the control line will not develop, indicating the user to reject the results.

Biosensors are the basis for most POC diagnostic technologies. However, only a few calorimetric biosensors suited to POC have been developed pertaining to the measurement of blood glucose or urine urea due to the large enthalpy changes associated with these reactions (-80 and -61 kJ/mol)[68,69]. In the case of Davaji and Lee, a thin film resistive temperature detector is employed, so temperature senility is limited to 26 mK and noise limited minimum glucose concentration is 1.51 mM. A paper strip held the glucose oxidase enzyme in close proximity to the sensing surface, however it had to be added to the flow strip at the beginning of each measurement and evaporative effects caused a large drift in the calorimeter signal. Lai and Tadigadapa's device relied on a Y-cut quartz resonator for temperature sensing, giving higher temperature sensitivity. However, the entire device had to be placed in a 37 ˚C oven during measurements, microfluidic pumping systems were required, and the uncertainty in their urea detection results were too high for reliable use. In order to create a user-friendly POC device, liquid handing must be automated and insensitive to user error.

One approach that avoids the high thermal conductance's of standard microfluidics while still allowing for efficient, evaporation limited sample delivery is to utilize capillary action in thin channels to draw samples in. Much like a LFA or glucose test strip, the required amount of

sample is automatically drawn. Excess sample goes to an overflow reservoir or once full, no more sample is pulled into the reaction zone.

References

1. Reading, M., Elliott, D. & Hill, V. L. A New Approach to the Calorimetric Investigation of Physical and Chemical-Transitions. *J. Therm. Anal.* **40**, 949-955 (1993).
2. Leavitt, S. & Freire, E. Direct Measurement of Protein Binding Energetics by Isothermal Titration Calorimetry. *Curr. Opin. Struct. Biol.* **11**, 560-566 (2001).
3. Mabrey, S. & Sturtevant, J. M. Investigation of Phase-Transitions of Lipids and Lipid Mixtures by High Sensitivity Differential Scanning Calorimetry. *Proc. Natl. Acad. Sci. U. S. A.* **73**, 3862-3866 (1976).
4. Kemp, R. B. The Application of Heat Conduction Microcalorimetry to Study the Metabolism and Pharmaceutical Modulation of Cultured Mammalian Cells. *Thermochim. Acta* **380**, 229-244 (2001).
5. Braissant, O. et al. Biomedical Use of Isothermal Microcalorimeters. *Sensors-Basel* **10**, 9369-9383 (2010).
6. De Corcuera, J. I. R. & Cavalieri, R. P., in *Encyclopedia of Agricultural, Food, and Biological Engineering* (Taylor & Francis, 2007), pp. 119-123.
7. Inomata, N. et al. Pico Calorimeter for Detection of Heat Produced in an Individual Brown Fat Cell. *Appl. Phys. Lett.* **100** (2012).
8. Johannessen, E. A. et al. A Suspended Membrane Nanocalorimeter for Ultralow Volume Bioanalysis. *IEEE Trans Nanobioscience* **1**, 29-36 (2002).
9. Boyer, A. & Cisse, E. Properties of Thin-Film Thermoelectric-Materials - Application to Sensors Using the Seebeck Effect. *Materials Science and Engineering B-Solid State Materials for Advanced Technology* **13**, 103-111 (1992).
10. Vanherwaarden, A. W. & Sarro, P. M. Thermal Sensors Based on the Seebeck Effect. *Sensor Actuator* **10**, 321-346 (1986).
11. Johannessen, E. A. et al. Micromachined Nanocalorimetric Sensor for Ultra-Low-Volume Cell-Based Assays. *Anal. Chem.* **74**, 2190-2197 (2002).
12. Lee, W. et al. High-Sensitivity Microfluidic Calorimeters for Biological and Chemical Applications. *Proc. Natl. Acad. Sci. U. S. A.* **106**, 15225-15230 (2009).
13. Kopparthy, V. L. et al. Thermoelectric Microfluidic Sensor for Bio-Chemical Applications. *Sensor Actuat B-Chem* **166**, 608-615 (2012).
14. Zhang, Y. Y. & Tadigadapa, S. Calorimetric Biosensors with Integrated Microfluidic Channels. *Biosens. Bioelectron.* **19**, 1733-1743 (2004).
15. Zhang, X. & Grigoropoulos, C. P. Thermal Conductivity and Diffusivity of Free-Standing Silicon Nitride Thin Films. *Rev. Sci. Instrum.* **68**, 1115-1120 (1995).
16. Mattsson, C. G. et al., *IEEE Sensors 2007* (Atlanta, GA, 2007), pp. 836-839.
17. Lorenz, H. et al. High-Aspect-Ratio, Ultrathick, Negative-Tone near-Uv Photoresist and Its Applications for Mems. *Sensor Actuat a-Phys* **64**, 33-39 (1998).
18. Bourque-Viens, A. et al. Modelling and Experimental Validation of Thin-Film Effects in Thermopile-Based Microscale Calorimeters. *Sensor Actuat a-Phys* **150**, 199-206 (2009).
19. Johannessen, E. A. et al. Heat Conduction Nanocalorimeter for Pl-Scale Single Cell Measurements. *Appl. Phys. Lett.* **80**, 2029-2031 (2002).
20. Chancellor, E. B. et al. Heat Conduction Calorimeter for Massively Parallel High Throughput Measurements with Picoliter Sample Volumes. *Appl. Phys. Lett.* **85**, 2408-2410 (2004).

21. Wadso, I. Design and Testing of a Micro Reaction Calorimeter. *Acta Chem. Scand.* **22**, 927-& (1968).
22. Briggner, L. E. & Wadso, I. Test and Calibration Processes for Microcalorimeters, with Special Reference to Heat Conduction Instruments Used with Aqueous Systems. *J. Biochem. Biophys. Methods* **22**, 101-118 (1991).
23. Lubbers, B. & Baudenbacher, F. Isothermal Titration Calorimetry in Nanoliter Droplets with Subsecond Time Constants. *Anal. Chem.* **83**, 7955-7961 (2011).
24. Strang, G. & Fix, G. J., *An Analysis of the Finite Element Method*. (Prentice-Hall Englewood Cliffs, NJ, 1973).
25. Reddy, J. N. & Gartling, D. K., *The Finite Element Method in Heat Transfer and Fluid Dynamics*. (CRC press, 2010).
26. Nix, W. Mechanical Properties of Thin Films. *Metall. Trans. A* **20**, 2217-2245 (1989).
27. Voller, A., Bartlett, A. & Bidwell, D. E. Enzyme Immunoassays with Special Reference to Elisa Techniques. *J. Clin. Pathol.* **31**, 507-520 (1978).
28. Du, D. et al. Sensitive Immunosensor for Cancer Biomarker Based on Dual Signal Amplification Strategy of Graphene Sheets and Multienzyme Functionalized Carbon Nanospheres. *Anal. Chem.* **82**, 2989-2995 (2010).
29. Ahmed, M. U. et al. Electrochemical DNA Biosensor Using a Disposable Electrochemical Printed (Dep) Chip for the Detection of Snps from Unpurified Pcr Amplicons. *Analyst* **132**, 431-438 (2007).
30. Chen, X. et al. Electrochemical Immunosensor for Simultaneous Detection of Multiplex Cancer Biomarkers Based on Graphene Nanocomposites. *Biosensors Bioelectron.* **50**, 356-361 (2013).
31. Xie, B. et al. Fast Determination of Whole-Blood Glucose with a Calorimetric Micro-Biosensor. *Sensor Actuat B-Chem* **15**, 141-144 (1993).
32. Premjeet, S. et al. Enzyme-Linked Immuno-Sorbent Assay (Elisa), Basics and It's Application : A Comprehensive Review. *J. Pharm. Res.* **4**, 4581-4583 (2011).
33. Zhuo, W. et al., presented at the Engineering in Medicine and Biology Society, 2005. IEEE-EMBS 2005. 27th Annual International Conference of the, 2005 (unpublished).
34. Danielsson, B. Calorimetric Biosensors. *J. Biotechnol.* **15**, 187-200 (1990).
35. Nelson, D. L., Lehninger, A. L. & Cox, M. M., *Lehninger Principles of Biochemistry*. (W.H. Freeman, New York, 2008).
36. Liu, H. et al. Enthalpy Change and Mechanism of Oxidation of O-Phenylenediamine by Hydrogen Peroxide Catalyzed by Horseradish Peroxidase. *Thermochim. Acta* **443**, 173-178 (2006).
37. Hamilton, T. M., Dobie-Galuska, A. A. & Wietstock, S. M. The O-Phenylenediamine-Horseradish Peroxidase System: Enzyme Kinetics in the General Chemistry Laboratory. *J. Chem. Educ.* **76**, 642 (1999).
38. Domalski, E. S. Selected Values of Heats of Combustion and Heats of Formation of Organic Compounds Containing the Elements C, H, N, O, P, and S. *J. Phys. Chem. Ref. Data* **1**, 221-277 (1972).
39. Lammers, F. & Scheper, T. Thermal Biosensors in Biotechnology. *Adv. Biochem. Eng. Biotechnol.* **64**, 35-67 (1999).
40. Goldberg, R. N., Tewari, Y. B. & Bhat, T. N. Thermodynamics of Enzyme-Catalyzed Reactions--a Database for Quantitative Biochemistry. *Bioinformatics* **20**, 2874-2877 (2004).

41. Bar-Even, A. et al. The Moderately Efficient Enzyme: Evolutionary and Physicochemical Trends Shaping Enzyme Parameters. *Biochemistry (Mosc).* **50**, 4402-4410 (2011).
42. Sheldon, R. A. Enzyme Immobilization: The Quest for Optimum Performance. *Adv. Synth. Catal.* **349**, 1289-1307 (2007).
43. Minteer, S. D., *Enzyme Stabilization and Immobilization : Methods and Protocols*. (Humana Press, New York, 2011).
44. Bowers, L. D. & Carr, P. W. An Immobilized-Enzyme Flow-Enthalpimetric Analyzer: Application to Glucose Determination by Direct Phosphorylation Catalyzed by Hexokinase. *Clin. Chem.* **22**, 1427-1433 (1976).
45. Gibson, T. D., Pierce, B. L. J. & Parker, S. M., in *Biosensors for Food Analysis*, edited by A. O. Scott (Woodhead Publishing, 2005), pp. 46-53.
46. Ellerby, L. et al. Encapsulation of Proteins in Transparent Porous Silicate Glasses Prepared by the Sol-Gel Method. *Science* **255**, 1113-1115 (1992).
47. Brinker, C. J. & Scherer, G. W., *Sol–Gel Science*. (Academic Press, San Diego, 1990).
48. Bhatia, R. B. et al. Aqueous Sol−Gel Process for Protein Encapsulation. *Chem. Mater.* **12**, 2434-2441 (2000).
49. Diamandis, E. P. & Christopoulos, T. K. The Biotin-(Strept)Avidin System: Principles and Applications in Biotechnology. *Clin. Chem.* **37**, 625-636 (1991).
50. Hakkinen, H. The Gold-Sulfur Interface at the Nanoscale. *Nature chemistry* **4**, 443-455 (2012).
51. Ebersole, R. C. et al. Spontaneously Formed Functionally Active Avidin Monolayers on Metal-Surfaces - a Strategy for Immobilizing Biological Reagents and Design of Piezoelectric Biosensors. *J. Am. Chem. Soc.* **112**, 3239-3241 (1990).
52. Tischer, W. & Wedekind, F., in *Biocatalysis - from Discovery to Application*, edited by Wolf-Dieter Fessner, A. Archelas, D. C. Demirjian et al. (Springer Berlin Heidelberg, 1999), Vol. 200, pp. 95-126.
53. Fowler, E. & Cheng, N. Comparison of Radioimmunoassay and Elisa Methods for Detection of Antibodies to Chromatin Components. *J. Immunol. Methods* **62**, 297-303 (1983).
54. Lequin, R. M. Enzyme Immunoassay (Eia)/Enzyme-Linked Immunosorbent Assay (Elisa). *Clin. Chem.* **51**, 2415-2418 (2005).
55. Voller, A., Bidwell, D. E. & Bartlett, A. Enzyme Immunoassays in Diagnostic Medicine. Theory and Practice. *Bull. W.H.O.* **53**, 55-65 (1976).
56. Avrameas, S. Amplification Systems in Immunoenzymatic Techniques. *J. Immunol. Methods* **150**, 23-32 (1992).
57. Mattiasson, B. et al. Thermometric Enzyme Linked Immunosorbent Assay: Telisa. *Biochim. Biophys. Acta* **483**, 221-227 (1977).
58. Mattiasson, B. & Nilsson, H. An Enzyme Immunoelectrode. Assay of Human Serum Albumin and Insulin. *FEBS Lett.* **78**, 251-254 (1977).
59. Danielsson, B. The Enzyme Thermistor. *Appl. Biochem. Biotechnol.* **7**, 127-134 (1982).
60. Elder, M., *Point of Care Diagnostics*, BCC Research, (2014).
61. Gamez, A. et al. Toward Pku Enzyme Replacement Therapy: Pegylation with Activity Retention for Three Forms of Recombinant Phenylalanine Hydroxylase. *Molecular therapy : the journal of the American Society of Gene Therapy* **9**, 124-129 (2004).

62. Banta-Wright, S. A. & Steiner, R. D. Tandem Mass Spectrometry in Newborn Screening: A Primer for Neonatal and Perinatal Nurses. *J. Perinat. Neonatal Nurs.* **18**, 41-58; quiz 59-60 (2004).
63. Longo, N. et al. Single-Dose, Subcutaneous Recombinant Phenylalanine Ammonia Lyase Conjugated with Polyethylene Glycol in Adult Patients with Phenylketonuria: An Open-Label, Multicentre, Phase 1 Dose-Escalation Trial. *The Lancet* **384**, 37-44.
64. Newman, J. D. & Turner, A. P. F. Home Blood Glucose Biosensors: A Commercial Perspective. *Biosensors Bioelectron.* **20**, 2435-2453 (2005).
65. Soni, A. & Jha, S. K. A Paper Strip Based Non-Invasive Glucose Biosensor for Salivary Analysis. *Biosensors Bioelectron.* **67**, 763-768 (2015).
66. Agrawal, R. P. et al. Noninvasive Method for Glucose Level Estimation by Saliva. *J Diabetes Metab* **4**, 266 (2013).
67. Yetisen, A. K., Akram, M. S. & Lowe, C. R. Paper-Based Microfluidic Point-of-Care Diagnostic Devices. *Lab Chip* **13**, 2210-2251 (2013).
68. Davaji, B. & Lee, C. H. A Paper-Based Calorimetric Microfluidics Platform for Bio-Chemical Sensing. *Biosensors Bioelectron.* **59**, 120-126 (2014).
69. Son Vu Hoang, L. & Tadigadapa, S., presented at the Sensors, 2012 IEEE, 2012 (unpublished).

CHAPTER II

Isothermal Titration Calorimetry In Nanoliter Droplets With Sub-Second Time Constants[1]

By

Brad Lubbers & Franz Baudenbacher

Abstract

We reduced the reaction volume in microfabricated suspended-membrane titration calorimeters to nanoliter droplets and improved the sensitivities to below a nanowatt with time constants of around 100 ms. The device performance was characterized using exothermic acid-base neutralizations and a detailed numerical model. The finite element based numerical model allowed us to determine the sensitivities within 1% and the temporal dynamics of the temperature rise in neutralization reactions as a function of droplet size. The model was used to determine the optimum calorimeter design (membrane size and thickness, junction area, and thermopile thickness) and sensitivities for sample volumes of 1 nl for silicon nitride and polymer membranes. We obtained a model sensitivity of 153 $pW/Hz^{1/2}$ for a 1 μm SiN membrane and 79 $pW/Hz^{1/2}$ for a 1 μm polymer membrane. The time constant of the calorimeter system was determined experimentally by using a pulsed laser to increase the temperature of nanoliter sample volumes. For a 2.5 nanoliter sample volume, we experimentally determined a noise equivalent power of 500 $pW/Hz^{1/2}$ and a 1/e time constant of 110 ms for a modified commercially available infrared sensor with a thin-film thermopile. Furthermore, we

[1] Reproduced with permission from Lubbers, B. & Baudenbacher, F. Isothermal Titration Calorimetry in Nanoliter Droplets with Subsecond Time Constants. *Anal. Chem.* **83**, 7955-7961 (2011).

demonstrated detection of 1.4 nJ reaction energies from injection of 25 pl of 1 mM HCl into a 2.5 nl droplet of 1 mM NaOH.

Introduction

Isothermal titration microcalorimetry is one of the most powerful techniques to characterize chemical binding mechanism and biological processes through enthalpy changes at constant temperatures[1]. In a series of additions, reagent are injected into a sample volume under isothermal conditions and by integrating small temperature increases over time, as compared to the baseline temperature, reaction enthalpies are determined[2,3].

Micromachined membrane based calorimeters allow for a dramatic reduction in sample volumes and thermal mass and therefore enable measurements with very small heat capacities[4]. Combined with a sensitive thermometer relying on the Seebeck effect, these devices reach detection limits in the nanowatt range[5]. Since change in enthalpy is a nearly universal fingerprint of binding reactions and phase transitions, these devices are used in areas such as bioscience[6], biophysical chemistry[7], chemical engineering[8], drug development[9], antibody engineering[10] and cellular assays to determine cellular growths or metabolic rates[11].

Many biothermodynamic processes occur at characteristic time constants linked to intrinsic physical kinetics or metabolic/signaling activity of living cells. Of particular interest is protein binding/folding/unfolding[12], phase transitions,[4] or physiometry to determine the activity of living cells[13].

The reduction of the sample volume implies a decrease in the time constant; allowing the temporal dynamics of the chemical and biological processes become accessible. In this study we reduced the reaction volume to nanoliter droplets and utilized a membrane based calorimeter to

obtain time constants on the order of 100 ms and detection of nJ reaction energies. The response time of the system depends on the location of the heat generated, the diffusion of heat in the sample volume, and the thermal coupling of the sample volume to the heat sink. To understand these different contributions, we derived a detailed finite element model to represent the data and used the model to optimize the device performance.

Experimental Section

Sensor Description

In order to measure sub-nanowatt reaction enthalpies and characterize chemical processes, very small ΔT (<100 μK) must be detected. A commercial infrared (IR) radiation sensor (S-25, Dexter Research) was evaluated for calorimetry as the manufacturer states a sensitivity of 193 V/W, a time constant (τ) of 9 ms, and a moderate thermopile resistance of 23 KΩ, which defines the noise floor of the system. Since the sensor is designed for IR detection and not for calorimetry, the stated sensitivity and τ will vary due to the presence of the sample drop and the method of calibration. The sensor consists of 20 bismuth/antimony (Bi/Sb) thermopile junctions on a suspended 1.5 μm thick silicon nitride/silicon oxide membrane. A 0.5 mm deep by 2 mm wide chamber is formed on top of the membrane by the sensor casing and is an ideal size for holding small, nanoliter sample droplets (**Figure 4B**).

Amplifier Design

The intrinsic noise of the micromachined calorimeter is dominated by the Johnson-Nyquist noise of the thermopiles and can be described by the spectral noise density:

$$V_n = \sqrt{4\, k_B T R} \tag{11}$$

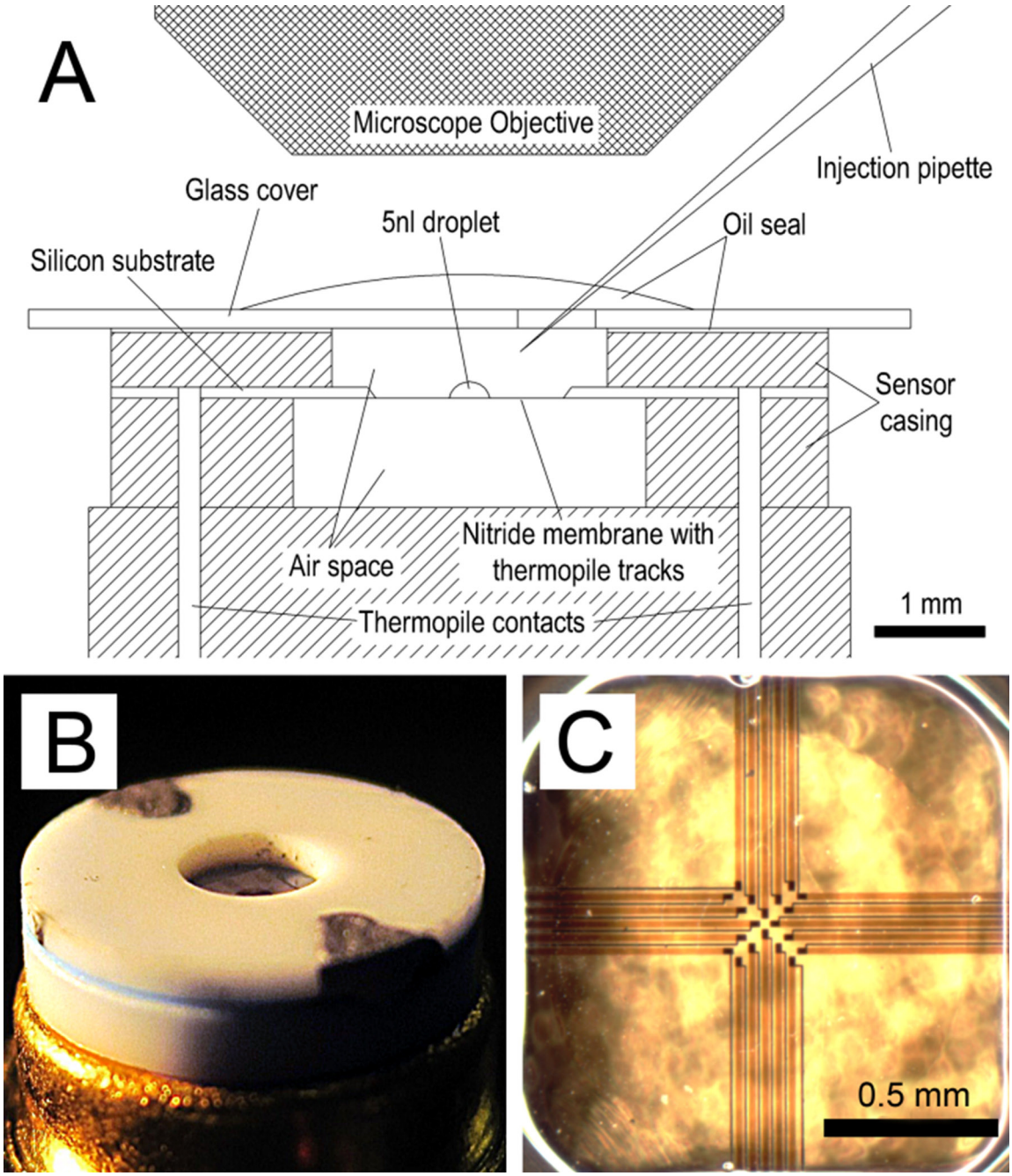

Figure 4. Device layout. (**A**) Side-view schematic of calorimeter setup showing chamber sealing with oil and sample delivery pipette. Additional shielding (not shown) around the sensor reduces thermal fluctuation noise. (**B**) Angle view of sensor showing sample well in center. (**C**) Top view of sensor membrane showing 20 Bi/SB thermopile junctions with an active area of 0.0625 mm^2 and sensitivity of 3600 μV/K.

where k_B is the Boltzmann's constant, T the resistors absolute temperature, and R the resistance of the thermopile. The 23 kΩ thermopile resistance results in a noise density of 19.4 nV/Hz$^{1/2}$. In order to operate the calorimeter close to the intrinsic noise floor, the amplifier noise should be much smaller so as not to contribute substantially to the overall noise. Since isothermal calorimeters are typically operated near DC, the contribution of flicker or 1/f noise from the amplifier often becomes a dominating factor. Therefore, we selected a zero offset DC chopper amplifier (LMP2021, National Semiconductor) as the amplifier for our read out circuitry. Noise spectra were measured using a 3265A Dynamic Signal Analyzer (Hewlett-Packard). The noise spectrum of our amplifier is essentially white with a noise floor of 15 nV/Hz$^{1/2}$, which leads to an overall sensor and amplifier noise of 30 nV/Hz$^{1/2}$ (**Figure 5**). Above 1.5 Hz, the sensor plus amplifier signal decreases due to the characteristics of the 7 Hz low pass filter.

The cutoff frequency of the amplifier depends on the thermal time constant, which in turns is a function of sample volume. At a minimum realistic sample volume of 2.5 nl we obtained a time constant of 110 ms or f_{-3dB} of 1.45 Hz. This represents the bulk time constant of the sensor and therefore we selected a cutoff frequency of 7 Hz to suppress 60 Hz line noise and reduce the Johnson noise bandwidth. The amplifier output was sampled using a National Instruments 12 bit PCI-6024E A/D card. Through oversampling and decimation, its effective bit count was increased to 16 and therefore the digitization noise was reduced to 7 nV/Hz$^{1/2}$ at a gain of 25,000. All measurements were performed at room temperature (22-24 °C). During setup and measurements, the chamber of the sensor was covered by a glass cover slide with an access hole drilled for sample delivery (**Figure 4**). The cover slide was sealed with mineral oil to prevent sample evaporation. Thermal fluctuations were greatly reduced by adding additional copper shielding to the sensor casing. Without the additional thermal shielding the sensor was extremely

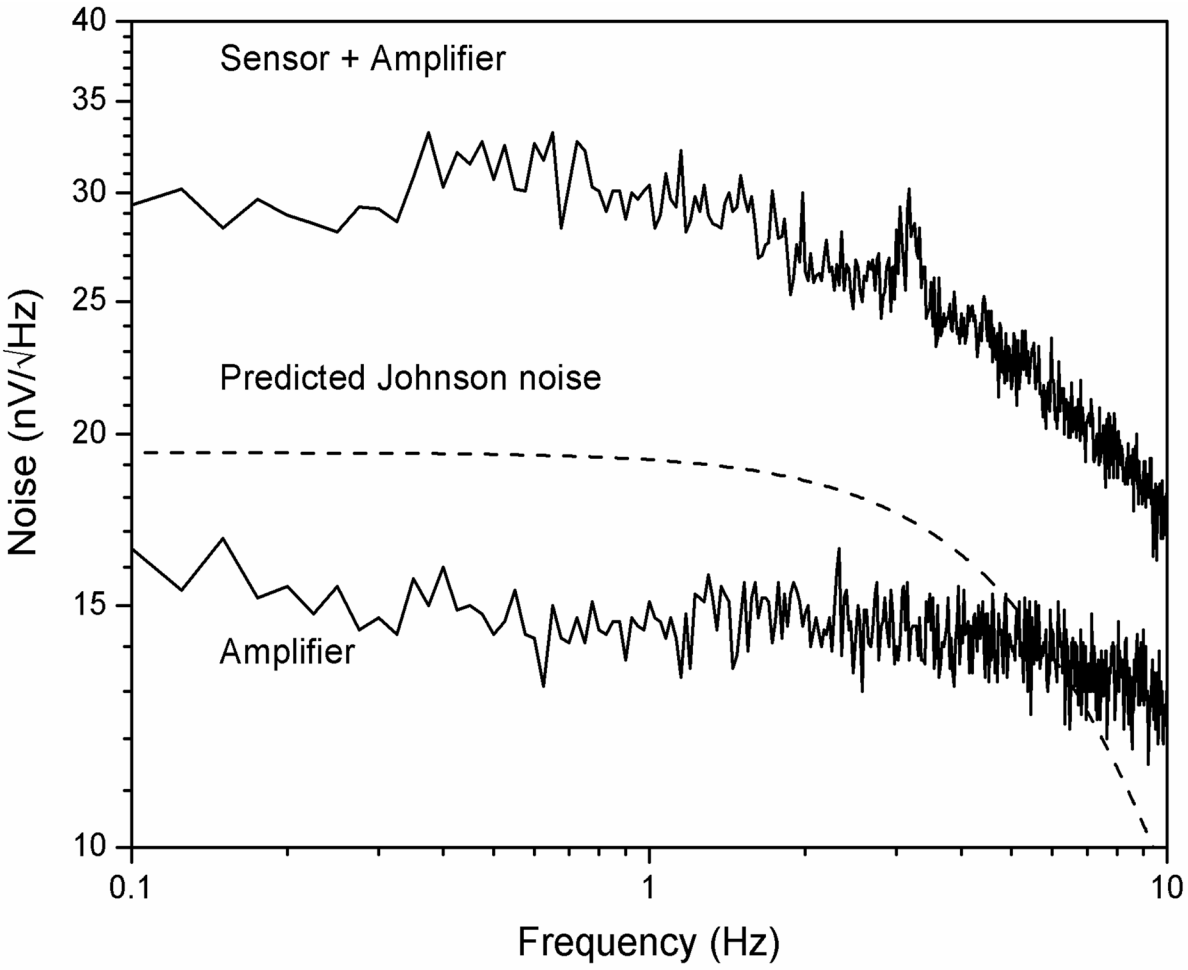

Figure 5. Noise spectral density of the amplifier, sensor, and calculated Johnson noise of the sensor, all at a 7 Hz cutoff. The combined sensor and amplifier noise is 30.1 nV in a 1 Hz bandwidth and free of 1/f noise.

susceptible to any air drafts or changes in the ambient temperature. In addition, the grounded copper ring and a metal amplifier enclosure reduced EMF noise. The combined effects of the low noise amplifier, shielding, and filtering reduced the RMS noise to 30.1 nV in the 0-1 Hz bandwidth and the peak-to-peak noise of the system to approximately 290 nV over a 10 second window under actual experimental conditions.

Sample Delivery

Liquid sample injections were performed using a micromanipulator (MP-285, Sutter Instrument Co.) and a pressure driven injection system (PicoSpritzer II, Parker Hannifin Corp.), both controlled through LabVIEW (**Appendix C**). This allowed automated pipette placement and sample injection of sample volumes between 25 pl and 50 nl onto the sensor. Pipettes were prepared by pulling on a Flaming/Brown pipette puller (P-87, Sutter Instrument Co.) and fire polished to a 1-20 μm ID using a microforge (MF-9, Narishige). Pipettes were calibrated before and after measurements by making repeated injections into a small diameter tube and measuring the total volume dispensed. In comparison to microfluidic based calorimeter devices, there is no noise contribution from the flow of reactants[14]

Sample Stabilization

Since our sample volume is a free standing nl sized droplet, evaporation is a major issue. In an unsealed sensor chamber, 2.5 nl of water would evaporate in a few seconds, so we have to stabilize the sample volume and reduce evaporation. The main strategy involved the use of a glass lid with a sealed sample injection port (**Figure 4A**). Since pipette access to the sensor surface was necessary for sample delivery, mineral oil was used as vapor tight seal that a micron sized delicate pipette tip could penetrate. However, sample evaporation was never completely reduced to zero and becomes critical as the sample volume is reduced[14]. For example a 5 nl water drop left on the sensor overnight would evaporate completely. This residual evaporation leads to a constant cooling flux and offsets the sample temperature slightly but measurably from the ambient temperature. The offset was integrated over the time it took for the evaporation of the droplet and was equivalent to the enthalpy of vaporization of the sample volume at the beginning. As the evaporating droplet changes geometry or droplets are injected, the evaporative

flux will be altered. Therefore, injections of liquid reagent into a sample drop results in a lower signal baseline (**Figure 6**). When smaller water drops were repeatedly injected to increase the base droplet, it was found that the baseline shift scaled with the change in surface area of the drop (**Figure 7**). Though the evaporative flux per area remains constant during an experiment, it

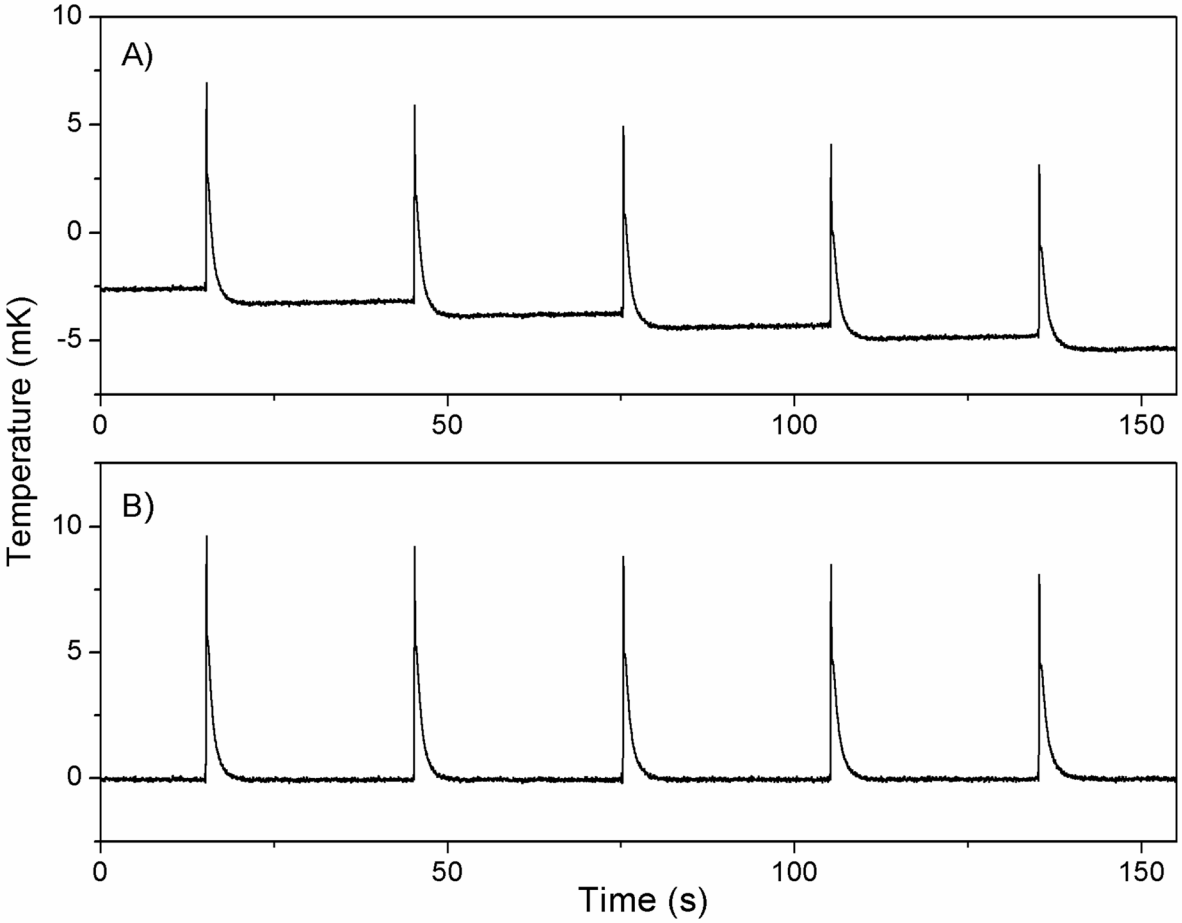

Figure 6. Baseline correction. A series of 100 pl injections of 0.05M HCl into 2.5 nl of 0.05M NaOH obtained for calibration. (**A**) Raw data and (**B**) data with the baseline shift and offset corrected for.

varies between experiments due to changes in sensor sealing efficiency. In order to account for the baseline shift when determining the energy evolved in a reaction, the shift occurs instantly and can be approximated as a step function with amplitude y. When the signal is convolved with a step function of amplitude -y, the original signal can be easily recovered (**Figure 6B**). The

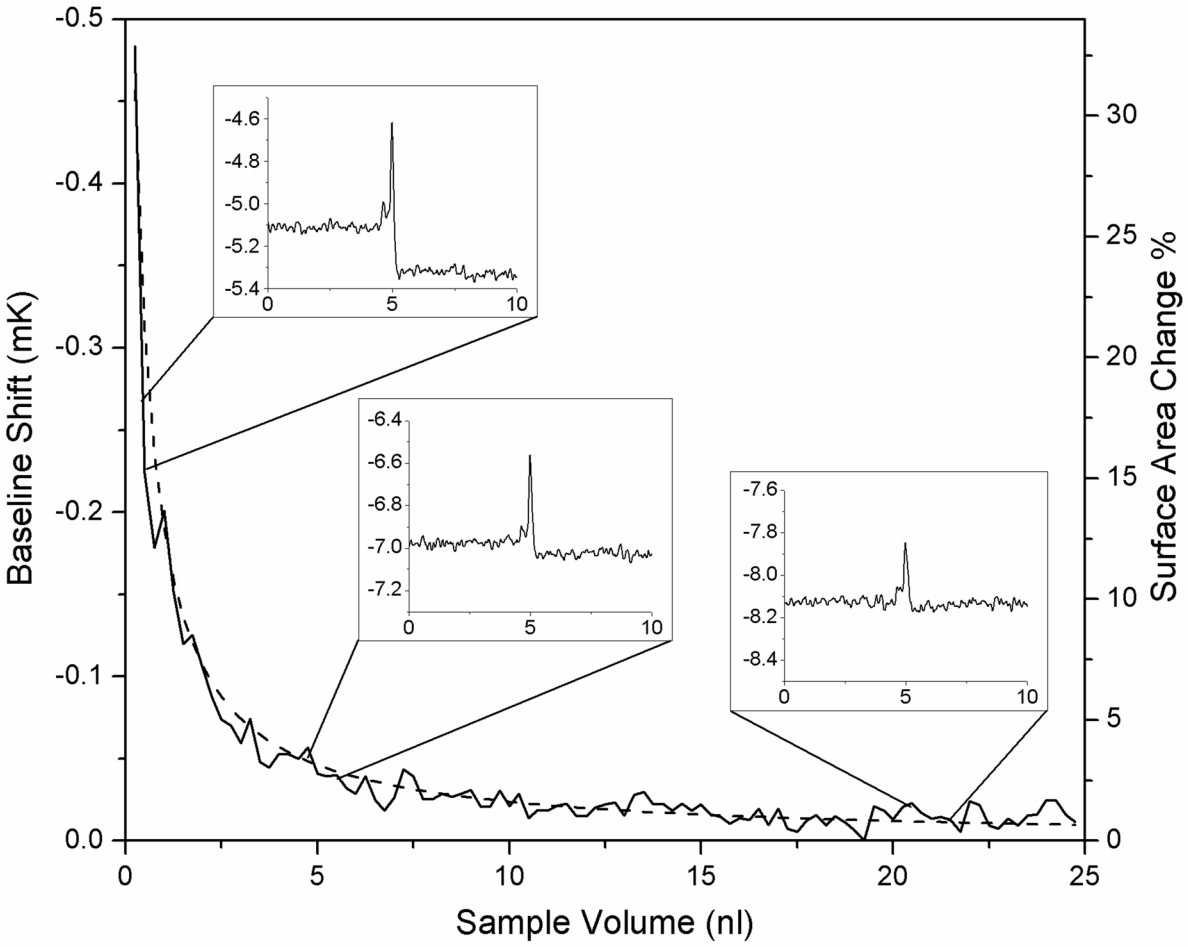

Figure 7. Baseline shift to volume relationship. Shift in baseline of water droplets injected with 250 pl of additional water (inserts). The baseline shift scales with the surface area change (dashed line) of the drops due to the increased evaporative flux from the drop surface. The positive spikes during injection are due to the ΔT between the injected water and the cooled base droplet.

evaporative sample cooling leads to a temperature difference (ΔT) between the sample volume and the injected reactants. This temperature difference causes a slight peak during any injection and the peak energy equals the specific heat of the injected sample multiplied by ΔT. The water injection peaks in **Figure 7** have energies of 4.6 – 8.2 nJ, giving a calculated ΔT of 4.8 – 8.6 mK which is a realistic ΔT. We were able to eliminate, and even drive this peak negative, by holding the base drop several mK above ambient temperature using a focused laser.

Time Constant Measurements

The sensor time constant (τ) was measured at different sample volumes using a 650 nm laser as a heat source. The laser was focused through the microscope optics to a point in the center of the sensor ~100 μm wide. Starting with an empty membrane, the laser was pulsed slowly (0.1 Hz) and 1 nl of ddH_2O was repeatedly injected onto the sensor until 50 nl was reached. τ was calculated from the 1/e rise and fall time at 0-50 nl using MATLAB (**Appendix A**).

Sensitivity Calibration

Sensitivity was determined using the neutralization reaction between HCl and NaOH. Stocks of HCl and NaOH were freshly prepared in ddH_2O at concentrations of 0.01 M, 0.05 M, 0.1 M, and 0.5 M filtered with a 0.22 μm syringe filter before use. New glass pipettes were used each time to prevent contamination and tip fouling. To calibrate, a drop of NaOH between 2.5-50 nl was injected onto the sensor membrane and allowed to stabilize resulting in a flat temperature baseline. Then, a pipette containing HCl was used to inject small (0.5%-2% of base drop) volumes of HCl into the center of the NaOH drop. Identical molarity of the acid and base were used to eliminate dilution effects. The signal output was recorded in LabVIEW (**Appedix C**) and then exported to MATLAB for data analysis (**Appendix A**). Sensitivity was determined by integrating the area under the curve from the exothermic reaction and dividing by the predicted reaction energy.

Sensor Modeling

In order to validate our findings and provide insights on how to optimize measurement sensitivity, a 2-D radial heat conduction model of the sensor was constructed in Comsol

Multiphysics. The model included the sensor casing, glass cover, Si substrate, membrane, thermopiles, air spaces, and sample droplet. The heat origin was a sphere the same size as the injected HCl in the middle of the NaOH drop. Since some parameters (membrane thermal conductivity (G_{mem}) and total thermopile Seebeck coefficient (S_{tot})) were not provided by the sensor manufacturer, these were determined by least squares fitting of the model to experimental data. Using these parameters, sensitivity and τ were calculated in MATLAB using the Comsol data at several volumes between 0-50 nl. This model was then utilized in designing a 2nd generation calorimeter with optimized dimensions at small sample volumes for improvements in sensitivity and τ (**Appendix B**).

Results and Discussion

Modeling

The use of Comsol Multiphysics allowed for rapid modeling and the ability to least squares fit the modeling parameters to the experimental data in MATLAB. The three main parameters characterizing a calorimeter are power sensitivity (P), minimum detectable power (Pmin), and time constant (τ). They are related through the following equations:

$$P = S_{tot}/G_{tot} \tag{12}$$

where S_{tot} is the total Seebeck coefficient of the thermopiles and G_{tot} is the total thermal conductance away from the sample drop. The minimum detectable power is predicted by:

$$P_{min} = \Phi/P \tag{13}$$

where Φ is the total electronic and thermal noise of the system. The temporal response is predicted by

$$\tau = C_{tot}/G_{tot} \quad (14)$$

where C_{tot} is the total thermal mass of the sample and device. Since S_{tot} and Φ are intrinsic quantities of the device, G_{tot} and C_{tot} are the only variables dependent on the droplet size. C_{tot} can be calculated from the sample and membrane mass, however G_{tot} encompasses all heat fluxes away from the sample through the membrane, thermopiles, air, and radiation. Therefore, a numerical model of the device is required to predict G_{tot}.

Ideally, a full 3-D model would be used to encompass all device geometries. However, the thin 1.5 μm thick membrane in combination with a 2 mm wide chamber resulted in an overly complex mesh that could not be solved efficiently. Therefore, we pursued a radial 2-D model. The only feature of the sensor not radially symmetric was the thermopile traces, as can be seen in **Figure 4C**, so the thermal conductivity of the thermopile traces was combined into the overall conductivity of the membrane (G_{mem}). Though constant, initially the Seebeck coefficient was unknown and not provided by the device manufacturer. Based on the dimensions and resistance of the thermopile traces, it was presumed that they were made of bismuth and antimony. Bi/Sb thermopiles are reported to have thermopowers of 90-410 μV/K per junction depending on dopants and crystal orientation[15]. Even if the exact composition of the materials was known, it would still be difficult to predict their properties as these deviate from the normal bulk properties in thin films[16]. It would also be difficult to determine experimentally the thermopower of our sensor by applying a known temperature difference across the thermopile due to its small size and high sensitivity. Instead, it was easier to fit the model to independent experimental calibrations at various different sample volumes. As can be seen in **Figure 8**, by varying G_{mem}, S_{tot}, and the location of the heat origin, the model can be fit to the data accurately, in terms of both amplitude and temporal response. G_{mem} most directly affected τ, while S_{tot} is a scaling

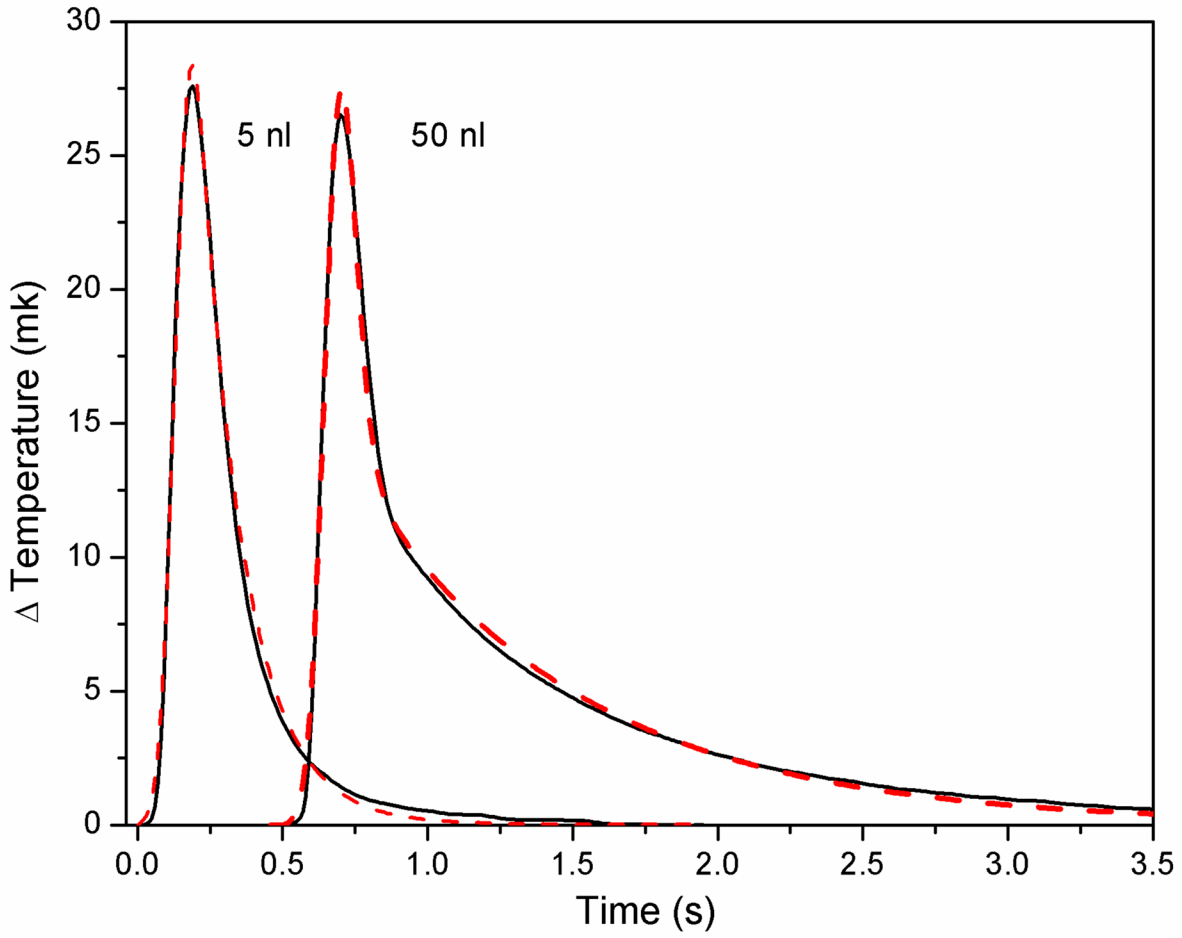

Figure 8. Exothermic acid-base neutralizations used for calibration at 5 and 50 nl. The experimental data (solid lines) are well predicted by the modeling results (dashed). 100 pl of 0.1 M HCl was injected at 0 s into 5 nl of 0.1M NaOH yielding 0.565 μJ. 500 pl of 0.1 M HCl was injected at 0.5 s into 50 nl of 0.1M NaOH yielding 2.83 μJ.

factor, as expected from equations 12 and 14. The residual sum of squares of the data in **Figure 8** showed less than 1% error between the experimental and modeling data. The least square fitting gave similar values of G_{mem} (18.9 +/- 0.79 W/ (m·K)) and S_{tot} (3590 +/- 260 μV/K) regardless of the sample volume or energy evolved. This high S_{tot} value combined with the low noise floor yields a temperature sensitivity of 25 $\mu K/Hz^{1/2}$. This represents a threefold improvement in RMS noise compared to our previous work[5] and a 10 fold improvement in temperature resolution over microfluidic based calorimeter devices[17]. The model also showed that the location of the heat

origin in the base droplet could significantly affect the results. The shoulder seen at 1.0 s in the 50 nl sample in **Figure 8** varied depending on the heat origin location and disappeared when the heat origin was near the top of the sample drop. However, this reduced the curve areas and sensitivity by 30%. The effect decreased to <7% at smaller drop sizes as the volume-to-surface-area ratio of the drop decreased.

Determination of the Power Sensitivity

The acid-base neutralization injections provided a straightforward way to calibrate our sensors. Unlike calorimeters utilizing a built in heater for calibrations, our sensors are calibrated in the same fashion in which they will be used. Resistor heating on the underside of the membrane produces localized heating at the thermopile junctions and a temperature gradient throughout the sample[14]. This can lead to overestimations of sensitivity and does not take into account properties like surface area changes and finite diffusion rates that occur during reactant injections[18]. The binary reaction of HCl and NaOH was chosen for calibrations due to fast diffusion and reaction rates. When low concentration HCl is injected into an excess of equimolar concentration NaOH, the reaction occurs almost instantaneously and with very little variation between injections due to dilution of the NaOH[18]. Diffusion modeling of dilute HCl diffusion within our samples revealed that it could take up to 10 s to reach 99% uniformity. However, in all experimental cases, the reactions appeared to occur in <200 ms. This can be seen in **Figure 8** where the time from the start of the injections at 0.1 s to the peaks is ~150 ms. The faster than expected reaction is likely due to the turbulent flow produced during injection and the reaction completing long before concentration equilibrium was reached.

The calibration results show that a sensitivity of up to 60 V/W can be achieved by reducing the sample volume to 2.5 nl which was verified by the model results (**Figure 9**). In

Figure 9, each triangle represents an individual injection of 0.05 M HCl into 0.05 M NaOH and each has been corrected for baseline shift and ΔT at the time of injection. Calibrations were also performed at 0.01 M, 0.1 M, and 0.5 M to verify further the results. From this, the experimental sensitivity can be predicted empirically by:

$$P_{exp} = 88.07 \times Volume^{-0.409} \quad (15)$$

with an R^2 = 0.992 for 2.5 to 60 nl. The noise equivalent power of 0.5 nW/Hz$^{1/2}$ at 2.5 nl translates to a minimum power resolution of 1.5 nW/Hz$^{1/2}$ at a SNR of 3:1. To verify these results, model predictions of G_{tot} and S_{tot} were fed into equation 12 and the result matched well with the experimental data (**Figure 9**). The model revealed that G_{tot} ranged from 65 μW/K at 2.5 nl to 220 μW/K at 50 nl, with the membrane providing the main heat flow path away from the sample drop. G_{tot} increased at larger sample volumes due to the increase in surface area and the shortening of the distance between the sample and sidewalls. The near exponential increase in power sensitivity at smaller sample volumes motivated the investigation of even smaller sample volumes. Although 2.5 nl was the minimum stable droplet size in our current setup, the model was used to determine sensitivities at reduced volumes. The maximal sensitivity of 80 V/W achieved near zero volumes shows further reductions in sample volume does not led to dramatic improvements in sensitivity with our current device as would be predicted from equation 5 (**Figure 9**).

The calculated maximal sensitivity of 80 V/W falls short of the sensor manufactures claim of 193 V/W. This is due to differences in calibration procedures. The manufacturer calibrated under argon gas using a blackbody radiation source that heated the entire membrane surface while the model utilizes a small heat source that localizes the heat to a few micron area in

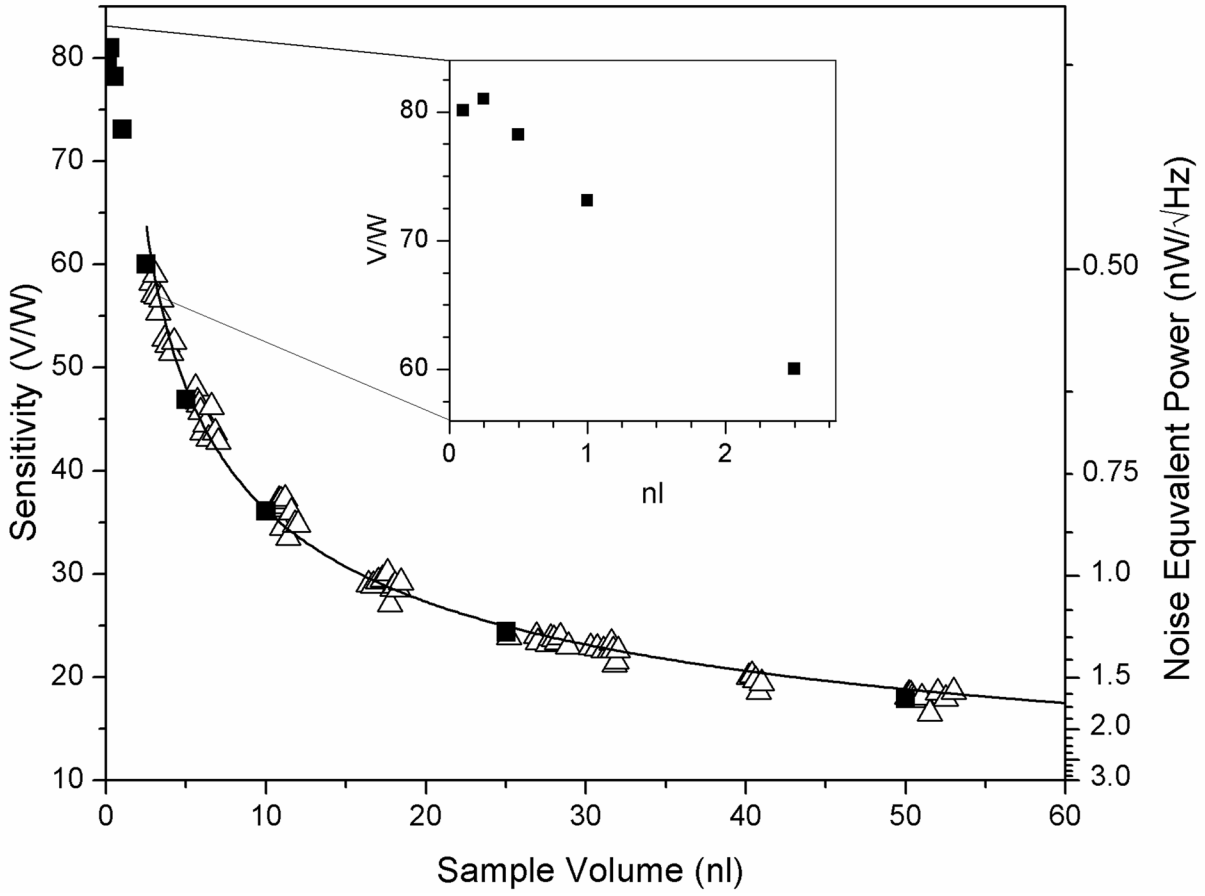

Figure 9. Experimentally determined sensitivity (Δ) determined with acid-base neutralizations. 2.5 nl is an experimental practical limit due to drop instability at small volumes. Model data (■) shows that the ultimate limit of the sensor is ~80 V/W at 0 nl sample volume. The experimentally obtained sensitivity at 2.5 nl, in conjunction with the low noise amplifier, gives an NEP of 500 pW/Hz$^{1/2}$.

the center of the membrane. When the manufacturer's methods were implemented in the model using our derived parameters, a sensitivity of 190 V/W was attained.

Device Optimization

Modeling revealed important information about our sensor that allowed us to find areas for improvement in its design. In an optimal device, S_{tot} must be maximized while C_{tot}, G_{tot}, and noise minimized. These parameters are determined by factors including the composition, thickness, and area of the membrane and thermopile, number of junctions, and sample droplet volume. Our current minimum sample volume of 2.5 nl is dictated by evaporative losses and

sample delivery inaccuracy. Improvements in these areas could enable a minimum sample volume of 1 nl which would improve both τ and G_{tot} according to our model. Assuming a fixed sample volume of 1 nl it was then possible to find the optimal device dimensions and geometry. At first glance an increase in the number of thermopile junctions through feature size reduction would seem to benefit P_{min} by increasing S_{tot}; however any benefit is equally offset by an increase in noise. With the best amplifiers typically contributing at least 5 $nV/Hz^{1/2}$ noise[19], it provides little benefit to reduce V_n past that level. It is more advantageous to keep V_n around 10 - 15 $nV/Hz^{1/2}$ so that amplifier noise is not a dominant factor. Therefore, calculations for P_{min} were carried out with enough junctions to keep V_n in that range.

Since the membrane is the dominant factor in G_{tot}, using a membrane material with a lower G_{mem}, like a polymer, P_{min} could be improved and at the same time the dependence on membrane thickness by Pmin is reduced (**Figure 10C**). The limiting factor is mechanical stability of the thin membranes, with 1 μm being a realistic minimum thickness[20]. By using previously reported membranes like Su-8[21] or parylene-C[17], membrane heat flux could be reduced from 70% to 5% of G_{tot}. However, even with our current G_{mem}, higher sensitivities than previous studies[17] can be achieved due to our higher S_{tot}. The Bi/Sb thermopiles used in our current device are ideal in terms of high Seebeck coefficient and low resistance. While optimizing the thermopile thickness we found that decreased thickness leads to reduce G_{tot} are at the expense of noise (**Figure 10D**). We selected the ideal thermopile thickness to be 1μm for SiN membranes and 0.5 μm for polymer membranes. It is advantageous to have a large membrane area in order to reduce G_{tot}, however as membrane size increases, thermopile length also increases, resulting in increased Johnson-Nyquist noise. Similarly, higher ΔT is realized at the thermopile junctions when they are situated centrally under the sample droplet, but this leads to

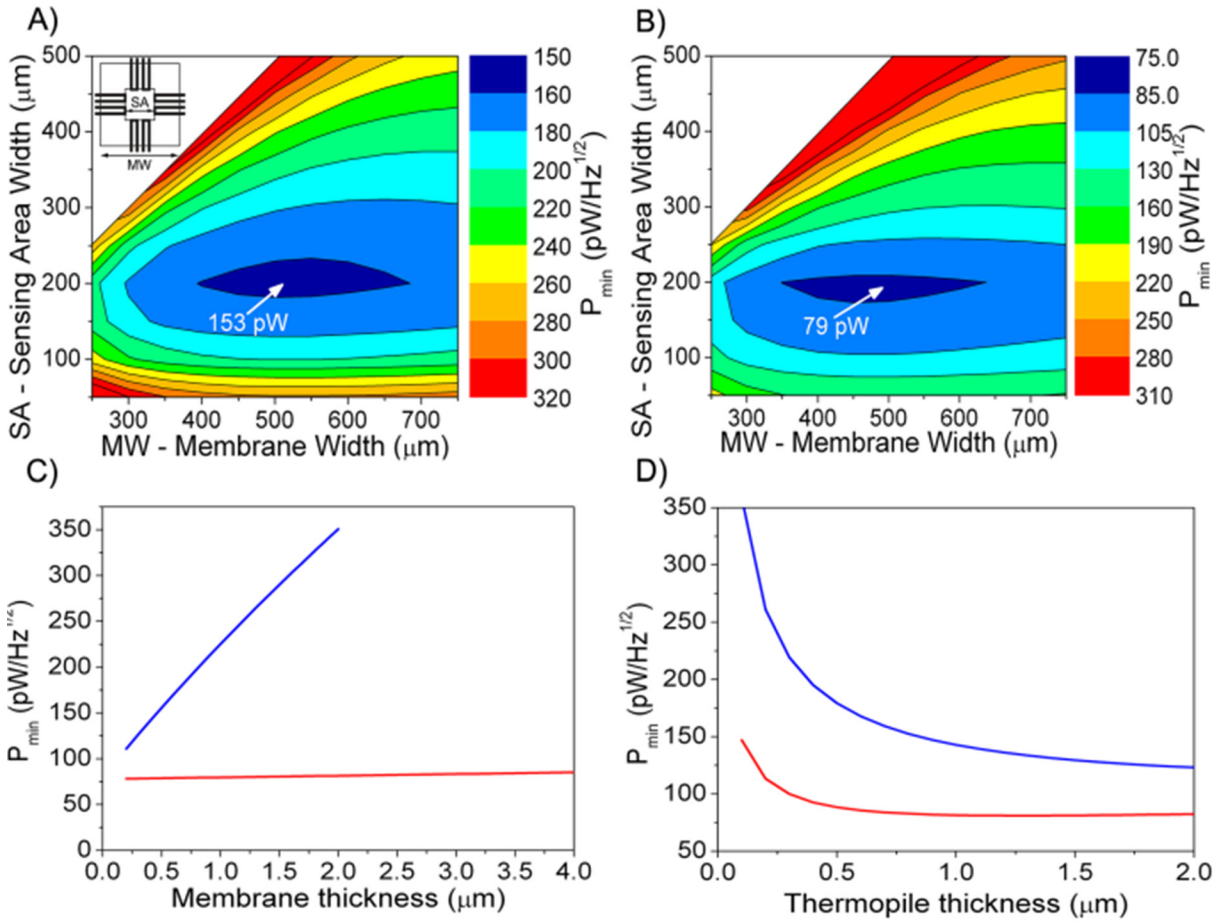

Figure 10. Device modeling. (**A**) Contour plot showing how the minimum detectable energy changes as a function of membrane size and junction area for a 1 nl sample drop on a 1 μm SiN membrane. The best P_{min} is achieved at a membrane size of 500 μm and a junction size of 200 μm. (**B**) Similar dimensions were found for a 1um thick polymer membrane, but with a lower resulting P_{min}. (**C**) P_{min} is influenced much more by membrane thickness in SiN based (blue line) than polymer based (red line) calorimeters. (**D**) Increasing thermopile thickness decreases noise (dotted line) and improves P_{min} for SiN (blue line) and polymer (red line) based calorimeter.

more noise due to longer junctions and increases G_{tot} through conduction along the thermopile traces. By modeling a matrix of different sensing area widths (SA) and membrane widths (MW) using parameters from previous modeling, we found minima for both SiN and polymer membranes (**Figure 10A,B**). For both membranes, the optimal SA was ~200 μm wide, placing the thermopile junctions just at the edge of a 1 nl droplet. This optimization also revealed the 2 fold improvement in P_{min} by using a polymer membrane over a SiN membrane (**Figure 10A,B**).

Error

A source of error in these reactions can be attributed to injection volume uncertainties. The PicoSpritzer II injection system used relies on air pressure and not on positive displacement to deliver samples. At small (<100 pl) injection volumes, this results in short (<20 ms) injection pulses that are not far above the 3 ms air valve opening time. Random error determined experimentally with a series of injections is greatest at 2.5 nl base volume with a relative standard deviation of 2.3%, decreasing to 1.2% at 50 nl. Additional error is introduced at small volumes due to changes in the base drop volume. If the injection of reactants changes the base drop volume from 2.5 to 3.0 nl, sensitivity drops from 60.5 to 56.1 V/W, as shown in **Figure 9** and in the decrease in peak amplitude seen in **Figure 6**. To attain sample volumes below 2.5 nl a more accurate injection system and better evaporation control is needed.

Determination of Time Constant

Time constant measurements of the system are higher than predicted by equation 4, but verified by the numerical model (**Figure 11**). Since τ was determined empirically by applying a 650 nm laser heating step function to the sensor with various volumes of water on it, little energy was absorbed by the water drop. Most of the energy was deposited at the opaque SiN membrane surface, causing localized heating near the thermopiles. This causes an error in equation 14 since it assumes that the entire sample volume is heated uniformly. It also does not take into account differences in temperature distribution over the sample and membrane surfaces. When the model was changed from a point heat source to a constant heating throughout the sample, comparable time constants with the results from equation 14 were produced. The actual τ from a reaction on the calorimeter would be somewhere between the two findings. The laser heating results mimic what would occur in a chemical reaction where the reactants proceed to completion in a small

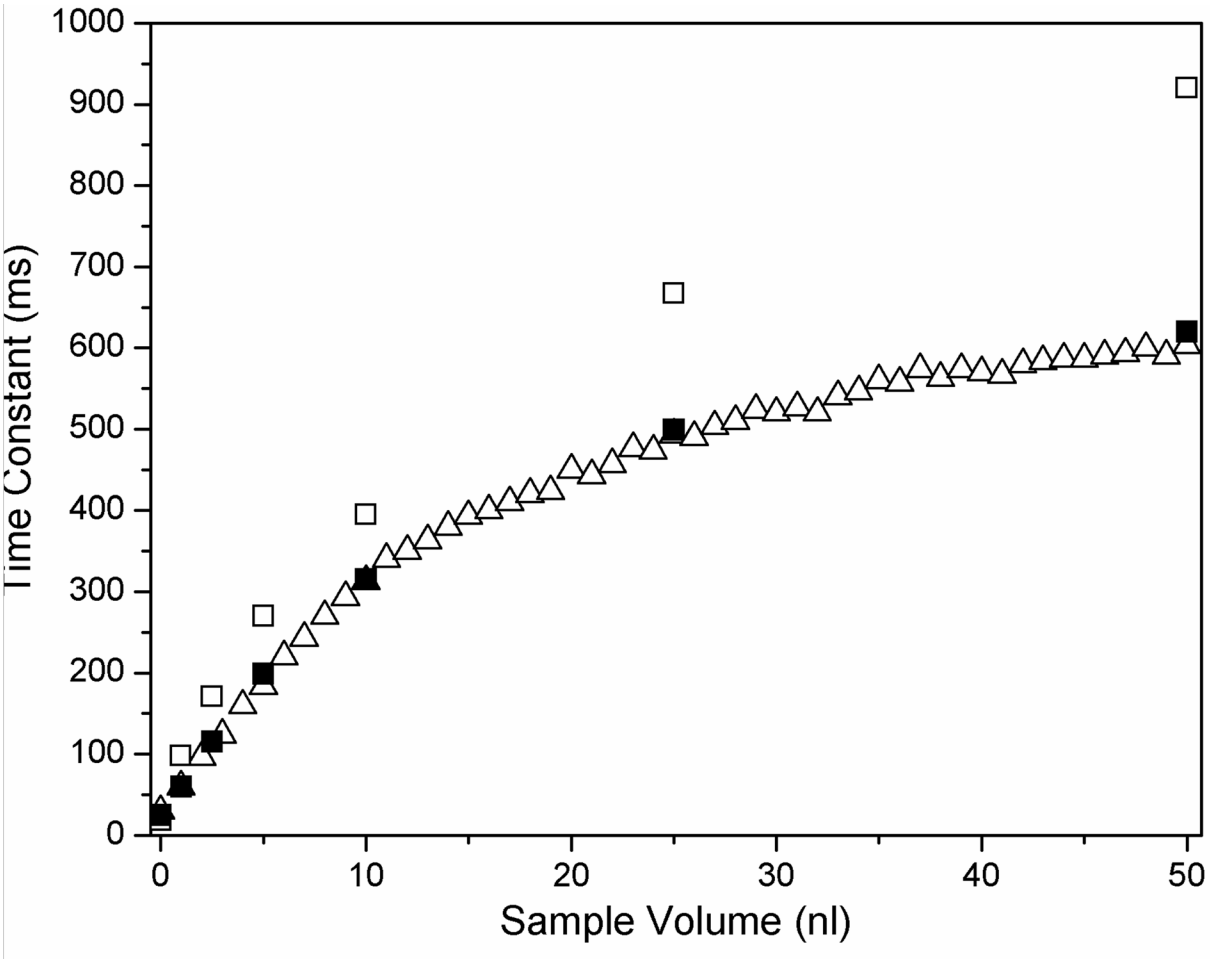

Figure 11. Time constant measured using a pulsed laser heat source at incrementally increased drop volumes (Δ) is matched well by the model data (■) and shows τ of 110 ms at 2.5 nl sample volume. However, when τ is calculated from C_{tot}/G_{tot}, the results (□) are different due to localized drop heating.

volume of the total sample. The same would also be true in a biological assay where the cells would settle to the bottom of the sample drop. Even the worst case scenario of a τ of 170 ms for a 2.5 nl sample is still much better than other calorimeters with comparable sensitivity[17]. These finding give justification for utilizing smaller sample volumes in future calorimeter designs.

Minimum Detectable Energy

P_{min} as predicted by equation 13 and shown in **Figure 9** is 0.5 $nW/Hz^{1/2}$ at 2.5 nl and translates to a minimum power resolution of 1.5 $nW/Hz^{1/2}$ at a SNR of 3:1. Nanowatt resolution

energy measurements were performed using our current calorimeter setup and achieved this level of sensitivity. When small droplets (12.5 pl – 800 pl) of dilute HCl were injected into a 2.5 nl drop of NaOH, as little as 1.4 nJ could be detected (**Figure 12A**). At 0.7 nJ, the peak was too small to be seen against the noise background. Injection artifacts were not seen until at least 100 pl of reactant was being injected (**Figure 12B**). The short time constant in conjunction with high sensitivity allows for the detection of these small, fast peaks that would be missed using other calorimeters.

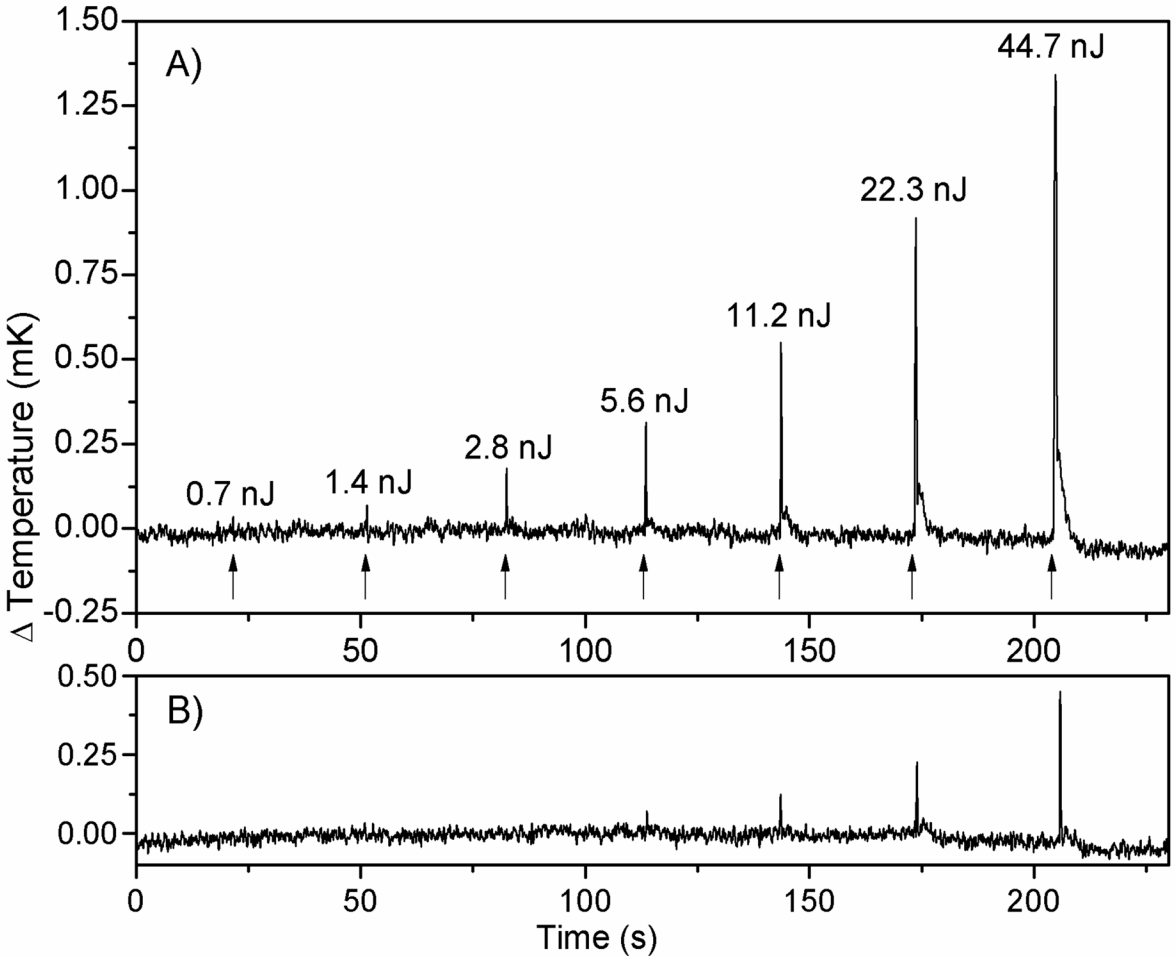

Figure 12. Sample injections. (**A**) HCl injections into a 2.5 nl NaOH drop at each arrow showing the sub-nW capabilities of the sensor. (**B**) Control injections of an equivalent volume of water into a 2.5 nl water drop.

Conclusions

We have described the use and optimization of a highly sensitive calorimeter which exceeds the capabilities of previously described calorimeters in both sensitivity and temporal response. Through reduction in sample volume and improvements in calibration, we showed, at 2.5 nl sample volume, a functional power resolution of 1.5 $nW/Hz^{1/2}$ and a sensitivity of 60 V/W, both an order of magnitude better than previously reported[5,17,20]. The reduction in sample volume also greatly enhanced τ, allowing for the first time sub-second measurements at high sensitivity. Modeling of the calorimeter allowed us to verify our results and determine if extending sample volumes smaller was warranted. Since only a 25% gain was predicted, we focused on using the model to design a calorimeter optimized for 1 nl samples. This showed the possibility for a polymer based calorimeter with P_{min} of less than 100 $pW/Hz^{1/2}$ and τ of 160 ms. Sub-nanowatt sensitivities and short time constants are essential for monitoring dynamic non-equilibrium biomolecular processes with brief intermediate states like protein folding or cellular metabolism. Furthermore, these micromachined membrane based nano-calorimeters in combination with advanced electrowetting liquid handling techniques[22] could be operated in an array format required for combinatorial chemistry and drug discovery.

Acknowledgements

This work was supported in part by NIH Grant U01AI061223, the Vanderbilt Institute of Integrative Biosystems Research and Education (VIIBRE). We are especially indebted to Joseph Sun for his help in developing the finite element model. Furthermore we thank Joel Tellinghuisen and John Wikswo for helpful discussions.

References

1. Falconer, R. J. et al. Survey of the Year 2008: Applications of Isothermal Titration Calorimetry. *J. Mol. Recognit.* **23**, 395-413 (2010).
2. Hansen, L. D., Fellingham, G. W. & Russell, D. J. Simultaneous Determination of Equilibrium Constants and Enthalpy Changes by Titration Calorimetry: Methods, Instruments, and Uncertainties. *Anal. Biochem.* **409**, 220-229 (2011).
3. Wiseman, T. et al. Rapid Measurement of Binding Constants and Heats of Binding Using a New Titration Calorimeter. *Anal. Biochem.* **179**, 131-137 (1989).
4. Cooke, D. W., Michel, K. & Hellman, F. Thermodynamic Measurements of Submilligram Bulk Samples Using a Membrane-Based "Calorimeter on a Chip". *Rev. Sci. Instrum.* **79**, 053902 (2008).
5. Xu, J. et al. A Microfabricated Nanocalorimeter: Design, Characterization, and Chemical Calibration. *Anal. Chem.* **80**, 2728-2733 (2008).
6. Roselin, L. et al. Recent Trends and Some Applications of Isothermal Titration Calorimetry in Biotechnology. *Biotechnol. J.* **5**, 85-98 (2010).
7. Ball, V. & Maechling, C. Isothermal Microcalorimetry to Investigate Non Specific Interactions in Biophysical Chemistry. *International journal of molecular sciences* **10**, 3283-3315 (2009).
8. Carreto-Vazquez, V. H. et al. Chip-Scale Calorimeters: Potential Uses in Chemical Engineering. *J. Loss Prev. Process Indust.* **24**, 34-42 (2011).
9. Ferenczy, G. G. & Keserue, G. M. Thermodynamics Guided Lead Discovery and Optimization. *Drug Discov. Today* **15**, 919-932 (2010).
10. Manta, B. et al. Tools to Evaluate the Conformation of Protein Products. *Biotechnol. J.* **6**, 731-741 (2011).
11. Vine, G. J. & Bishop, A. H. The Analysis of Microorganisms by Microcalorimetry in the Pharmaceutical Industry. *Curr. Pharm. Biotechnol.* **6**, 223-238 (2005).
12. Khan, S. H. et al. Protein-Protein Interactions: Principles, Techniques, and Their Potential Role in New Drug Development. *J. Biomol. Struct. Dyn.* **28**, 929-938 (2011).
13. Verhaegen, K. et al. A High-Throughput Silicon Microphysiometer. *Sensor Actuat a-Phys* **82**, 186-190 (2000).
14. Wadso, I. & Wadso, L. Systematic Errors in Isothermal Micro- and Nanocalorimetry. *J. Therm. Anal. Calorim.* **82**, 553-558 (2005).
15. Boyer, A. & Cisse, E. Properties of Thin-Film Thermoelectric-Materials - Application to Sensors Using the Seebeck Effect. *Materials Science and Engineering B-Solid State Materials for Advanced Technology* **13**, 103-111 (1992).
16. Bourque-Viens, A. et al. Modelling and Experimental Validation of Thin-Film Effects in Thermopile-Based Microscale Calorimeters. *Sensor Actuat a-Phys* **150**, 199-206 (2009).
17. Lee, W. et al. High-Sensitivity Microfluidic Calorimeters for Biological and Chemical Applications. *Proc. Natl. Acad. Sci. U. S. A.* **106**, 15225-15230 (2009).
18. Briggner, L. E. & Wadso, I. Test and Calibration Processes for Microcalorimeters, with Special Reference to Heat Conduction Instruments Used with Aqueous Systems. *J. Biochem. Biophys. Methods* **22**, 101-118 (1991).
19. Klushin, A. M. et al. Dc Voltage Calibrator Based on an Array of High-Temperature Superconductor Josephson Junctions. *IEEE Transactions on Instrumentation and Measurement* **52**, 529-532 (2003).

20. Johannessen, E. A. et al. A Suspended Membrane Nanocalorimeter for Ultralow Volume Bioanalysis. *IEEE Trans Nanobioscience* **1**, 29-36 (2002).
21. Mattsson, C. G. et al., *IEEE Sensors 2007* (Atlanta, GA, 2007), pp. 836-839.
22. Wheeler, A. R. et al. Electrowetting-Based Microfluidics for Analysis of Peptides and Proteins by Matrix-Assisted Laser Desorption/Ionization Mass Spectrometry. *Anal. Chem.* **76**, 4833-4838 (2004).

CHAPTER III

Nanoliter Droplet Based Calorimeter For Point Of Care ELISA[2]

By

Brad Lubbers, Raymond Mernaugh, Elliott Dawson, & Franz Baudenbacher

Abstract

Droplet based microfluidic systems can produce well defined nanoliter sized reaction volumes for high throughput chemical and diagnostic applications. We developed a calorimeter system for nanoliter droplets with a minimum detectable power of 375 $pW/Hz^{1/2}$. This allows for the detection of 4 femtomoles of hydrogen peroxide, or the energy output of 6 attomoles of HRP. We exploited the performance of the system to quantify therapeutic concentrations of the anticancer monoclonal antibody (trastuzumab) in a nanoliter of serum utilizing Thermometric ELISA. This is the first time a nano-calorimetry system is used for a clinically relevant assay. We attained excellent sensitivities and reduced serum matrix effects, which make nano-calorimetry an attractive technology for high throughput multiplexed low cost point of care diagnostics.

Introduction

Therapeutic monoclonal antibodies (mAbs) are of particular interest as an emerging alternative to small-molecule drugs for the treatment of conditions such as cancer, infections, cardiovascular disease, and immune disorders[1,2]. The first mAb approved for solid tumor cancer

---

[2] Submitted for publication to *Proceedings of the National Academy of Sciences of the United States of America*.

treatment, trastuzumab (Herceptin®, Genentech USA), is a humanized IgG1κ useful against HER2 positive breast cancers[3]. However, in some patients, cellular Fc receptors responsible for binding to and recycling trastuzumab are atypical; and as such, trastuzumab is cleared quicker from the body resulting in reduced therapeutic efficacy[4]. In order to improve patient outcome and - in view of trastuzumab's high cost (>$50,000 per treatment course) - serum titer measurements can be used to determine patient trastuzumab clearance rates and appropriate dosages for efficient treatment. Enzyme linked immunosorbent assays (ELISAs) have become the gold standard for measuring antibodies and antigens, both native and introduced, in biological samples[5] since the 1970s. Of the many commercially available microtiter-based ELISA kits, most utilize an enzyme linked to a detecting antibody to produce a colorimetric, chemiluminescent, or fluorescent signal that can be quantified using a microtiter plate reader. In order to provide a quantitative measurement of an analyte in a sample (e.g. trastuzumab in a human serum sample), standard analyte concentration curves must be generated during sample analysis for accurate quantification of analyte concentrations in samples. Additionally, personnel time and the antibodies needed to carry out ELISAs can be costly. This, in combination with sample consumption and the long time needed to perform ELISAs precipitates the need for a rapid, low-volume, calibration-free ELISA system.

A typical substrate in ELISA is hydrogen peroxide, which is catalytically reduced by horseradish peroxidase (EC 1.11.1.7). The reduced hydrogen peroxide then oxidizes an active reporter molecule or color developer to produce an optical signal that can be detected with a microtiter plate reader. The reaction enthalpy associated with the decomposition of H_2O_2 is large (-98 kJ/mol) making it an attractive target for calorimetric determination. Mattiasson was the first to create an ELISA system with a calorimetric readout, termed Thermometric Enzyme

Linked Immunosorbent Assay (TELISA)[6]. The original TELISA system was based on inhibition binding of a catalase linked albumin to an antibody coated calorimetry column. These flow through systems required a large sample volume (>0.5 ml) and required the use of temperature controlled thermistor columns, but sensitivity to the µg/ml level for insulin, human IgG, and album were achieved[7]. However, in the years following, fluorescent and chemiluminescent ELISA systems achieved much higher sensitivity, so TELISA has seen little use in the past decade.

Results & Discussion

Thermometric ELISA

We report here a sandwich based TELISA system that utilizes nanoliters of sample and does not require calibration curves like inhibition assays. **Figure 13** shows the antibody binding

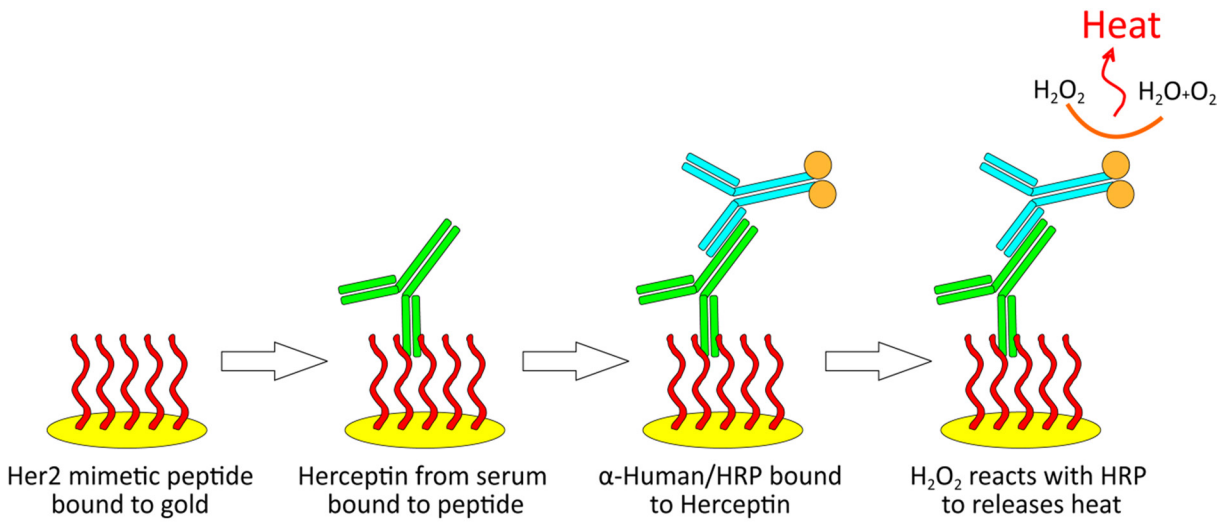

Figure 13. Thermometric ELISA steps. The binding steps of the TELISA follow that of a traditional sandwich ELISA. However, in the detection step, the heat from the reaction of H_2O_2 and OPD with HRP is quantified, rather than a chromogenic or fluorescent measurement. All steps can be carried out in a 1-nanoliter volume, greatly reducing reagent and sample consumption.

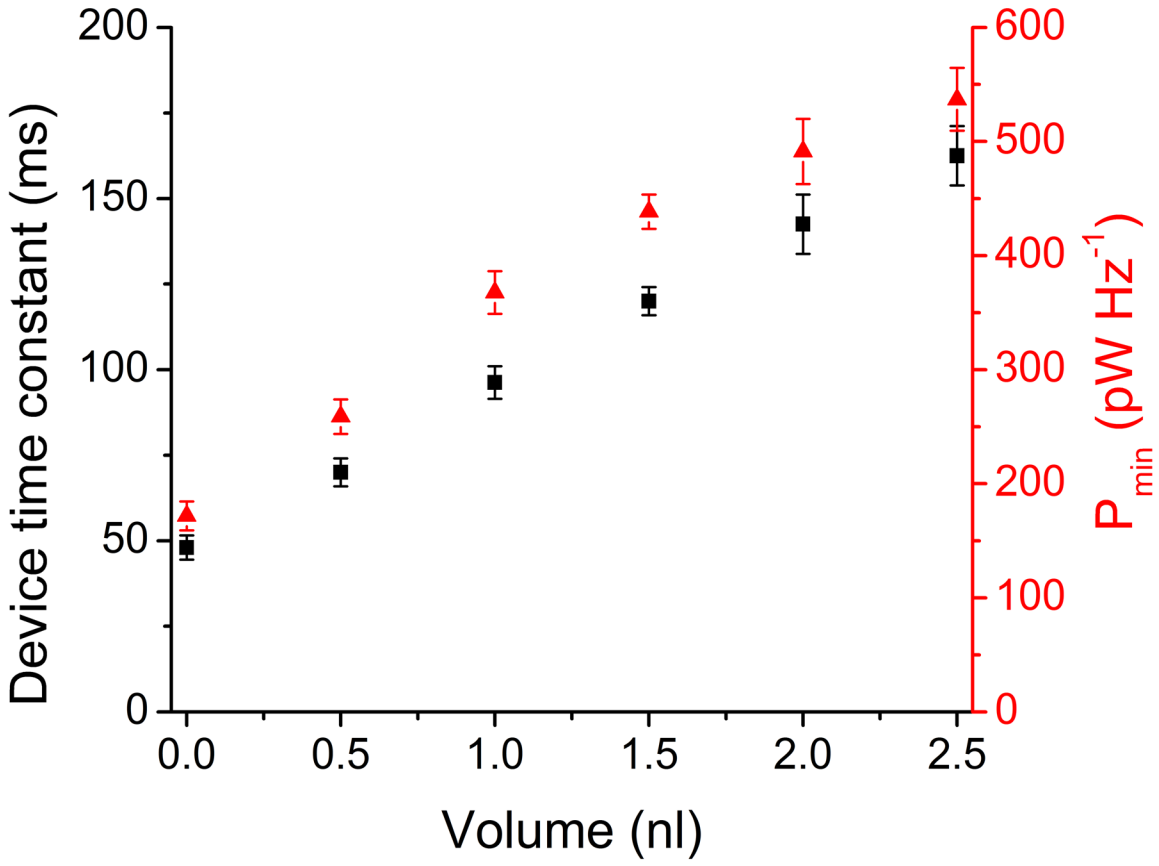

Figure 14. Small volume performance. The nanocalorimeter devices exhibit optimal performance at small sample volumes. 1 nl was chosen as the optimal volume to balance performance and droplet evaporation. The combination of sub-100 ms time constant (□) and minimum detectable power (P_{min}) (Δ) of 375 pW/Hz$^{1/2}$ at 1 nl, allows for high resolution measurement of TELISA heat signatures. Means ± s.d. are shown (n = 5 per point).

steps and the thermal readout step with HRP. Since a known amount of energy is released when a finite substrate supply is consumed, the reaction is self-calibrating. Furthermore, the sample volume can be reduced to maximize the surface area to volume ratio to increase assay sensitivity (**Figure 14**). By operating in a 1nl reaction volume, antibody and sample consumption is also greatly diminished. This has the added benefit of minimizing antibody binding time by reducing diffusion distance, such that a multi-step sandwich ELISA can be performed in less than 5 minutes[8]. This allows for the potential of pinprick point of care measurements that incorporate

on-chip microfluidics to automate sample handling. Since many commercial ELISA systems already rely on a peroxidase/peroxide reporter system, many off-the-shelf kits can be converted to use in TELISA. Significant advantages of the TELISA over traditional ELISAs are a reduction in assay times, conservation of sample volume, and calibration free measurements.

Device Design

Since the energies involved in the enzymatic reactions of ELISA can be quite small (< 100 nJ) and over a long time period (>100 s), a highly sensitive calorimeter with minimal drift and capable of sub-nanowatt resolution is needed. Previous calorimeters based on off-the-shelf thin film IR sensors showed a minimum energy resolution of 1.5 nW/Hz$^{1/2}$ and suffered from

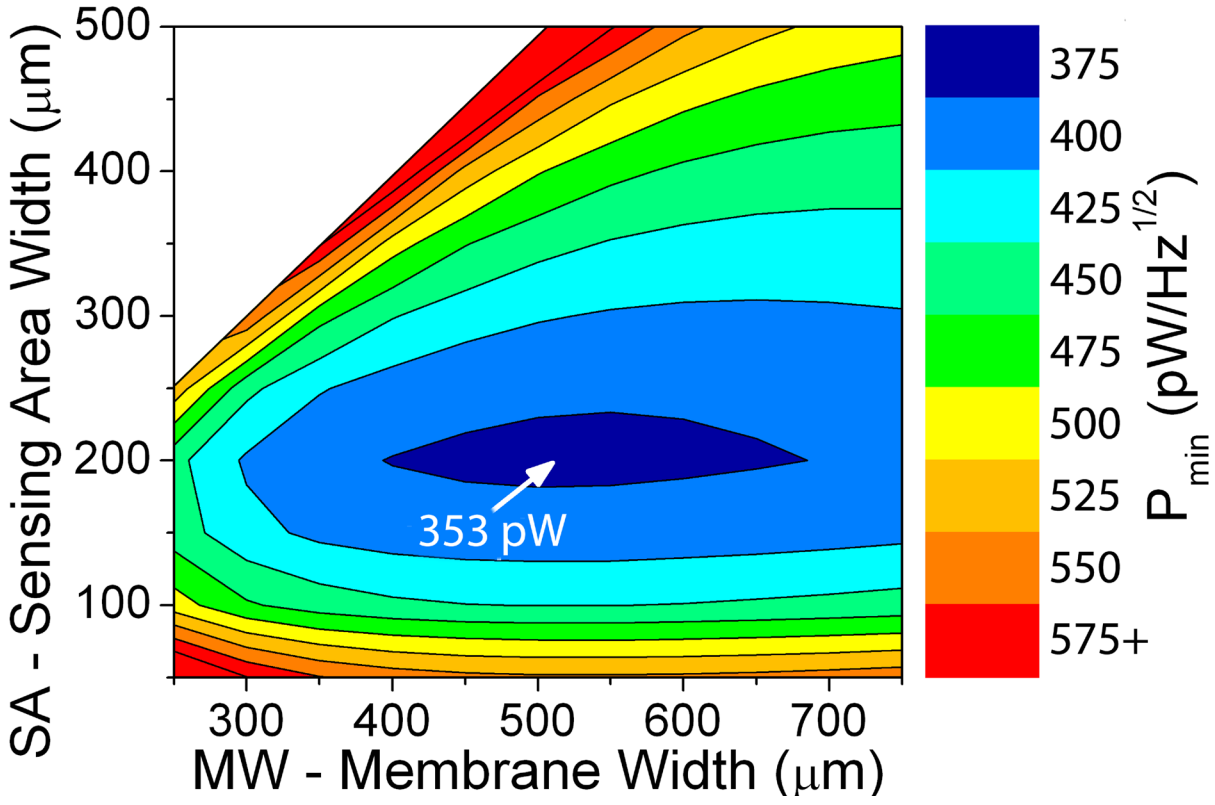

Figure 15. Calorimeter optimization. Heat flow and electrical modeling in COMSOL and MATLAB were used to determine the optimal dimensions of the calorimeter during the design phase. By balancing thermopile track length, thickness, and membrane size a P_{min} of 353 pW/Hz$^{1/2}$ was predicted. Actual measurements on the constructed calorimeters showed a P_{min} of 375 pW/Hz$^{1/2}$.

evaporative droplet loss[9]. Therefore, new calorimeters were designed to incorporate high Seebeck coefficient materials in the thermopile, a low conductivity membrane, better vapor sealing, and optimized dimensions (**Appendix D**). Heat flow modeling of the calorimeter was carried out using COMSOL Multiphysics to find the optimal membrane size, thickness, and junction number (**Figure 15**). Electrical modeling and thin film Seebeck coefficient measurements were also incorporated to investigate different thermopile materials, with Ti and Bi having the best mix of low resistance and high relative Seebeck coefficient. Modeling showed the optimal configuration to be a 28-junction Bi/Ti thermopile with a 525 μm wide Su-8 polymer membrane and a 200 μm wide hot-junction sensing area. The core technology of TELISA system is a microfabricated polymer membrane nano-calorimeter (**Figure 16**). Standard integrated circuit microfabrication techniques were used to construct the thin film calorimeters on Si substrates with a high device yield of >85%. Devices showed no degradation in performance over time (6 months), provided the membrane was not ruptured. With a 1 nl sample volume, acid-base and laser calibration[9] of the calorimeters showed a minimum detectable power of 375 $pW/Hz^{1/2}$, a power sensitivity of 45 V/W, and a time constant of 95 ms (**Figure 14**), all in line with the model predictions. This allows for the detection of as little as 4 femtomoles of hydrogen peroxide, or the energy output of 6 attomoles of typical HRP.

Trastuzumab Binding

The most abundant class/subclass of antibody present in human serum is IgG1 and normally ranges in concentration from 9-12 mg/ml of serum[10]. Trastuzumab is a genetically engineered humanized IgG1 kappa light chain mAb, however since it incorporates human IgG_1 constant domains it is difficult to distinguish from normal human antibodies[11]. To overcome this, Jiang et. al. used phage display to select for the HER2 peptide mimotope (designated Ch-19,

sequence: CGSGSGSQLGPYELWELSH) that trastuzumab binds[12]. Ch-19 has been successfully immobilized onto a gold sensor surface for use in a piezoimmunosensor (i.e. quartz crystal microbalance) assay to capture and detect trastuzumab present in solution[13]. In our study, we used Ch-19M (BioVentures, Murfreesboro, TN), a modified version that includes a biotin linker and an improved sequence to minimize serum matrix effects. We detected trastuzumab in 1 nl of diluted human serum using a typical sandwich ELISA format with Ch-19M and incorporated a

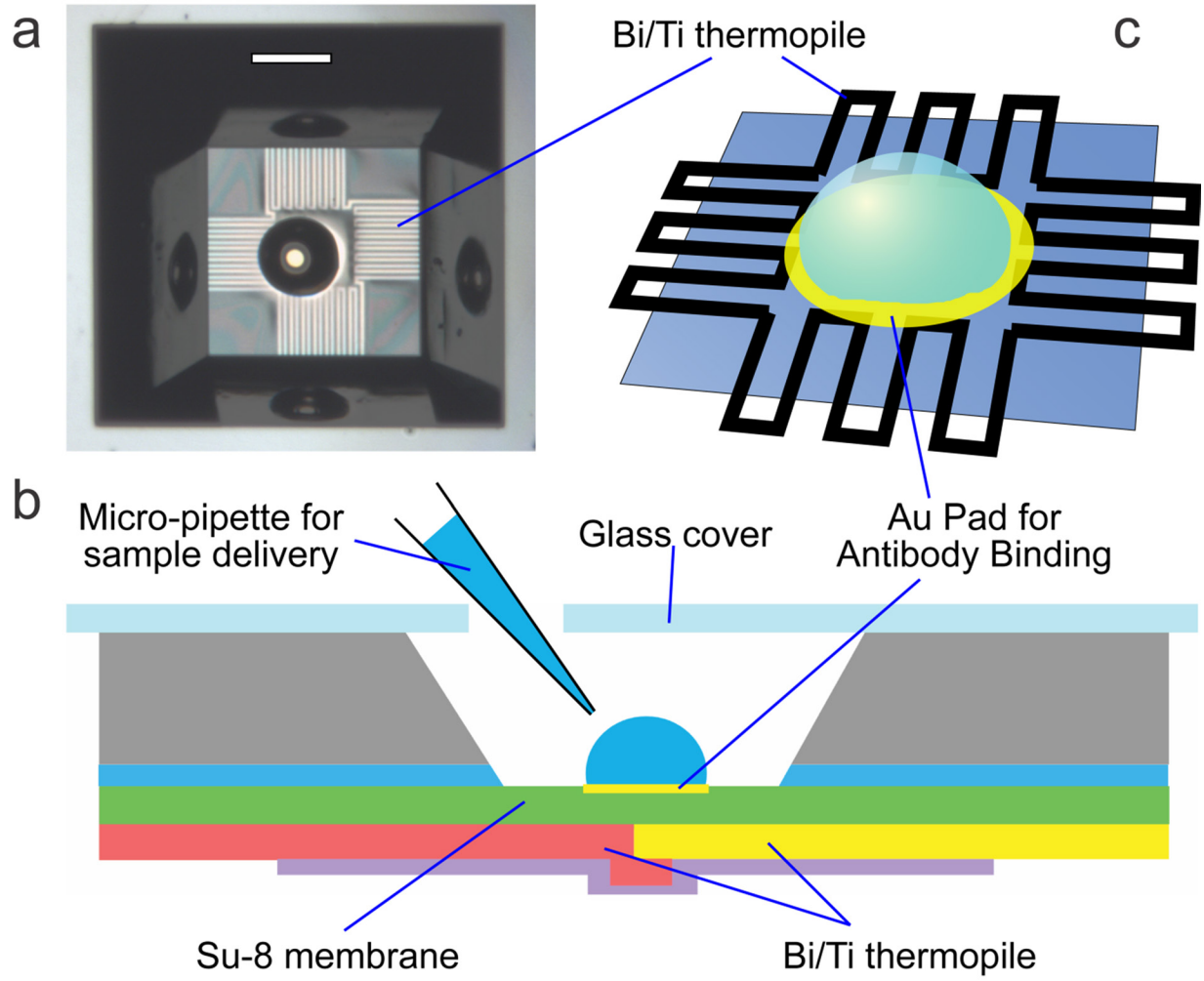

Figure 16. Nanocalorimeter device layout. (**a,c**) A 1 nl sample drop sits atop a suspended Su-8 membrane on which a 28 Bi/Ti thermopile junction has been patterned. The Su-8 membrane and gold pad are used to immobilize the HER2 peptide mimetic, confine the sample droplet, and carry out the reaction for trastuzumab detection. Scale bar 200 µm. (**b**) The sample drop sits in an anisotropically etched Si pit and is accessed through a hole in the cover via a glass micropipette.

thermal rather than an optical readout (**Figure 13**). A thermally deposited gold spot on the topside of the calorimeter membrane allowed for attachment of the Ch-19M peptide andsubsequent trastuzumab binding (**Figure 16**). All binding steps of a normal ELISA were carried out on the calorimeter surface in 1 nl reaction volumes. Trastuzumab detection was performed via calorimetric measurement of the heat of reaction of peroxide with the peroxidase linked secondary antibodies and required <100 s of measurement time. The limit of detection for the nanoliter based TELISA was 10 μg/ml trastuzumab in human serum. Normal human serum contains a high concentration (~9-12 mg/ml serum) of IgG1 antibodies. However, normal human serum IgG1 and the negative control humanized therapeutic antibody bevacizumab (Avastin®, Genentech USA) (an IgG1 kappa light chain mAb) did not bind to Ch-19M in the TELISA (**Figure 17**). Additionally, trastuzumab in diluted human serum did not bind to the negative control PINC peptide (PINCTHSCVDLDDKGCPAEQRASPLTSIISK-Ahx-biotin, United Biosystems) when used *in lieu* of Ch-19M (**Figure 17**). The PINC peptide is another HER2 mimotope, however is not known to bind to trastuzumab. These results suggest that trastuzumab could be specifically detected in 1 nl of diluted human serum, and that the assay exhibited high sensitivity.

Reduction in sample volume

In the trastuzumab TELISA, it was determined that trastuzumab concentration and the peroxide reaction time constant (τ) correlated well (R^2=0.954) and that τ could be used to accurately determine trastuzumab concentration in serum (**Figure 17**). It was found that τ could be varied by changing H_2O_2 concentration, with a shorter τ being obtained at lower concentrations. However, this resulted in a reduced assay signal and an increase in assay

background noise. It was determined that a 10 mM concentration of H_2O_2 provided a balance between assay time and signal strength for use in the present application.

Serum Matrix Effects

Components (e.g. proteins, lipids, etc.) present in human serum can interfere with antigen (e.g. Ch-19M) and antibody (e.g. trastuzumab) interactions. These interferences are referred to as serum matrix effects and lead to nonspecific binding. Trastuzumab diluted in serum could not be

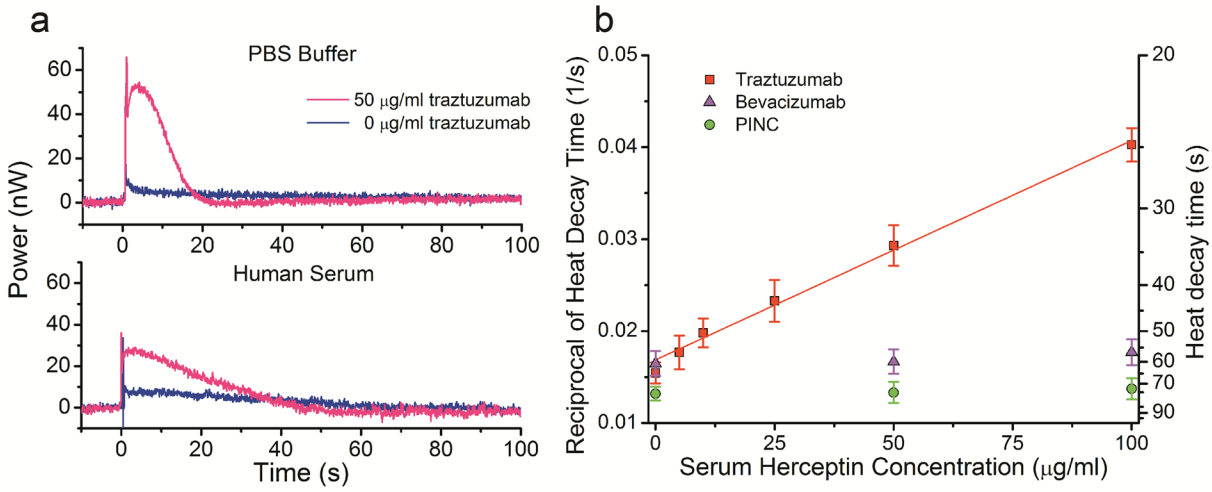

Figure 17. Thermometric ELISA signal and dose response. (**a**) A strong signal is produced during the detection of 50 μg/ml trastuzumab in PBS. Trastuzumab suspended in human serum shows a lower binding efficiency and a slightly higher background signal - presumably due to serum matrix effects. (**b**) As trastuzumab concentration increases, peroxide is consumed faster; leading to a shorter heat decay time. Negative controls with bevacizumab and PINC show no sensitivity to trastuzumab. The therapeutic dosage of trastuzumab (10-100 μg/ml serum concentration) is well covered by TELISA quantification and is highly correlated to τ (R^2=0.954). Means ± s.d. are shown (n = 4 per point).

detected when assayed against Ch-19 using a piezoimmunosensor assay[13], but could be detected when diluted in PBS. The results of the piezoimmunosensor assay suggested that serum matrix effects interfered with the trastuzumab/Ch-19 interactions. However, the concentration of reagents (e.g. the detergent Tween 20), sensor composition (e.g. a 1nl Su-8 sensor containing a gold spot versus a 1 ml cuvette containing a gold quartz crystal microbalance), diffusion

distances (e.g. <200 μm versus ~10 mm), and incubation times (e.g. <30 min versus 1-12 hr) were different for the TELISA versus the piezoimmunosensor assay, respectively. Additionally, the use of a biotin linker and the altered amino acid sequence on Ch-19M may have allowed it to bind more efficiently to trastuzumab and avoid serum matrix effects. Some serum matrix effects were seen with the TELISA, as trastuzumab binding was reduced when diluted in human serum rather than PBS buffer (**Figure 17**). This was taken into account during calibration and was not severe enough to affect our findings. Although differences in the assay conditions exist, it will be important to carry out future studies to identify those differences that may be responsible for abrogating serum matrix effects as serum matrix effects can typically render crucial diagnostic immunoassays useless.

Conclusions

TELISA does not rely on specific reagents and can be widely adapted to a broad spectrum of immunoassays using existing reagents. The thermal signature is quantified using micromachined nano-calorimeters with nanoliter sized reaction volumes, sub-nanojoule sensitives, and sub-second time constants. The technology lends itself to a point of care device for high throughput multiplexed assay based on a finger prick. We are currently working on label free point of care systems based on the thermal detection of direct binding events and analyte reactions.

Acknowledgements

This work was supported by a grant from BioVentures, Murfreesboro, TN.

Supplementary Material for Chapter III

Device modeling

Since the energies involved in the enzymatic reactions of ELISA can be quite small (< 100 nJ) and over a long time period (>100 s), a highly sensitive low drift calorimeter capable of sub-nanowatt resolution is needed. Other micro-calorimeter designs utilize a Si based membrane or microfluidic flow channels that increase heat flow and limit the minimum power sensitivity to several nanowatts[14-16]. In order to maximize sensitivity, a calorimeter with a small working volume, low thermal conductivity membrane, and high temperature sensing resolution is needed. We began by investigating the optimal thermopile materials. Prior research-grade micro-calorimeters have utilized materials like gold and nickel that are easy to micromachine and have low resistance, but lack the high Seebeck coefficient needed for high sensitivity[15,17]. Since the resistance and thermoelectric properties of thin film metals can vary greatly from the bulk properties[18], we performed 4 point sheet resistance and thermoelectric measurement of various metals to find those most suitable for our calorimeter. Bismuth and titanium provided the best mix of conductivity and high absolute Seebeck coefficient. The ideal calorimeter would have a very wide membrane on which the reaction droplet and thermopile sit to minimize thermal conduction away from the droplet. However, this creates long thermopile track with high electrical resistance. This leads to an increase in Johnson resistor noise, the limiting factor in minimum detectable power. A COMSOL Multiphysics/ MATLAB model was built based on previous calorimeter designs[9]. Variables were introduced to change the sensing area and membrane size while maximizing sensitivity and minimizing thermopile resistance. An iterative approach produced the data in **Figure 15** and showed for a 1 nl drop, the optimal calorimeter had a membrane width of 525 μm and a sensing area width of 200 μm with 28 junctions. 1 nl was

chosen as the optimal drop size as previous work had shown that as drop volume decreases, sensitivity increases, but must be balanced with sample evaporation to allow sufficient measurement time[9]. Variables for thermopile thickness were also introduced and it was found that a Ti thickness of 200 nm and a Bi thickness of 400 nm provided the best balance of thermal and electrical conductivity.

Device Fabrication

All micromachining was performed in the VIIBRE and VINSE cleanrooms at Vanderbilt University. 75 mm diameter silicon wafers, <100> orientation, double side polished, with 500 μm low stress silicon nitride (SiN) coated on both sides were obtained from WRS Materials (San Jose, CA). Chrome on soda-lime photomasks were produced by Advance Reproductions Corp. (North Andover, MA). Photoresist and developer were procured from MicroChem Corp. (Westborough, MA). All other chemical were from Fisher Scientific (Pittsburgh, PA). The numbering of the following steps corresponds to those displayed in **Figure 18**.

1. SiN hardmask patterning. Dry etching of SiN is the most efficient and allows for patterning using Shipley's S1813. Briefly, S1813 was spun on at 3000 rpm, soft baked at 95 °C for 2 min, G-line UV exposed through the chrome mask at 175 mJ/cm^2, developed in MF-330 for 1 min, rinsed in 18 megohm water, and dried with N_2. Dry etching was performed in an Orion RIE system (Trion Technology, Clearwater, FL) at 100 W, 60 mTorr, 25 sccm CF_4, and 5 sccm O_2 for 270 s.
2. Si etching. The exposed Si was anisotropically etched in 30% w/w at 80 °C for ~5 hours until the wafers were etched through. Wafers were carefully rinsed in 18-megohm water to prevent damage to the thin SiN windows.
3. Su-8 membrane creation. After a 5 min dehydration bake at 200 °C, Su-8 2002 was spun on

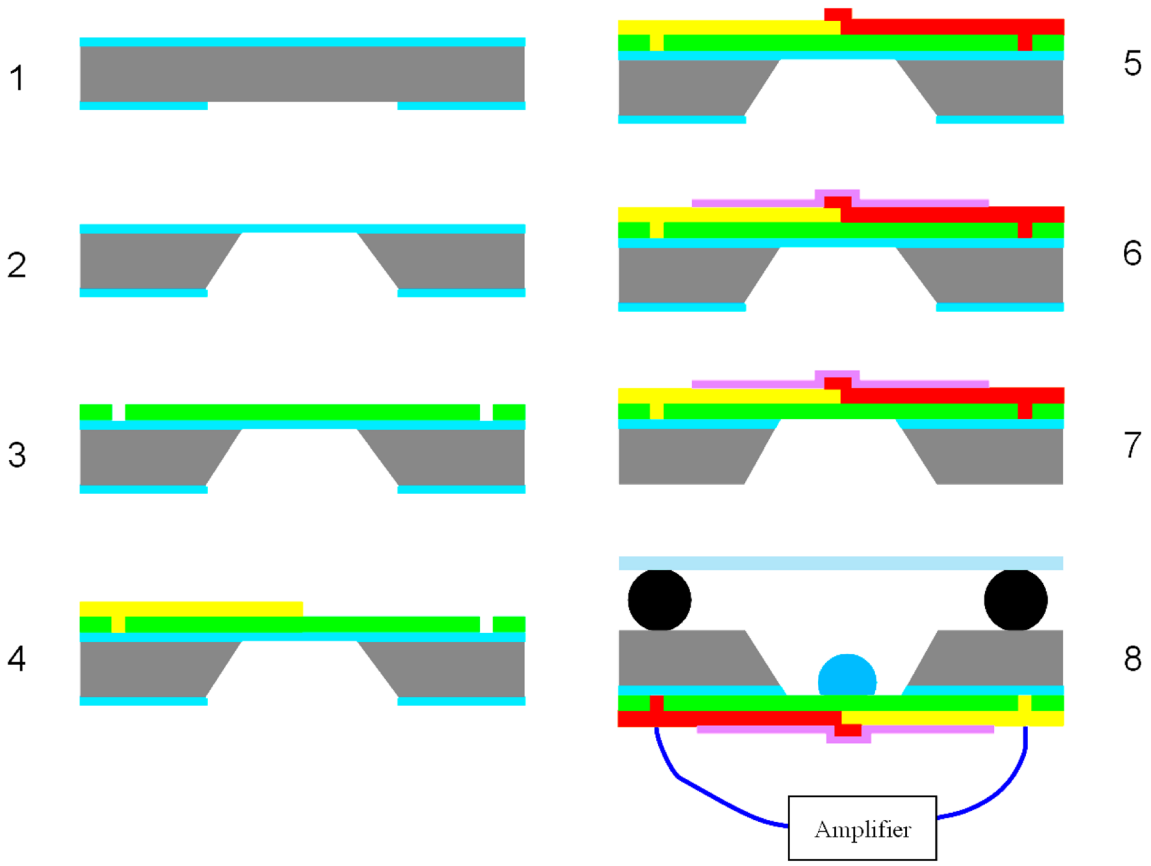

Figure 18. Calorimeter microfabrication steps. (**1-2**) Anisotropically etched pit is formed in the silicon substrate, revealing a sacrificial silicon nitride membrane. (**3**) Su-8 polymer membrane is applied. (**4-5**) Bismuth and titanium thermopile tracks are deposited and patterned. (**6**) Silicon dioxide passivation layer is applied. (**7**) The remaining silicon nitrite under the membrane is removed and the gold binding spot applied. (**8**) The finished device is paired with a glass lid and o-ring to prevent sample evaporation and attached to a low noise amplifier during measurements.

at 3000 rpm, soft baked at 95 °C for 2 min, exposed at 225 mJ/cm^2, post exposure baked at 95 °C for 2 min, developed in Su-8 developer, rinsed with 18 megohm water, and finally hard baked at 200 °C for 5 min.

4. Ti patterning. Deposition was performed in an Innotech e$^-$ beam deposition/ion-mill system. Immediately before each metal deposition step, wafers were ion mill cleaned for 30 s at 25 mA to remove any residual films or oxides. 99.99% Ti from Kurt J. Lesker Co. (Jefferson Hills, PA) was applied at a rate of 5 A/s to a thickness of 200 nm at a pressure of <1 x 10^{-3}

Pa. Ti was then patterned with S1813 as above with the addition of a reflow step at 150 °C after development to prevent photoresist undercutting during etching. Ti was etched in 20 H_2O:1HF:1H_2O_2 and photoresist was stripped with acetone.

5. Bi patterning. Bi was deposited at 10 A/s to a thickness of 400 nm. Bi was patterned with S1813 as above and ion mill etched at 50 mA for ~3 min. After photoresist stripping with acetone, a 5 min O_2 descum was perform on the Orion RIE system
6. Passivation. A 100 nm silicon dioxide passivation layer was applied to prevent oxidation and damage to the thermopile. The contact pads were masked off during deposition.
7. Membrane finishing. The remaining SiN under the membrane is removed using the Orion RIE system. 100 nm thick, 200 μm wide gold spots for antibody binding were thermally deposited on the underside of the membrane.
8. Packaging. The wafer was then diced and rubber o-rings glued onto the surface to create a larger sample chamber. A glass cover slide with a sonically drilled 500 μm access hole was placed on top and sealed with mineral oil. Electrical contacts to the thermopile were made using pogo pins and a custom designed holder.

Thermometric ELISA

Nano-calorimeter devices were prepared for use by rinsing the sample well with toluene to remove any manufacturing residue or protein left from previous tests. Streptavidin was passively adsorbed to the Au surface by incubating streptavidin diluted in PBS (20 μg/ml) on the Au surface for 30 min at room temperature in a humidified petri dish[19]. The sensor surface was rinsed and blocked for 15 s with PBS containing 0.2% Tween 20 (PBS-T). The biotinylated HER2 peptide mimetic Ch-19M was diluted to 3 μM in PBS-T and coupled to the adsorbed streptavidin by incubating for 20 min at room temperature. The sensor was again rinsed with

PBS-T. Pooled human serum (H4522, Sigma Aldrich) with varying concentrations of trastuzumab (0-100 μg/ml) was diluted 1:4 in PBS-T and allowed to bind for 20 min to Ch-19M on the gold sensor surface. After a PBS-T wash, a peroxidase conjugated, goat anti-human IgG (Fc-specific) antibody (Sigma Aldrich #A0170, diluted 1:250 in PBS-T) was applied to the sensor surface for 20 min at room temperature to bind the available trastuzumab. Unbound peroxidase conjugated anti-human IgG antibody was rinsed from the surface with PBS-T and the sensor surface dried with N_2. The reaction chamber was sealed with a glass cover slide and mineral oil to provide a vapor tight seal that allowed the reaction droplet to persist for up to an hour, although most reactions were completed in less than 5 minutes. 1 nl of PBS was dispensed onto the center of the sensor via an air driven Picospritzer II (Parker Hannifin, Cleveland, OH) using a glass micropipette positioned by a micromanipulator (MP-285, Sutter Instrument Co, Novato, CA) (**Figure 16**). After thermal equilibrium was reached, 100 pl of hydrogen peroxide (50 mM - acting as an electron acceptor) and o-phenylenediamine dihydrochloride (OPD) (100 mM - acting as an electron donor) in PBS was injected into the drop to generate a thermal signal. The resulting thermal output from the reaction of H_2O_2 with the bound peroxidase was recorded in LabView until temperature equilibrium was achieved and the time constant was then calculated in MATLAB (**Figure 19**). The baseline shift after injection was due to changes in the evaporation rate of the drop and could be removed by fitting the line to an exponential equation. The heat integral and time constant (τ) of the temperature decay were then computed from the corrected time trace (**Figure 19**). Since the energy released was constant with regards to H_2O_2 concentration, the time needed to consume the substrate was predicted to be dependent upon the concentration and enzyme-kinetics of the peroxidase indirectly coupled to trastuzumab captured

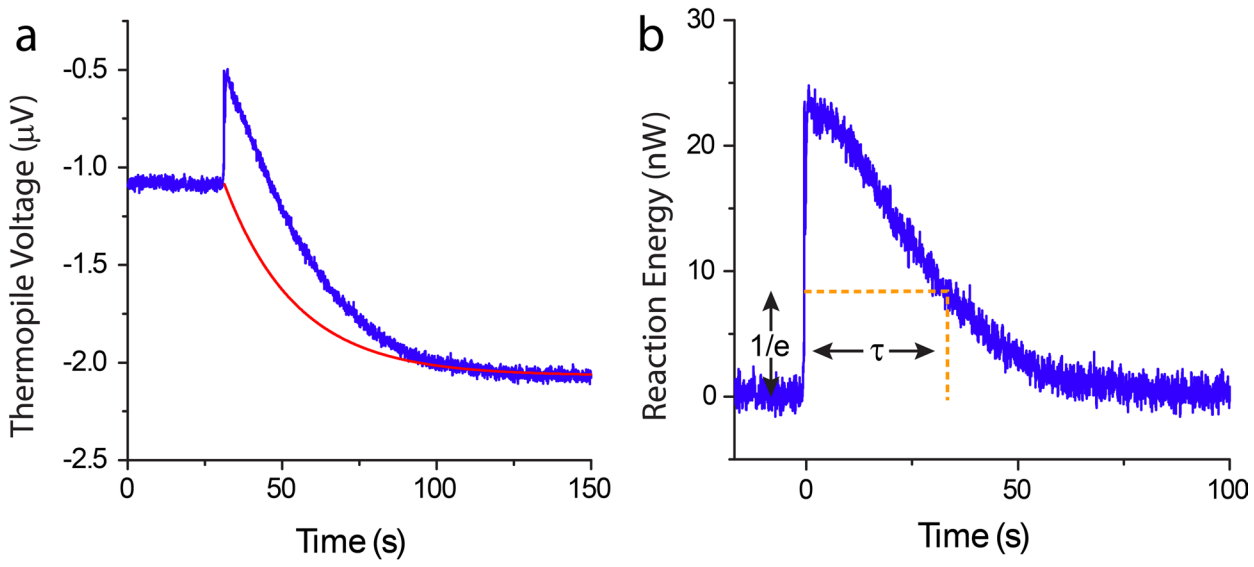

Figure 19. Baseline correction and τ calculation. (**a**) Uncorrected thermopile output voltage from Thermal ELISA detection of 50 μg/ml trastuzumab in human serum. The negative offset after peroxide injection is due to changes in the evaporation rate of the sample droplet. An exponential (red line) is fit to the curve so that the offset can be removed. (**b**) After the offset is removed, voltage can be converted to heat energy based on calorimeter sensitivity (45 V/W). The 1/e decay time (τ) of the signal is used to determine trastuzumab concentration.

on the calorimeter sensor surface. A calibration curve was constructed to allow the calculation of trastuzumab concentration based on the thermal time constant and it was found to have a high correlation (R^2=0.954) (**Figure 17**). A negative control was carried out using another HER2 mimotope peptide (PINC) in place of Ch-19M and showed no significant sensitivity to trastuzumab concentration (**Figure 17**). Similarly, negative controls using Avastin (i.e. Bevacizumab: a humanized IgG1 kappa light chain mAb specific for vascular endothelial growth factor) *in lieu* of trastuzumab did not show binding to Ch-19M (**Figure 17**).

References

1. Piggee, C. Lims and the Art of Ms Proteomics. *Anal. Chem.* **80**, 4801-4806 (2008).
2. Dolgova, E. V. et al. Identification of Cancer Stem Cells and a Strategy for Their Elimination. *Cancer biology & therapy* **15** (2014).
3. Esteva, F. J. et al. Phase Ii Study of Weekly Docetaxel and Trastuzumab for Patients with Her-2–Overexpressing Metastatic Breast Cancer. *J. Clin. Oncol.* **20**, 1800-1808 (2002).
4. Pohlmann, P. R., Mayer, I. A. & Mernaugh, R. Resistance to Trastuzumab in Breast Cancer. *Clin. Cancer. Res.* **15**, 7479-7491 (2009).
5. Premjeet, S. et al. Enzyme-Linked Immuno-Sorbent Assay (Elisa), Basics and It's Application : A Comprehensive Review. *J. Pharm. Res.* **4**, 4581-4583 (2011).
6. Mattiasson, B. et al. Thermometric Enzyme Linked Immunosorbent Assay: Telisa. *Biochim. Biophys. Acta* **483**, 221-227 (1977).
7. Lammers, F. & Scheper, T. Thermal Biosensors in Biotechnology. *Adv. Biochem. Eng. Biotechnol.* **64**, 35-67 (1999).
8. Kudo, Y. et al. Rapid Elisa in Droplet on Pdms Dimple with Nanoliter Reagents Dispensed by Ink-Jet Microchip. *Chem. Lett.* **37**, 536-537 (2008).
9. Lubbers, B. & Baudenbacher, F. Isothermal Titration Calorimetry in Nanoliter Droplets with Subsecond Time Constants. *Anal. Chem.* **83**, 7955-7961 (2011).
10. Delves, P. J. & Roitt, I. M., *Roitt's Essential Immunology*, 12th ed. (Wiley-Blackwell, Chichester, West Sussex ; Hoboken, NJ, 2011).
11. Morell, A. et al. Human Igg Subclasses in Maternal and Fetal Serum. *Vox Sang.* **21**, 481-492 (1971).
12. Jiang, B. et al. A Novel Peptide Isolated from a Phage Display Peptide Library with Trastuzumab Can Mimic Antigen Epitope of Her-2. *J. Biol. Chem.* **280**, 4656-4662 (2005).
13. Shang, Y., Mernaugh, R. & Zeng, X. Characterization of the Native and Denatured Herceptin by Enzyme Linked Immunosorbent Assay and Quartz Crystal Microbalance Using a High-Affinity Single Chain Fragment Variable Recombinant Antibody. *Anal. Chem.* **84**, 8164-8170 (2012).
14. Carreto-Vazquez, V. H. et al. Chip-Scale Calorimeters: Potential Uses in Chemical Engineering. *J. Loss Prev. Process Indust.* **24**, 34-42 (2011).
15. Johannessen, E. A. et al. A Suspended Membrane Nanocalorimeter for Ultralow Volume Bioanalysis. *IEEE Trans Nanobioscience* **1**, 29-36 (2002).
16. Verhaegen, K. et al. A High-Throughput Silicon Microphysiometer. *Sensor Actuat a-Phys* **82**, 186-190 (2000).
17. Lee, W. et al. High-Sensitivity Microfluidic Calorimeters for Biological and Chemical Applications. *Proc. Natl. Acad. Sci. U. S. A.* **106**, 15225-15230 (2009).
18. Boyer, A. & Cisse, E. Properties of Thin-Film Thermoelectric-Materials - Application to Sensors Using the Seebeck Effect. *Materials Science and Engineering B-Solid State Materials for Advanced Technology* **13**, 103-111 (1992).
19. Ebersole, R. C. et al. Spontaneously Formed Functionally Active Avidin Monolayers on Metal-Surfaces - a Strategy for Immobilizing Biological Reagents and Design of Piezoelectric Biosensors. *J. Am. Chem. Soc.* **112**, 3239-3241 (1990).

CHAPTER IV

Nano-Calorimetry Based Point Of Care Biosensor For Metabolic Disease Management[3]

By

Brad Lubbers, Raymond Mernaugh, Elliott Dawson, & Franz Baudenbacher

Abstract

Inborn errors of metabolism are characterized by dysfunction of key enzymes or transporters that result in substrate accumulation and product deficit. One such disease, Phenylketonuria (PKU), leads to the build-up phenylalanine (Phe), which, if not treated through diet modification, co-factor administration, or enzyme replacement therapy; results in mental retardation. Management of PKU requires frequent monitoring of Phe blood levels, however no point of care (POC) Phe devices exist. We present a novel point of care biosensor to measure Phe levels utilizing a microfabricated differential nanocalorimeter. The calorimeter has a resolution of 1.4±0.2 $nJ/Hz^{1/2}$ utilizing a 27 junction bismuth/titanium thermopile, with a total Seebeck coefficient of 2160 μV/K. Samples are wicked to the calorimeter through a capillary channel making it feasible to monitor blood Phe levels in blood samples obtained through a finger prick (<1 μL sample required). We demonstrate device performance utilizing pegylated phenylalanine ammonia-lyase (PEG-PAL), but are limited by the activity of PEG-PAL to reliable detection limits of <5mM Phe. The POC biosensor concept could be adapted to a large number of metabolic diseases by changing the immobilized enzyme.

---

[3] Submitted for publication to *Biosensors and Bioelectronics*.

Introduction

The expansion of point of care (POC) diagnostics over the past decade provides near instantaneous results for many common blood tests that previously required expensive laboratory equipment and personnel time. With a worldwide market value of over $15.5 billion in 2013, POC diagnostics represents one of the fastest growing medical technology segments[1]. For example, the largest POC segment, blood glucose monitoring, allows patients to conveniently monitor blood glucose levels. Test results are essential for diabetic patients to help them regulate their diet and medications[2]. Phenylketonuria (PKU) is another metabolic disease for which at-home monitoring is needed to help manage diet and medications. PKU affects 1 in 15,000 worldwide, and it prevents the conversion of metabolism of the essential amino acid phenylalanine (Phe) to tyrosine (Tyr). This results in high blood concentrations of Phe that can cause mental retardation if not treated though diet, co-factor, and/or enzyme replacement therapy, as well as Tyr deficiency[3]. While tandem mass spectrometry (MS/MS) testing of blood Phe levels is rapid and accurate it is still limited to larger clinical laboratories[4]. With new enzyme replacement therapies for PKU undergoing human clinical trials, the need for at home Phe monitoring to guide dosing and diet is even greater[5]. To enable POC Phe testing, we have developed a novel calorimetric biosensor with the ability to measure Phe levels in 1 µl of sample.

Biosensors are the basis for most POC diagnostic technologies. An enzymatic reaction with the analyte of interest produces a quantifiable signal that is transduced by one of several different methods, amperometric, optical, calorimetric, or acoustic to name a few[6,7]. Calorimetry is an attractive detection method as most enzymatic reactions produce 20-100 kJ/mole substrate and do not require the use of secondary or labeling reactions for transduction as most optical methods do[8]. However, calorimetry is based on a temperature measurement that senses heat

changes from all chemical or physical processes present at the sensor. This requires the elimination of noise from side reactions and temperature fluctuations[9]. Previously calorimetric biosensors relied on flow-through columns with enzymes immobilized on a support matrix and thermistors for temperature sensing[7]. These required large sample volumes (>0.5 ml), exact temperature control, and complex pumping systems that limited their use to laboratory settings[10]. Many were successful in measuring sub-milimolar concentrations of common blood analytes like cholesterol, urea, lactate, glucose, and ethanol[9,11]. The current trend in calorimetric biosensors is towards miniaturization, microfluidic sample handing, and on-chip thermoelectric based sensing[12]. This reduces sample volumes required to the microliter range and minimum detectable energies approaching 1 nJ are possible[13]. A few calorimetric biosensors suited to POC have been developed to measure blood glucose or urine urea by the large enthalpy changes associated with these reactions (-80 and -61 kJ/mol)[14,15]. In the case of Davaji and Lee, a thin film resistive temperature detector was employed, so temperature sensitivity was limited to 26 mK and the noise limited minimum glucose concentration was 1.51 mM. A paper strip held the glucose oxidase enzyme in close proximity to the sensing surface, however it had to be added to the flow strip at the beginning of each measurement, and evaporative effects caused a large drift in the calorimeter signal. Lai and Tadigadapa's device relied on a Y-cut quartz resonator for temperature sensing, giving higher temperature sensitivity. Despite placing the entire device in a 37 ˚C oven during measurements, and using microfluidic pumping systems, the uncertainty in their urea detection results were still unreliable. This suggests that creation of a user-friendly POC device will require automated liquid handing that is insensitive to user error.

Another impediment to POC biosensors is enzyme immobilization and preservation. While the gold-thiol binding system is an attractive method to form patternable enzyme

monolayers on a calorimeter surface, limiting enzyme immobilization to one dimension, results in a low binding density (10's picomoles of enzyme per cm^2) compared to a nano-porous medium like silica gel (sol-gel). The extremely high surface area of sol-gels (100-1000 m^2/g) and the stabilizing effects of physical confinement of enzyme molecules make sol-gels attractive, but it is difficult to create a patternable surface coating on the micrometer level. Most commercial glucose biosensors use passive absorption of glucose oxidase onto a nitrocellulose carrier or physical entrapment of the enzyme between two size exclusion membranes[2,16]. This allows a high density of enzyme to be immobilized, often with a preserving reagent like trehalose or polyvinyl alcohol (PVA) included[17]. Another strategy for enzyme preservation involves enzyme modification. The addition of groups like polyethylene glycol (PEG) has been widely used to prevent loss of activity, presumably by crosslinking enzyme structure and/or preventing steric hindrance[18].

We previously used nanoliter volume calorimeters with very low minimum detectable energy (375 $pJ/Hz^{1/2}$) to create a Thermometric ELISA system[19]. The high sensitivity was due to the use of suspended polymer membranes holding bismuth/titanium thermopiles and allowed for μg/ml measurement of the monoclonal cancer drug trastuzumab in human serum. Here we present a device based on that nano-calorimeter design, but with differential sensing to eliminate common mode noise and capillary microfluidic channels for sample delivery to the thermoelectric sensor. Catalase (CAT) and Pegylated phenylalanine ammonia-lyase (PEG-PAL) are used in the detection of their respective substrates. Many common blood analytes (i.e. cholesterol, carbohydrates, amino acids) have corresponding oxidases that release H_2O_2 during the oxidation of their substrate. The large enthalpy associated with H_2O_2 decomposition (-98 kJ/mol), can be exploited by co-immobilizing these enzymes with CAT, leading to enzymatic

amplification of the signal[9]. Most oxidases require O_2 to react and this can be a limiting factor in closed systems since the O_2 saturation of water is only 0.25 mM. Alternative electron acceptors can be used, but must then be immobilized with the enzymes, increasing stability concerns. In the interest of reducing the number of immobilized components, we focused on systems not requiring external cofactors or enzyme cascades. PAL is one such enzyme, which catalyzes the following reaction:

$$\text{L-phenylalanine} \leftrightarrow \text{trans-cinnamic acid} + NH_3 \qquad \Delta H=+24.8\ \text{kJ/mol}^{20}$$

Here we present characterization of the capillary calorimeter and preliminary data showing milimolar detection of Phe utilizing PAL in the interest of creating a POC test that could be used at home test for the management of PKU.

Methods

Materials

All micromachining was performed in the VIIBRE and VINSE cleanrooms at Vanderbilt University. 75 mm diameter silicon wafers, <100> orientation, double side polished, with 500 μm low stress silicon nitride (SiN) coated on both sides were obtained from WRS Materials (San Jose, CA). Chrome on soda-lime photomasks were produced by Front Range Photomask (Palmer Lake, CO). Photoresist and developer were procured from MicroChem Corp. (Westborough, MA). PEG-PAL was donated by BioMarin (San Rafael, CA). Catalase (CAT) (#C100) and all other chemical were obtained from Sigma-Aldrich (St. Louis, MO). All reaction were performed at room temperature (20-23 °C).

Device modeling and fabrication

COMSOL and MATLAB heat flow modeling of the nano-calorimeter were performed as described previously[19] with the addition of diffusion modeling of the reaction substrates. The results from the modeling guided the calorimeter design and predicted a minimum detectable energy of <2 nJ/Hz$^{1/2}$. The layout of the device (**Figure 20**) shows the differential sensing thermopile and the capillary flow channels. The thickness of the capillary channel is 50 μm and this low height ensures fast wicking of the sample while minimizing the thermal conductance through the sample fluid itself.

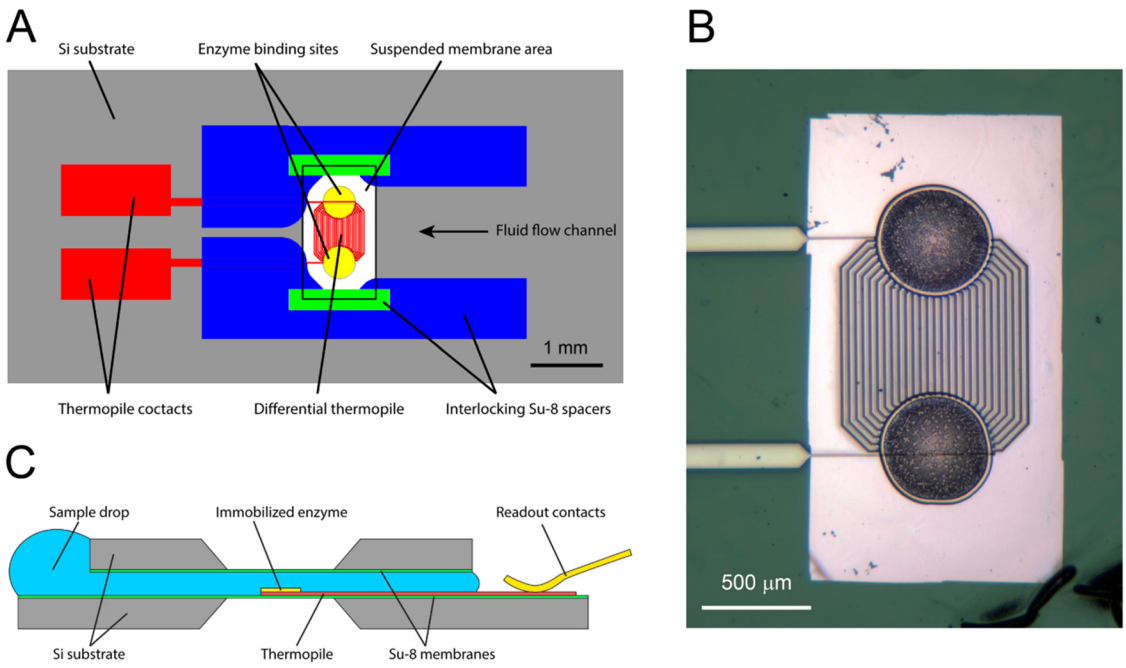

Figure 20. Differential nanocalorimeter layout. (**A**) Active and control enzymes are bound to the two sides of the 27 junction thermopile. The differential sensing arrangement eliminates errors associated with sample evaporation and heat of dilution. Interlocking Su-8 spaces on the top and bottom substrates allow for accurate alignment of the layers. (**B**) Device with CAT immobilized on bottom enzyme spot and BSA control on top. The thermopile junctions are patterned on a suspended Su-8 membrane and line the edges of the enzyme spots to maximize sensitivity. (**C**) The suspended Su-8 membrane over the thermopile allows for very low thermal leakage, thereby maintain high sensitivity. When a sample drop (~1 μl) is placed at the device opening, capillary forces draw the sample into the reaction chamber in less than 1 second.

Fabrication of our device was performed as previously described[19]. An additional 50 μm thick Su-8 layer was patterned on the device surface to create interlocking spacers for the capillary channel (**Figure 20A**). This ensures proper alignment of the top and bottom of the devices. Device yield was good with less than 10% of devices being rejected due to missing traces or broken membranes. Electrical contacts to the thermopile on the chip were built into a spring-loaded holder that also held down the sample lid during measurements. A custom-built low noise amplifier provided signal amplification (gain = 10,000) of the thermopile output voltage and data was recorded in LabVIEW. A 500 μm diameter, 50 nm thick gold spot was deposited through a shadow mask on each side of the thermopile to define a hydrophilic droplet wetting spot amid the hydrophobic Su-8 membrane.

Device characterization

The calorimeter time constant was measured by focusing a light beam onto one side of the differential thermopile and measuring the 1/e time to reach a steady state output voltage while the device was filled with ~1 μl of distilled water (dH_2O). The actual volume of the capillary channel was 225 nl, but excess liquid ensured that the channel filled completely without bubbles and compensated for sample evaporation. Device sensitivity was measured using the enthalpy of dilution of Phe (+8.20 ±0.05 kJ/mol at 298 K)[21]. 5, 10, and 20 nl drops of 100 mM Phe were spotted onto one thermopile junction and allowed to evaporate. The calorimeter lid was reassembled and the device was filled with dH_2O while measuring the thermopile output. Sensitivity was calculated by dividing the integral of the signal by the respective amount of Phe on the sensor. Phe has a negligible enthalpy change due to dilution below 100 mM, precluding the need to calculate integral solution enthalpy. It also dissolves over a period of a few seconds, allowing the device to equilibrate after filling before the Phe has dissolved completely.

Table 3. Device properties. Means ± s.d. are shown (n=6-18 per value).

Parameter	Symbol	Unit	Value
Thermal time constant	τ	ms	315 ± 5
Power sensitivity	P_{sens}	V/W	7.2 ± 0.4
Minimum detectable power	P_{min}	$nJ/(Hz)^{1/2}$	1.4 ± 0.2
Total thermal conductance	G_{tot}	µW/K	300 ± 24
Total Seebeck coefficient	S_{tot}	µV/K	2160
Effective thermal mass	C_{tot}	µJ/K	91.5
Thermopile resistance	R	kohms	11.5 ± 2.1
Capillary volume	v	nl	225

The uncertainty in the sensitivity measurements (**Table 3**) are due to the filling noise obscuring of the first 100-500 ms of the Phe dissolution (**Figure 21B**).

Enzymatic measurements

The activity of CAT (EC 1.11.1.6) was measured by spectrographically monitoring the consumption of H_2O_2 at 240 nm in 50 mM phosphate buffered saline ph 7.4 (PBS). The activity of PEG-PAL (EC 4.3.1.24) was measured by spectrographically monitoring the production of trans-cinnamic acid at 270 nm in 50 mM Tris-HCl pH 8.5 buffer. The reaction of CAT with hydrogen peroxide was used to validate the operation of this calorimetric biosensor. CAT suspended in 50 mM phosphate buffered saline pH 7.4 (PBS) at 1,000 units/ml was spotted onto the gold binding zone on one side of a sensor. PBS with 0.1 mg/ml bovine serum albumin (BSA) was spotted onto the other side of the same sensor. Calibrated glass micropipettes were used to dispense 10 nl of solution to each spot. 1% PVA was added to the CAT/BSA suspension in most cases to aid in confining the enzyme after resuspension in the sample fluid. After assembling the lid onto the sensor and mounting in the device holder, 1 µl aliquots of PBS with H_2O_2 at concentrations between 0-2000 µm were applied to an individual sensor channel. At higher concentrations of H_2O_2, O_2 releases by the reaction formed bubbles and resulted in inconsistent readings. After H_2O_2 application, the output signal was integrated for 30 s, divided

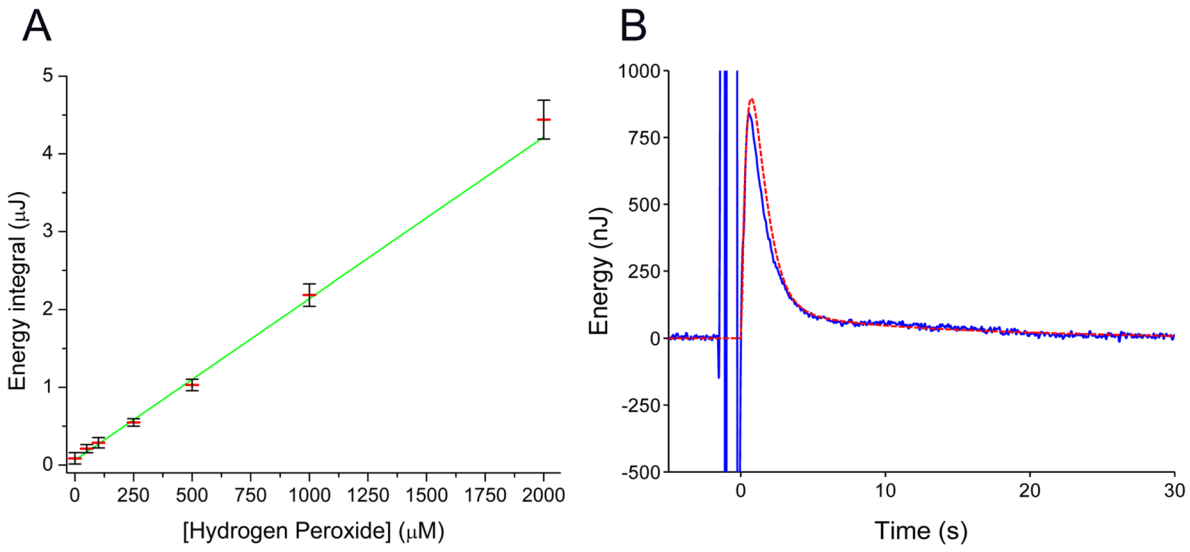

Figure 21. Catalase assay (**A**) Hydrogen peroxide concentration response when reacted with immobilized catalase on the capillary calorimeter. With a linear fit of R^2 = 99.24 and uncertainty of ±75μM, a detection limit of 100 μm H_2O_2 can be achieved. Means ± s.d. are shown (n=4 per point). (**B**) Representative output from 1000 μM H_2O_2 reacting with CAT overlaid with diffusion modeling results in red. The instability of the signal before 0 s is due to the filling of the device and causes uncertainty in the energy integral since it partly obscure the signal. After ~5 s, all local H_2O_2 is consumed and the reaction becomes diffusion limited.

by the device sensitivity of 7.2 V/W, and provided the data for **Figure 21A**. As shown in **Figure 21B**, and confirmed by diffusion modeling, a near steady state signal is maintained once the reaction becomes limited by the diffusion of H_2O_2 to the enzyme site. The energy integral correlates well with H_2O_2 concentration with an uncertainty of ~75 μM below 500 μM. Measurements at 50 μm were significantly different from those at 0 mM (P=0.035).

Phe quantification was accomplished by calorimetric detection with the enzyme PEG-PAL. Unmodified PAL has poor tolerance to desiccation, losing 50% activity upon exposure to moist air after drying[22]. Pegylated PAL (PEG-PAL) was developed to decrease clearance rates needed for treating PKU; however, the PEG group also increases tolerance to desiccation. We performed an activity assay utilizing PEG-PAL desiccated in the presence of 1% PVA and showed 86% activity retained. The low activity of PAL (~ 2 units/mg), required loading a high

concentration onto the sensor surface. PEG-PAL was supplied at 20 mg/ml in 150 mM NaCl, 10 mM tris-HCl pH 7.5. PVA was added to a final concentration of 1% w/v and 10 nl of the enzyme mix spotted onto one enzyme binding spot on the capillary calorimeter. Control enzyme was created by heat inactivation of PEG-PAL at 60 ˚C for 60 minutes before spotting 15 nl onto the control binding site. Assays showed no activity after heat treatment. Phe at 0-10 mM in 50 mM tris-HCl pH 8.3 was introduced into the assembled capillary calorimeter and monitored for up to 1 min. As **Figure 22A** shows, the energy integral for PEG-PAL reacting with Phe at 1 mM was inconsistent at compared to the CAT reactions of 1 mM H_2O_2 (i.e. ± 40% vs 6% error). Measurements at 1 mM were not significantly different from 0 mM readings (P=0.57)(**Figure 22B**), but were at 5 mM and 10 mM (P=0.0039). If more PEG-PAL was loaded onto the sensor surface, variance should decrease due to shorter integration times. A second set of tests were run with PEG-PAL that was spin concentrated using Amicon Ultracel 30K MWCO filters. However, the samples were too viscous to reliably pipette onto the sensor surface and dissolved inconsistently, leading to excessive errors.

Results and Discussion

The differential sensing capillary calorimeter provides a new approach to POC testing of many blood analytes. The detection of H_2O_2 was used as a model system to validate device performance and aided in model alignment to enzyme kinetics and heat flow. Due to the loss of signal during device filling (**Figure 21B**), modeling could aid in reconstructing this data to reduce error and extend our minimum detectable concentration lower. With our current detection limit of 100 μM H_2O_2, this device is not sensitive enough to measure normal H_2O_2 levels in the blood (~2.5 μm). Urine levels are greater (up to 100 μM) and high levels are indicative of

oxidative stress[23]. This device could be a useful tool for urinalysis, and with further improvement could be applicable to blood peroxide analysis.

By integrating the enzyme output over a finite time, rather than measuring a rate as in most blood glucose POC sensors, our device is less sensitive to changes in enzyme activity. When the amount of CAT bound to the sensor was reduced by one-half, the integral only decreased by 6% at the 1000 μM level. Similarly, if an excess of sample (i.e. > 1 μl) is added to the device, more enzyme is lost as it is swept away by the initial flow. Once flow ceases, the remaining enzyme stays localized due to the small diffusion coefficient of CAT compared to H_2O_2 (4.1×10^{-7} vs 1.3×10^{-5} cm^2/s)[24]. Other sources of error are related to the heat of dilution of the enzyme spots. If both spots are not of equal size and well centered on the thermopiles, unintended baseline shifts can occur. The gold spots currently used do not always limit the spread of liquid enzyme droplets before drying and devices with poorly matched spots were rejected. Future research into techniques such as screen printing enzyme pastes are needed to improve production reliability.

Our calorimetric quantification of Phe by reaction with PEG-PAL showes that simple enzymatic reactions could be used to measure common blood analytes without the need for expensive optical or MS/MS systems. The energy integral correlated well with Phe concentration (R^2=0.9295), however noise at low concentrations limit the minimum detectable concentration to around 5 mM (**Figure 22A)**. Though this limit is well above the recommended Phe range for phenylketonuria patients (120-360 μM)[3], a change in enzymes or slight improvements in enzyme activity would enable the device to be used for high level threshold detection. This would allow patients to detect abnormally high Phe levels at home, and report to their doctor for more thorough testing. We found that the pegylation of PAL helped preserve activity upon

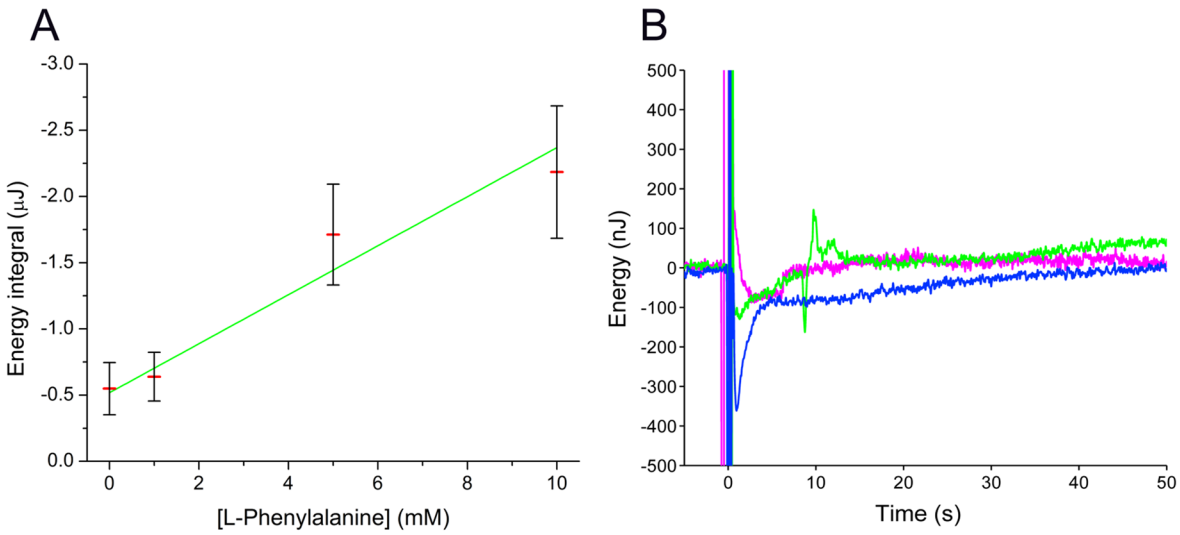

Figure 22. Phenylalanine assay (A) Phe concentration response when reacted with immobilized PEG-PAL on the capillary calorimeter. [Phe] confidence is lower with an $R^2 = 0.9295$ and uncertainty of ± 3 mM. This is due to the lower activity of PEG-PAL compared to CAT, smaller reaction enthalpy, and greater error associated with rehydration of the dried PEG-PAL. Means ± s.d. are shown (n=4 per point) (B) Representative signals from 10 mM (blue), 1 mM (green), and 0 mM (magenta) Phe reacting on the capillary calorimeter. The low activity of PEG-PAL leads to a longer integration time and greater error associated with baseline drift.

drying and helped to localize the enzyme to the thermopile upon rehydration with the sample fluid. As with the H_2O_2 assay, a main source of error was due to uneven dissolution if the enzyme spots, but was compounded by the lower reaction enthalpy and activity of PAL. As **Figure 22B** shows, the signals for 0 and 1 mM Phe are occluded by noise and small baseline changes lead to large integral errors. We our diffusion model, we estimated 0.0078 units of CAT were present after sample addition, but only 0.0006 units of PEG-PAL remained. If another Phe reacting enzyme (i.e. phenylalanine 2-monooxygenase, EC 1.13.12.9) were used, which has potentially 50 times higher activity[25], sub milimolar Phe detection would be possible. However, phenylalanine 2-monooxygenase does not have the commercial availability of PAL.

In comparison to our standing drop nano-calorimeters used for TELISA[19], error due to evaporation and heat of dilution upon sample injection is greatly reduced. Previously, after the

reaction droplet was placed in the calorimeter, at least 5 minutes was required for evaporation to stabilize and after each sample injection the signal baseline would shift, necessitation curve fitting to remove the offset. Utilizing a differential sensing approach eliminates theses error and in combination with the capillary liquid handling eliminates the need for precision sample application. Even though sensitivity is reduced by a factor of 4, these devices still have the ability to measure milimolar concentrations of blood analytes. Future studies will examine the effects plasma and whole blood have on device performance. Since the space required for each thermopile is small (~1 mm^2) and chip based, it would be possible to include several sensors in one capillary channel. These could provide control reactions and monitor several analytes at once.

Acknowledgements

This work was supported by a grant from BioVentures, Inc. We would like to thank Evan Kazura for his assistance with diffusion modeling. Furthermore, we thank John Phillips for discussions regarding Phenylketonuria and its management.

References

1. Elder, M., *Point of Care Diagnostics*, BCC Research, (2014).
2. Newman, J. D. & Turner, A. P. F. Home Blood Glucose Biosensors: A Commercial Perspective. *Biosensors Bioelectron.* **20**, 2435-2453 (2005).
3. Vockley, J. et al. Phenylalanine Hydroxylase Deficiency: Diagnosis and Management Guideline. *Genetics in medicine : official journal of the American College of Medical Genetics* **16**, 188-200 (2014).
4. Banta-Wright, S. A. & Steiner, R. D. Tandem Mass Spectrometry in Newborn Screening: A Primer for Neonatal and Perinatal Nurses. *J. Perinat. Neonatal Nurs.* **18**, 41-58; quiz 59-60 (2004).
5. Longo, N. et al. Single-Dose, Subcutaneous Recombinant Phenylalanine Ammonia Lyase Conjugated with Polyethylene Glycol in Adult Patients with Phenylketonuria: An Open-Label, Multicentre, Phase 1 Dose-Escalation Trial. *Lancet* **384**, 37-44 (2014).
6. De Corcuera, J. I. R. & Cavalieri, R. P., in *Encyclopedia of Agricultural, Food, and Biological Engineering* (Taylor & Francis, 2007), pp. 119-123.
7. Danielsson, B. The Enzyme Thermistor. *Appl. Biochem. Biotechnol.* **7**, 127-134 (1982).
8. Danielsson, B. Calorimetric Biosensors. *J. Biotechnol.* **15**, 187-200 (1990).
9. Lammers, F. & Scheper, T. Thermal Biosensors in Biotechnology. *Adv. Biochem. Eng. Biotechnol.* **64**, 35-67 (1999).
10. Lammers, F. & Scheper, T. On-Line Monitoring of Enzyme-Catalyzed Biotransformations with Biosensors. *Enzyme Microb. Technol.* **20**, 432-436 (1997).
11. Xie, B., Ramanathan, K. & Danielsson, B. Principles of Enzyme Thermistor Systems: Applications to Biomedical and Other Measurements. *Adv. Biochem. Eng. Biotechnol.* **64**, 1-33 (1999).
12. Zhang, Y. Y. & Tadigadapa, S. Calorimetric Biosensors with Integrated Microfluidic Channels. *Biosens. Bioelectron.* **19**, 1733-1743 (2004).
13. Lee, W. et al. High-Sensitivity Microfluidic Calorimeters for Biological and Chemical Applications. *Proc. Natl. Acad. Sci. U. S. A.* **106**, 15225-15230 (2009).
14. Davaji, B. & Lee, C. H. A Paper-Based Calorimetric Microfluidics Platform for Bio-Chemical Sensing. *Biosensors Bioelectron.* **59**, 120-126 (2014).
15. Son Vu Hoang, L. & Tadigadapa, S., presented at the Sensors, 2012 IEEE, 2012 (unpublished).
16. Wang, J. Electrochemical Glucose Biosensors. *Chem. Rev.* **108**, 814-825 (2008).
17. Minteer, S. D., *Enzyme Stabilization and Immobilization : Methods and Protocols*. (Humana Press, New York, 2011).
18. Zalipsky, S. Chemistry of Polyethylene Glycol Conjugates with Biologically Active Molecules. *Adv. Drug Del. Rev.* **16**, 157-182 (1995).
19. Lubbers, B. et al. Nanoliter Droplet Based Calorimetry for Point of Care Elisa. *Submitted to Proc. Natl. Acad. Sci.* (2015).
20. Tewari, Y. B., Gajewski, E. & Goldberg, R. N. An Equilibrium Study of the Conversion of L-Phenylalanine to Trans-Cinnamic Acid and Ammonia. *The Journal of Physical Chemistry* **91**, 904-909 (1987).
21. Kustov, A. V. & Korolev, V. P. The Thermodynamic Parameters of Solution of L-Phenylalanine in Water. *Russ J Phys Chem a+* **81**, 193-195 (2007).

22. Gareth Rees, D. & Hugh Jones, D. Stability of L-Phenylalanine Ammonia-Lyase in Aqueous Solution and as the Solid State in Air and Organic Solvents. *Enzyme Microb. Technol.* **19**, 282-288 (1996).
23. Halliwell, B., Clement, M. V. & Long, L. H. Hydrogen Peroxide in the Human Body. *FEBS Lett.* **486**, 10-13 (2000).
24. Tyn, M. T. & Gusek, T. W. Prediction of Diffusion Coefficients of Proteins. *Biotechnol. Bioeng.* **35**, 327-338 (1990).
25. Koyama, H. Purification and Characterization of a Novel L-Phenylalanine Oxidase (Deaminating and Decarboxylating) from Pseudomonas Sp. P-501. *J Biochem* **92**, 1235-1240 (1982).

CHAPTER V

Conclusions And Future Research

Summary of Findings

The primary focus of this dissertation has been the development and optimization of new calorimetric devices for high-sensitivity diagnostic testing. We have shown that the field of calorimetry can be extended to new sensitivity levels through the use of micro-fabricated thermopiles on polymer membranes. Heat flow and diffusion modeling enabled optimization of calorimeter design *in silico* and improved our understanding of enzyme kinetics. Combining calorimetry with ELISA resulted in orders of magnitude reduction in sample requirements. The ultimate outcome of this dissertation was the creation of a novel sub-microliter POC device for testing blood analytes.

Towards Aim 1, we successfully designed and built calorimeters capably of sub-nanowatt sensitivity. Our initial studies in Chapter II using prefabricated IR sensors as small volume calorimeters provided much insight into reaction chemistry and heat flow at the nanoliter scale. We determined the best techniques for calibrating a standing drop nano-calorimeter, from laser heating of the drop to find the time constant, to acid base reactions to determine sensitivity. Much work was done understanding evaporation at these volumes and how to prevent errors from it. We found that the simple act of injecting tens of picoliters into a 5 nl drop resulted in changes to the evaporation rate, and consequently a signal baseline shift. After accounting for these shifts, we were able to successfully calibrate the IR sensors and found that as drop volume decreases, a dramatic increase in sensitivity is gained. Through heat flow modeling we found that

changing from the high conductivity silicon nitride/silicon oxide membrane of the IR sensor to a low conductivity polymer membrane, sensitivity was more than doubled. In Appendix D, we investigated different thermopile materials and performed our own thin film measurements of resistivity and Seebeck coefficients. This allowed us to determine that titanium and bismuth were the best thermopile materials for us as they had the best combination of low thermal conductivity, low electrical resistance, and high Seebeck coefficient. Further refinement of our heat flow model provided us with the best dimension and thermopile thickness for our calorimeters. With this in mind, photolithography masks were commissioned and production began. Along the way we worked out many of the technical issues involved in fabricating Bi/Ti thermopiles on freestanding Su-8 membranes and detailed the fabrication in Chapter III. Once successful devices were built, we set about characterizing them. We found that they matched our model predictions well, providing us with calorimeters sensitive to 375 $pJ/Hz^{1/2}$, almost an order of magnitude better than the leading calorimeters.

Towards aim 2, we applied our new calorimeters to nanoliter TELISA in Chapter III. We utilized a sandwich ELISA approach with calorimetric readout to successfully measure µg/ml concentrations of the anti-cancer mAb trastuzumab in human serum. By reducing the sample size, the time required for binding steps was greatly reduced while at the same time reducing sample requirements many fold over conventional microplate based ELISA. We found that serum matrix effects were mitigated by our device design. We believe the combination of our device materials and limited dimensions allowed for use of a trastuzumab AB_1 that previously was overwhelmed by non-specific binding in the presence of serum. Different buffers, detergents, and reagent concentrations were investigated to find the conditions needed for maximal trastuzumab sensitivity. We found the best way to correlate calorimeter signal with

analyte concentration was through determination of the signal time constant. This posed some problems due to the baseline shift mentioned previously, but with our prior knowledge, we were able to compensate for this error. In our experiences with nanoliter TELISA, we found the largest impediment to ease-of-use and therefore commercialization was the lack of an integrated liquid handing system. We were still using glass micropipettes and micromanipulators to perform the experiments. This cumbersome and inefficient system meant these devices would be limited to only the research lab without significant improvements.

Towards Aim 3, we used our modeling knowledge to construct a capillary channel based calorimeter with POC testing potential. With the need for built in sample handling clear, we set about finding a way to do this without sacrificing all the performance gains we had built into our calorimeters. By placing two Su-8 membranes in close proximity, we found that capillary forces alone would deliver sample fluid to our sensor. Modeling showed that if the channels were kept thin, the heat flow losses would be minimal. Towards reducing the measurement errors that had plagued us previously, we created a differential sensing thermopile that eliminated most evaporation, dilution, and baseline drift errors. In Chapter IV, we used CAT as a model enzyme due to its high energy output and demonstrated H_2O_2 detection down to 100 μM with our new capillary calorimeter. Diffusion modeling confirmed our belief that H_2O_2 local to the enzyme was consumed quickly, followed by a steady state limited by the diffusion of substrate to the enzyme site. It was found that complicated enzyme immobilization strategies were not needed, and simple drying of the enzyme on the sensor provided a high concentration of enzyme that remained near the thermopile. Our capillary sample deliver technique worked well and eliminated the need for micropipette injections. With these calorimeters, we created a novel Phe POC testing device with potential to enable at home monitoring of phenylketonuria. Though the

assay is only reliable down to 5 mM in its current form, it shows for the first time that a calorimetric biosensor can be adapted to a POC format.

Future Research

Our next goal is to extend the sensitivity of our Phe assay. We know PEG-PAL is not the ideal enzyme due to low activity and enthalpy. However, more promising enzymes like phenylalanine 2-monooxygenase are not commercially available, requiring us to find new sources or someone with the capability to purify the enzymes for us. We will also investigate enzyme preservation techniques to provide adequate shelf life for a future POC device. The conditions under which the enzymes are desiccated, the included preservatives, and the storage conditions are all critical to preserving maximal activity. We will also investigate the co-immobilization of other enzymes with CAT to create assays for other blood analytes. We have not done testing with plasma and whole blood on our devices yet. We must determine the effects of such components and find ways to mitigate their contribution. We will also investigate the feasibility of combining our capillary system with our TELISA devices. Different enzyme immobilization strategies and the ability to perform wash steps on chip would need to be considered. All this in the hopes of creating new diagnostic tools to improve patient outcomes through better, faster, and cheaper testing.

APPENDIX A

MATLAB Code

Time constant calculation

```
clear all
close all
clc

Data1=dlmread('laser_drop_build_1nl_blue_25k_2.txt','\t');
Data=Data1(:,2:3);
N=length(Data);
f=100; % frequency
G=25000; %gain
Start_point=350*f;
End_point=N;

Data_2= Data(Start_point:End_point,1)/G*1e6; %conver to uV
Data_1=Data(Start_point:End_point,2);
N_2=length(Data_2);
S1=1;
S2=N_2;
figure (1)
grid on
hold on
plot(Data_2)
title('raw data')
ylabel('uV')
grid on


Max_point=zeros(2000,2); % this array will be used to store the peak values
of the data
j=1;
for i=2:(N_2-1)
    if Data_1(i)>.5 % peak heights to include
        Max_point(j,1)=i;Max_point(j,2)=Data_1(i);
        j=j+1;
    end
end
j=j-1;
figure(2)
plot(Max_point(1:j,1),Max_point(1:j,2));
title('Peaks')
% Peak=zeros(p,1); % this array to store the peak values
Mark_1=1;Mark_2=0;
%these two variables will be used to store the local limit for one injection
k=1;
q=0;
for i=1:j
```

```
    if Max_point(i+1,1)-Max_point(i,1)>500 %only selects peaks spaced at
least 20s apart
        Mark_2=i;
        [Y,I] = max(Max_point(Mark_1:Mark_2,2));
        Peak(k)=Max_point(I+q,1);
        Mark_1=i+1;
        k=k+1;
        q=i;
    end
end
[Y,I] = max(Max_point(Mark_1:i,2)); %catches last peak missed by loop
Peak(k)=Max_point(I+q,1);

p=length(Peak);
baseline_t=zeros(p,1);
baseline_b=zeros(p,1);
cutoff=zeros(p,1);
T=zeros(p,1);
for i=1:p
    baseline_t(i)=mean(Data_2(Peak(i)-400:Peak(i)-10));
    baseline_b(i)=mean(Data_2(Peak(i)+3000:Peak(i)+3500));
    cutoff(i)=(baseline_t(i)-baseline_b(i))*(1/exp(1))+baseline_b(i);
    for s=1:400
        if Data_2(Peak(i)+s)>cutoff(i)
        T(i)=T(i)+1;
        end
    end
end
t=T.*10;
figure(3)
x=0:50;
plot(x,t)
```

Pico-calorimeter detrending and signal integration

```
%This line reads the data
clear all
close all
clc

Data1=dlmread('2pt5nl_lowenergy_1mM_2hz_filter_2.txt','\t');
Data=Data1(:,2);
N=length(Data);
figure(1);grid on;
f=100;      % frequency
G=25000;     %gain
p=6;        % # peaks to consider
E=1e-8;   %energy per injection
Start_point=460*f;
End_point=706*f;
R=-5;         % retrend


Data_1= Data(Start_point:End_point)/G*1e6; %conver to uV
```

```
% Data_1K= Data(Start_point:End_point)/G/480e-6; %convert to K
Data_2=detrend(Data_1);
% Data_2K=detrend(Data_1K);
N_2=length(Data_2);
S1=1;
S2=N_2;
figure (1)
plot(Data_2(S1:S2));
title('Detrended data')
ylabel('uV')
grid on

y=1:length(Data_2);
trend=y'*-1e-6*R;
Data_2=Data_2+(trend*-12); %Add slight trend back to data to make baseline
detection work better

figure(2)
plot(Data_2)
title('Retrended Data')
ylabel('uV')
grid on

Max_point=zeros(2000,2); % this array will be used to store the peak values
of the data
j=1;
for i=2:(N_2-1)
    if Data_2(i)>-.1 % peak heights to include
        Max_point(j,1)=i;Max_point(j,2)=Data_2(i);
        j=j+1;
    end
end
j=j-1;
figure(3)
plot(Max_point(1:j,1),Max_point(1:j,2));
title('Peaks')
Peak=zeros(p,1); % this array to store the peak values
Mark_1=1;Mark_2=0;
%these two variables will be used to store the local limit for one injection
k=1;
q=0;
for i=1:j
    if Max_point(i+1,1)-Max_point(i,1)>2000 %only selects peaks spaced at
least 20s apart
        Mark_2=i;
        [Y,I] = max(Max_point(Mark_1:Mark_2,2));
        Peak(k)=Max_point(I+q,1);
        Mark_1=i+1;
        k=k+1;
        q=i;
    end
end
[Y,I] = max(Max_point(Mark_1:i,2)); %catches last peak missed by loop
Peak(k)=Max_point(I+q,1);
```

```
Voltage_time=zeros(p,1); %this array to record the voltage*time for each
injection
base=zeros(2000,1);
baseline=zeros(p,1);
baselinea=zeros(p,1);
offset=zeros(p,1);
for i=1:p
     baselinea(i)=mean(Data_2(Peak(i)+1500:Peak(i)+2000));
     baseline(i)=mean(Data_2(Peak(i)-500:Peak(i)-25));
     offset(i)=baseline(i)-baselinea(i); %find signal drop
     Data_2(Peak(i)-25:N_2)=Data_2(Peak(i)-25:N_2)+offset(i); %remove drop
end

for i=1:p
    baselinea(i)=mean(Data_2(Peak(i)-400:Peak(i)-50));
    for k=1:1000
        q=(Data_2(Peak(i)-50+k)-baselinea(i))*(1/f);
        Voltage_time(i)=Voltage_time(i)+q;
    end
end

figure(4)
plot(Data_2)
grid on

figure(5)
plot(Voltage_time)
title('Voltage time')

Voltage_time;
scaledVT = Voltage_time.*G./1e6;

VperW=scaledVT./G./E
VperWavg=mean(VperW)
deviation_pct=std(Voltage_time)/VperWavg*100
Data_i=Data_2;
%%
close all
Data1=dlmread('2pt5nl_lowenergy_control_2hz_filter.txt','\t');
Data=Data1(:,2);
N=length(Data);

figure(1);grid on;
f=100;       % frequency
G=25000;      %gain
p=6;         % # peaks to consider
E=1e-8;    %energy per injection
Start_point=250*f;
End_point=550*f;
R=0;          % retrend


Data_1= Data(Start_point:End_point)/G*1e6; %conver to uV
Data_1K= Data(Start_point:End_point)/G/480e-6; %convert to K
Data_2=detrend(Data_1);
```

```
Data_2K=detrend(Data_1K);


N_2=length(Data_2);
S1=1;
S2=N_2;
figure (1)
plot(Data_2(S1:S2));
title('Detrended data')
ylabel('uV')
grid on

y=1:length(Data_2);
trend=y'*-1e-6*R;
Data_2=Data_2+(trend*-12); %Add slight trend back to data to make baseline
detection work better

figure(2)
plot(Data_2)
title('Retrended Data')
ylabel('uV')
grid on

Max_point=zeros(2000,2); % this array will be used to store the peak values
of the data
j=1;
for i=2:(N_2-1)
    if Data_2(i)>-.032 % peak heights to include
        Max_point(j,1)=i;Max_point(j,2)=Data_2(i);
        j=j+1;
    end
end
j=j-1;
figure(3)
plot(Max_point(1:j,1),Max_point(1:j,2));
title('Peaks')
Peak=zeros(p,1); % this array to store the peak values
Mark_1=1;Mark_2=0;
%these two variables will be used to store the local limit for one injection
k=1;
q=0;
for i=1:j
    if Max_point(i+1,1)-Max_point(i,1)>2000 %only selects peaks spaced at
least 20s apart
        Mark_2=i;
        [Y,I] = max(Max_point(Mark_1:Mark_2,2));
        Peak(k)=Max_point(I+q,1);
        Mark_1=i+1;
        k=k+1;
        q=i;
    end
end
[Y,I] = max(Max_point(Mark_1:i,2)); %catches last peak missed by loop
Peak(k)=Max_point(I+q,1);
```

```
Voltage_time_c=zeros(p,1); %this array to record the voltage*time for each
injection
base=zeros(2000,1);
baseline=zeros(p,1);
baselinea=zeros(p,1);
offset=zeros(p,1);
for i=1:p
     baselinea(i)=mean(Data_2(Peak(i)+1500:Peak(i)+2000));
     baseline(i)=mean(Data_2(Peak(i)-500:Peak(i)-25));
     offset(i)=baseline(i)-baselinea(i); %find signal drop
     Data_2(Peak(i)-25:N_2)=Data_2(Peak(i)-25:N_2)+offset(i); %remove drop
end

for i=1:p
    baselinea(i)=mean(Data_2(Peak(i)-400:Peak(i)-50));
    for k=1:1000
        q=(Data_2(Peak(i)-50+k)-baselinea(i))*(1/f);
        Voltage_time_c(i)=Voltage_time_c(i)+q;
    end
end

figure(4)
plot(Data_2)
grid on

figure(5)
plot(Voltage_time_c)
title('Voltage time')

Voltage_time_c;
scaledVT_c = Voltage_time_c.*G./1e6;

VperW_c=scaledVT_c./G./E
VperWavg_c=mean(VperW_c)
deviation_pct_c=std(Voltage_time_c)/VperWavg_c*100

Etot=[.7e-9 1.4e-9 2.8e-9 5.56e-9 11.18e-9 22.37e-9]'*6;

VTtot=Voltage_time-Voltage_time_c
scaledVT_tot = VTtot.*G./1e6;
VperW_tot=scaledVT_tot./G./Etot
figure(6)
plot(VperW_tot)

figure(7)
plot(Data_2(2400:30000))
hold on
plot(Data_i,'-g')
```

Enzyme kinetics fitting

```
clear all
tstep=0.01;       % time step (seconds)
kcat=2000*tstep; % turnover (1/s)
Km=0.003;         % concentration at half Vmax (M)
Epg=3;           % enzyme mass in 1 nl (pg)
EMW=42000;       % enzyme molecular weight
E0=Epg/1000/EMW; % enzyme concentration (M)
S0=.005;          % substrate concentration (M)
length=200;      % length time to model (s)
t=0:tstep:length-tstep;
Psens=45;

load('Hd.mat')

v(1)=(kcat*E0*S0)/(Km+S0);
S(1)=S0;
for i=2:(length/tstep)
    S(i)=S(i-1)-v(i-1);
    v(i)=(kcat*E0*S(i))/(Km+S(i)); % units of moles/time step/l
end
V=v(1)/tstep   % V initial
figure(3)
plot(t,S)
title('Substrate Concentration')
% axis([0 50 0 .05])
% hold on
grid on
% figure(2)
% D=diff(-S);
%
% plot(S(2:end),D);
% title('dP/dt')
% grid on
% figure(3)
% plot(t,v*10)
% title('Rate (mols/s)')
% hold on
grid on
figure(4)
E=v*1e-9*98000*2; % convert v to 1nl volume and multiply by energy
Ei=zeros(1,1000);
E=[Ei E];
ti=0.01:0.01:length+10;
Ef=filter(Hd,E);
uV=Ef*Psens*1e6;    % convert enery to uV
plot(ti,uV/tstep)
title('uVolts')
Energy=trapz(E)
uV_S=trapz(uV)
grid on

M=max(Ef);
Me=M*(1/exp(1));
```

```
for i=1:((length+10)/tstep)
        if Ef(i)>Me
        tau=i*tstep;
        end
end

tau=tau-10
```

TELISA curve fitting and signal integration

```
function plot_fit4(file)
while 1==1
% close all
% clear all
% clc

% file is file reference, ends in .txt
% segs is # of segments to fit
% polyn is polynomial order for fitting

% Construct a questdlg with three options
choice = questdlg('Use previous fit?', ...
    'Fitting', ...
    'Yes, do integration','Yes, find tau','No, just plot','No, just plot');
% Handle response
switch choice
    case 'Yes, do integration'
        f=100;  %sampling frequency
        D=load('data.mat');
        X=D(1).X;
        Data_fit=D(1).Data_fit;

        figure(1)
        set(gcf,'Position',[1,41,1590,1080])
        plot(X(1:length(Data_fit)),Data_fit)
        grid on
        title(file)
        pause;
        [x,y]=ginput(2);
        start=double(int32(x(1)*f));
        ending=double(int32(x(2)*f));

        n=(ending-start);
        Voltage_time=0;
        baseline=mean(Data_fit((ending-100):ending));
        for k=1:n   %length to integrate peak
            q=(Data_fit((start)+k)-baseline)*(1/f);
            Voltage_time=Voltage_time+q;
        end
        disp('Voltage time (uV/s)')
        disp(Voltage_time)
```

```
    case 'Yes, find tau'
        f=10;  %sampling frequency
        D=load('data.mat');
        X=D(1).X;
        Data_fit=D(1).Data_fit;
        pre=2000;   % length to read before starting
        post=2000;   % length to continure after ending
        figure(1)
        set(gcf,'Position',[1,41,1590,1080])
        plot(X(1:length(Data_fit)),Data_fit)
        title(file)
        grid on
        hold on
%         title(file)
        pause;
        [x,y]=ginput(3);
        starting=double(int32(x(1)*f));
        peaking=double(int32(x(2)*f));
        peak=y(2);
        ending=double(int32(x(3)*f));
        final=y(3);

%         data=Data_fit(starting:ending)-final;
        e=(peak-final)*(1/exp(1));
%         halfa=(peak-final)*0.5; %half level
        Data2=Data_fit(peaking:ending);
        Xi=(1/f:1/f:length(Data2)/f)';
        F=smooth(Data2,1000,'lowess');  %specify smoothinhg window
        plot(Xi+peaking/f,F,'r')

        for i=1:length(F)   % find tau based on decay
            if F(i)-final>e
                tau=i/f;
            end
        end
        tau=tau+((peaking-starting)/f)  %correct for peak shift

        base=y(1);
        shift=base-final;
        ts=0:0.01:(ending-peaking+post-pre)/f;
        ta=0:0.01:(ending-peaking+post)/f;
        y1=Data_fit(peaking-pre:peaking-1)-shift;
        ecurve=shift*exp(-ts/(tau*0.8));   % fit exp cure base on tau
        hold on
        plot(ts+(peaking/100),ecurve+final,'-r')   % plot exp curve against
data
        hold off
        y2=Data_fit(peaking:ending+post-pre)-ecurve';  % remove exp curve
        ya=[y1' y2'];
        figure(3)
        plot(ta,ya-final);
        title(file)
        grid on
        hold on

        F_post=(F-final)-ecurve';   %remove exp curve for post tau calc
```

```
        Xf=1/f:1/f:length(F)/f;
        plot(Xf+pre/f,F_post,'-r')
        title(file)
        hold off
        e_post=max(F_post)*(1/exp(1));
        for i=1:length(F_post)    % find tau based on decay
            if F_post(i)>e_post
                tau_p=i/f;
            end
        end

        tau_p=tau_p+((peaking-starting)/f)  %correct for peak shift

        Data_fit=ya-final;
        X=ta;
        savefile='dataf.mat';    %save fitted file for integration later
        save(savefile,'Data_fit','X')

    case 'No, just plot'
        Data1=dlmread(file,'\t');
        Data=Data1(:,2);
        Data=Data/10000*1e6;    %amp gain correction
        f=100;  %sampling frequency
        N=length(Data);
        X=1/f:1/f:N/f;
        figure(1);
        set(gcf,'Position',[1,41,1590,1080])
        plot(X,Data);
        grid on
        title(file)
        pause;
        [xr,yr]=ginput(2);  %specify two point on line to be flat
        m=diff(yr)/diff(xr);
        Data_fit=Data+(-m*X');  %detrend data
        plot(X,Data_fit);
        title(file)
        grid on

        savefile='data.mat';    %save fitted file for integration later
        save(savefile,'Data_fit','X')
end
K=menu('Thanks for using plot fit. Would you like another run?','yes','no');
if K==1
else
    disp('Done')
break
end
end
```

APPENDIX B

MATLAB Integration of COMSOL Code for Device Optimization

```
function Gtot=com1nlpoly_Bi_Ti(Q,d,aa,tp)
% COMSOL Multiphysics Model M-file
% Generated by COMSOL 3.5 (COMSOL 3.5.0.494, $Date: 2008/09/19 16:09:48 $)
% Some geometry objects are stored in a separate file.
% The name of this file is given by the variable 'flbinaryfile'.

flclear fem

% COMSOL version
clear vrsn
vrsn.name = 'COMSOL 3.5';
vrsn.ext = '';
vrsn.major = 0;
vrsn.build = 494;
vrsn.rcs = '$Name:  $';
vrsn.date = '$Date: 2008/09/19 16:09:48 $';
fem.version = vrsn;

flbinaryfile='1nl_basem_shift.mphm';

% Geometry
clear draw
g7=flbinary('g7','draw',flbinaryfile);
g8=flbinary('g8','draw',flbinaryfile);
g2=flbinary('g2','draw',flbinaryfile);
g1=flbinary('g1','draw',flbinaryfile);
g6=flbinary('g6','draw',flbinaryfile);
g5=flbinary('g5','draw',flbinaryfile);
g4=flbinary('g4','draw',flbinaryfile);
g3=flbinary('g3','draw',flbinaryfile);

draw.s.objs = {g7,g8,g2,g1,g6,g5,g4,g3};
draw.s.name = {'R7','CO1','R6','R2','R3','R1','R4','R5';
draw.s.tags = {'g7','g8','g2','g1','g6','g5','g4','g3';
fem.draw = draw;
fem.geom = geomcsg(fem);

% Geometry
g9=rect2(2e-3-(d/2),7.5E-4,'base','corner','pos',[-0.0020,-7.5E-4]);
%lower
g10=rect2(2e-3-(d/2),7.5E-4,'base','corner','pos',[-0.0020,0]); % upper
g11=rect2(d/2,2.0E-6,'base','corner','pos',[-d/2,0]);       %mem
g12=rect2((d/2)-(aa/2),tp,'base','corner','pos',[-d/2,-tp]);    %tp
parr={point2(-(aa/2)-0.25e-6,0)};   %meas point
g13=geomcoerce('point',parr);

% Analyzed geometry
clear p s
```

```
p.objs={g13};
p.name={'PT1'};
p.tags={'g13'};

s.objs={g4,g5,g7,g8,g9,g10,g11,g12};
s.name={'R4','R1','R7','CO1','R2','R3','R5','R6'};
s.tags={'g4','g5','g7','g8','g9','g10','g11','g12'};

fem.draw=struct('p',p,'s',s);
fem.geom=geomcsg(fem);

% Initialize mesh
fem.mesh=meshinit(fem, ...
                  'hauto',7);

% (Default values are not included)

% Application mode 1
clear appl
appl.mode.class = 'GeneralHeat';
appl.mode.type = 'axi';
appl.module = 'HT';
appl.shape = {'shlag(1,''J'')','shlag(2,''T'')'};
appl.border = 'on';
appl.assignsuffix = '_htgh';
clear prop
prop.analysis='static';
appl.prop = prop;
clear bnd
bnd.type = {'T','cont','ax','q0'};
bnd.shape = 1;
bnd.T0 = {0,0,0,0};
bnd.ind = [1,1,1,2,2,2,2,2,2,2,2,2,2,2,2,2,2,2,2,2,2,2,2,2,2,3,3,3,4,3, ...
  3,3,3,2];
appl.bnd = bnd;
clear equ
equ.eta = {'mat1_eta(T[1/K])[Pa*s]',1,1,1,1,1};
equ.sdtype = 'gls';
equ.opacity = {0,1,1,1,0,1};
equ.rho = {1.02,2500,1200,3500,997,8700};
equ.init = {0,0,0,0,0,{273.15;0}};
equ.shape = 2;
equ.C = {1005,740,1200,225,4182,385};
equ.gamma = {1.4,1,1,1,1,1};
equ.Q = {0,0,0,0,Q,0};
equ.name = {'air','ceramic','poly','TP','water','new group'};
equ.k = {0.024,1,0.2,6.3,0.58,400};
equ.ind = [1,2,2,3,3,1,4,3,1,5];
appl.equ = equ;
fem.appl{1} = appl;
fem.sdim = {'r','z'};
fem.frame = {'ref'};
fem.border = 1;
fem.outform = 'general';
clear units;
units.basesystem = 'SI';
```

```
fem.units = units;

% Library materials
clear lib
lib.mat{1}.name='Air';
lib.mat{1}.varname='mat1';
lib.mat{1}.variables.nu0='nu0(T[1/K])[m^2/s]';
lib.mat{1}.variables.eta='eta(T[1/K])[Pa*s]';
lib.mat{1}.variables.gamma='1.4';
lib.mat{1}.variables.sigma='0[S/m]';
lib.mat{1}.variables.C='Cp(T[1/K])[J/(kg*K)]';
lib.mat{1}.variables.rho='rho(p[1/Pa],T[1/K])[kg/m^3]';
lib.mat{1}.variables.k='k(T[1/K])[W/(m*K)]';
lib.mat{1}.variables.cs='cs(T[1/K])[m/s]';
clear fcns
fcns{1}.type='inline';
fcns{1}.name='cs(T)';
fcns{1}.expr='sqrt(1.4*287*T)';
fcns{1}.dexpr={'diff(sqrt(1.4*287*T),T)'};
fcns{2}.type='inline';
fcns{2}.name='rho(p,T)';
fcns{2}.expr='p*0.02897/8.314/T';
fcns{2}.dexpr={'diff(p*0.02897/8.314/T,p)','diff(p*0.02897/8.314/T,T)'};
fcns{3}.type='piecewise';
fcns{3}.name='Cp(T)';
fcns{3}.extmethod='const';
fcns{3}.subtype='poly';
fcns{3}.expr={{'0','1.04763657E+03','1','-3.72589265E-01','2', ...
  '9.45304214E-04','3','-6.02409443E-07','4','1.28589610E-10'}};
fcns{3}.intervals={'200','1600'};
fcns{4}.type='piecewise';
fcns{4}.name='eta(T)';
fcns{4}.extmethod='const';
fcns{4}.subtype='poly';
fcns{4}.expr={{'0','-8.38278000E-07','1','8.35717342E-08','2', ...
  '-7.69429583E-11','3','4.64372660E-14','4','-1.06585607E-17'}};
fcns{4}.intervals={'200','1600'};
fcns{5}.type='piecewise';
fcns{5}.name='nu0(T)';
fcns{5}.extmethod='const';
fcns{5}.subtype='poly';
fcns{5}.expr={{'0','-5.86912450E-06','1','5.01274491E-08','2', ...
  '7.50108343E-11','3','1.80336823E-15','4','-2.91688030E-18'}};
fcns{5}.intervals={'200','1600'};
fcns{6}.type='piecewise';
fcns{6}.name='k(T)';
fcns{6}.extmethod='const';
fcns{6}.subtype='poly';
fcns{6}.expr={{'0','-2.27583562E-03','1','1.15480022E-04','2', ...
  '-7.90252856E-08','3','4.11702505E-11','4','-7.43864331E-15'}};
fcns{6}.intervals={'200','1600'};
lib.mat{1}.functions = fcns;


fem.lib = lib;
```

```
% ODE Settings
clear ode
clear units;
units.basesystem = 'SI';
ode.units = units;
fem.ode=ode;

% Multiphysics
fem=multiphysics(fem);

% Extend mesh
fem.xmesh=meshextend(fem);

% Solve problem
fem.sol=femstatic(fem, ...
                  'solcomp',{'T'}, ...
                  'outcomp',{'T'}, ...
                  'blocksize','auto');

% Save current fem structure for restart purposes
fem0=fem;

% % Plot solution
% postplot(fem, ...
%          'tridata',{'T','cont','internal','unit','K'}, ...
%          'trimap','jet(1024)', ...
%          'title','Surface: Temperature [K]', ...
%          'axis',[-6.193398684210526E-4,1.2046426842105256E-4,-1.718812E-
4,1.627921E-4]);

% Integrate
I=postint(fem,'T', ...
           'unit','K', ...
           'recover','off', ...
           'dl',[13], ...
           'edim',0);
Gtot=(1/I)*(Q*1e-12);
```

APPENDIC C

LabView Code

Figure 23. Calorimeter control and recording front panel. Controls micromanipulator and picospritzer, automates sample injection, calibrate pipettes, filters data, and records data.

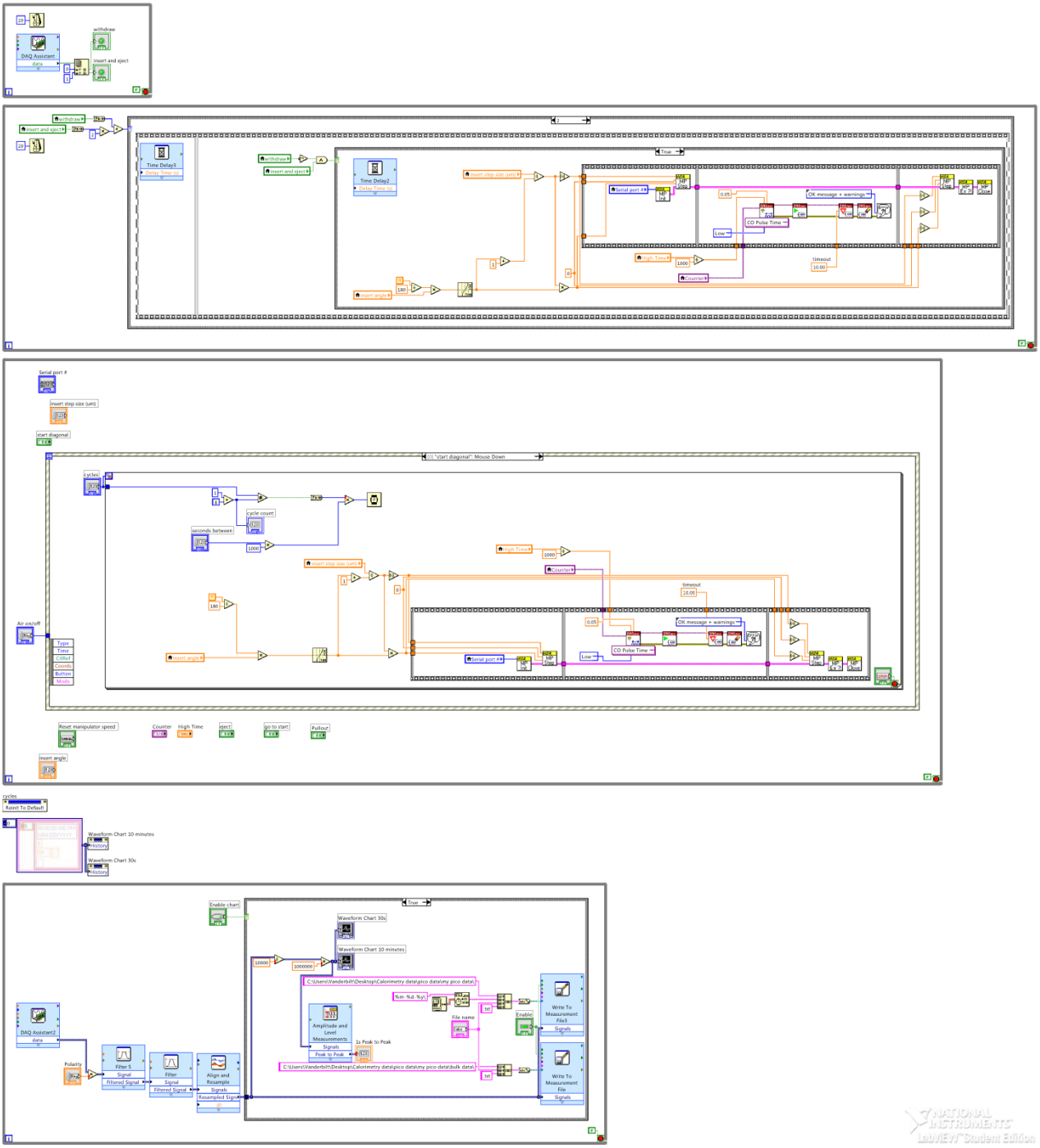

Figure 24. Calorimeter control and recording block diagram

APPENDIX D

Additional Methods

Model Fitting

As a starting point for heat flow modeling of the commercial S25 IR sensor (Dexter Research Inc.), we examined the work of Xu whom this project was inherited from. He achieved a P_{sens} of 3.05 V/W and P_{min} of 7.6 nW/√Hz at a 50 nl sample volume[1]. Finite element analysis performed by Xu showed only a modest improvement of P_{sens} to 6.15 V/W at 5 nl sample volume, so he focused on the larger and easier to work with 50 nl sample volumes. Additionally, his prediction of a P_{sens} of 9.43 V/W with an empty membrane fell far short of the manufactures stated sensitivity of 193.9 V/W. We began by replicating Xu's methods and found much higher sensitivity than he reported at 50 nl. When the sample size was reduced, a dramatic increase in P_{sens} was also noted. Our measured P_{sens} of 45.5 V/W at 5 nl greatly exceeded Xu's prediction and established the motivation for minimizing sample volume.

We believe his low figures are likely due to his underestimation of S_{tot} and oversimplifications in his FEA model. Xu stated S_{tot} as 480 μV/K or 24 μV/K per junction. This would be a typical S for a Ni/Au thermocouple, however the S25 sensor is based off of previous work by Meinel using Bi/Sb thermopiles[2]. Typical S for a Bi/Sb pair would be ~112 μV/K, but can be increased to over 400 μV/K through doping and anisotropy effects[3]. Since we did not know the exact composition of the thermopiles, we relied on fitting of our experimental data to a FEA model constructed in COMSOL. When our τ and P_{sens} data was incorporated in, a S_{tot} value of 3590 μV/K or 180 μV/K per junction was generated. This represents a 7.5 fold increase over Xu's reported S_{tot} and can account for most of the discrepancy. Additionally there were

differences between the FEA models used. Xu's model assumed that all heat generated by the chemical reaction originated from a small volume atop the larger sample drop. Our model assumed a more uniform heat distribution and found that the location of the heat origin affected output by up to 30%. Another unknown in the model was the overall thermal conductivity of the membrane. Ideally, a full 3-D model would be used to encompass all device geometries. However, the thin (1.5 μm) membrane in combination with a 2 mm wide chamber resulted in an overly complex mesh that could not be solved efficiently. Therefore, we pursued a radial 2-D model. Later, when we were more familiar with the software and when run on a more powerful computer we switch to a full 3-D model.

Using a least squares fitting of experimental reaction data at various volumes and an iterative feedback loop between COMSOL and MATLAB we solved for the unknowns G_{mem}, S_{tot}, and heat origin. A satisfactory fitting at various volumes with constants of G_{mem} and S_{tot} was produced (**Figure 8**). With this well-tuned model, our measurements of τ and P_{sens} were also verified. The S25 manufacturer's claim of 193.9 V/W sensitivity was also verified by replicating the black body radiation source they used for calibration in our model.

Device Optimization

With a new model in hand, we were now prepared to extend calorimeter performance into the picowatt range. Our S25 sensor tops out at 60 V/W sensitivity and a NEP of 500 $pW/Hz^{1/2}$ at 2.5 nl. It is limited by the high thermal conductivity of its nitride membrane and a thermopile junction pattern better suited to 5 nl droplets. Other calorimeters have used polymer membranes to reduce G_{mem}, but have relied on thick (12μm) kapton layers or parylene-C that requires its own dedicated deposition system[4,5]. One calorimeter designed for IR measurements utilized a free standing Su-8 membrane due to its low conductivity and high chemical

resistance[6]. This is an ideal membrane material for us as we have access to Su-8 and all the necessary equipment to process it. The formation of suspended silicon nitride membranes through anisotropic Si etching is well established and formed the basis for our development. Normally the backside Si etching occurs as the last step to release the membrane after all frontside processing is done. However this exposes the front side thermopiles to hot potassium hydroxide (KOH). We found that 1 μm thick low stress SiN windows were durable enough for Su-8 application and thermopile fabrication after KOH etching. The final step is to remove the SiN supporting the Su-8 membrane using reactive ion etching.

Thermopile Material Selection

In order to select to best materials for the thermopile it is helpful to look at Seebeck coefficient (S), electrical resistivity (ρ), and thermal conductivity (κ) of common thermoelectric

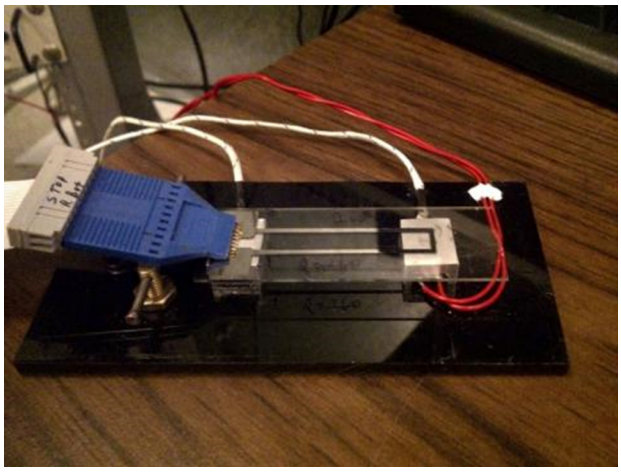

Figure 25. Combined ρ and S measuring probe. When operated for S, the block on the right was resistively heated while thermocouples measured both block temperature.

materials (**Table 4**). Other materials have been engineered with higher S, but rely on complex nanostructured thin films or silicon nanowires that are beyond our capabilities [3,7]. As **Table 4**

shows, the materials with the highest S also have the worst ρ making the following figure of merit equation useful for choosing the best materials:

$$Z = \frac{S^2}{\rho\kappa} \tag{16}$$

This equation is optimized for thermopower generation and not temperature sensing so a modified version is more useful for our application:

$$Z^* = \frac{S}{0.25\kappa + \sqrt{\rho}} \tag{17}$$

In this form, the dependency on κ is lessened, S attains a linear dependence, and the root of ρ is used as in equation 11. It is also advantageous to use the thin film parameters of the materials rather than their bulk constants as the resistance and Seebeck coefficient of most metals changes when in thin films due to grain boundaries and mean free path[3]. In order to measure the thin film

Table 4. Bulk and thin-film properties of common thermoelectric materials.

	bulk	thin film	bulk	thin film	
Material	S (μV/K)	S (μV/K)	ρ (μΩ/m)	ρ (μΩ/m)	κ (W/m·K)
Bi_2Te_3	-200	-160	7900	8400	1.9
$Bi_{(87\%)}Sb_{(13\%)}$	-80	-77	1470	1600	4.2
Bi	-72	-61	1290	1800	7.9
Constatan	-40	–	500	–	19
Ni	-18	-16	63	92	91
Au	1.5	1	21	24	320
Ti	8.7	8	420	980	22
Cr	18	17	125	1200	94
Fe	20	–	97	–	80
Nichrome	20	16	1250	1650	11
Sb	42	40	417	830	23
Sb_2Te_3	95	86	45k	55k	1.1
Si	250	–	100k+	–	149

properties we built a 4 point resistivity probe that also measures Seebeck coefficients of metal pairs (**Figure 25**).

Films of interest were e- beam deposited (Innotech deposition system) from 99.99% pure substrates (Ted Pella Inc., Kurt J. Lesker Co.) on plasma cleaned glass slides in thicknesses between 50-400 nm. Voltage drop across a known current was measured to calculate ρ in LabVIEW. To measure S, two films were deposited through shadow masks to produce a bimetal junction on one end of the slide. Then the slide was placed on the probe and the junction end warmed with a resistive heater. Generated voltage and ΔT between junctions was measured to calculate S in LabVIEW. S could be measured for relative effect between two thermoelectric metals or against a Pt reference for absolute S. Our finding for 200 nm thick Bi, Ni, Au, Cr, Ti, and NiCr (Nichrome), along with literature values for the other materials are summarized in **Table 4**. When these thin film material properties are fed into equation 17, thin film figure of merit values for different metal pairs are generated (**Table 5**). Only metals that we have the capability to deposit and pattern are considered in **Table 5**. The best pair is Bi/Sb, but there is some difficulty in patterning thin traces of Bi and Sb together. Bi/Cr and Bi/NiCr have good Z* values, but the deposition of Cr and NiCr over Su-8 forms a very rough surface with large grains

Table 5. Figure of merit for various thermocouple combinations.

	Z*	thin film Z*
Bi/Sb	3.446	2.517
Ni/Au	0.337	0.288
Ni/Ti	0.900	0.644
Ni/Cr	1.097	0.680
Bi/Ti	**2.447**	**1.682**
Bi/Cr	2.288	1.516
Bi/NiCr	2.421	1.754

and high resistance. Ti and Bi deposit smoothly, so we have focused on Bi and Ti as suitable thermopile materials.

In order to produce Bi/Ti thermopiles it was first necessary to determine the best selective chemical etchants. As Bi is more reactive and less adherent than Ti, it would be deposited after Ti patterning. This required an etchant that would remove Bi, while not affecting the underlying Ti layer. Through experimentation and adjustment of published etchants is was found that 20 H_2O:1 HF:1H_2O_2 was the best etchant for quick Ti etching without undercutting. It was difficult to wet etch Bi without undercutting and adhesion loss. Dry etching through ion milling was a better alternative as the milling rate for Bi are significantly high than Ti, allowing it to be processed after Ti patterning. Shipleys S-1813 positive photoresist allowed for processing Ti and Bi down to 5 μm linewidths. Though a linewidth of 10 μm provided better adhesion and allowed for easier alignment. Further refinement of the calorimeter design is discussed in Chapters III and IV.

References

1. Xu, J. et al. A Microfabricated Nanocalorimeter: Design, Characterization, and Chemical Calibration. *Anal. Chem.* **80**, 2728-2733 (2008).
2. Meinel, W. et al. Multijunction Thin-Film Radiation Thermopile Sensors. *Measurement* **6**, 2-4 (1988).
3. Boyer, A. & Cisse, E. Properties of Thin-Film Thermoelectric-Materials - Application to Sensors Using the Seebeck Effect. *Materials Science and Engineering B-Solid State Materials for Advanced Technology* **13**, 103-111 (1992).
4. Lee, W. et al. High-Sensitivity Microfluidic Calorimeters for Biological and Chemical Applications. *Proc. Natl. Acad. Sci. U. S. A.* **106**, 15225-15230 (2009).
5. Garden, J. L., Chateau, E. & Chaussy, J. Highly Sensitive Ac Nanocalorimeter for Microliter-Scale Liquids or Biological Samples. *Appl. Phys. Lett.* **84**, 3597-3599 (2004).
6. Mattsson, C. G. et al., *Sensors, 2007 IEEE* (Atlanta, GA, 2007), pp. 836-839.
7. Hochbaum, A. I. et al. Enhanced Thermoelectric Performance of Rough Silicon Nanowires. *Nature* **451**, 163-U165 (2008).